DRUG/DNA INTERACTIONS AND CONDENSATION INVESTIGATED WITH ATOMIC FORCE MICROSCOPY

A Dissertation
Presented to
The Academic Faculty

by

Elizabeth Deibler Gadsby

In Partial Fulfillment
Of the Requirements for the Degree
Doctor of Philosophy in the
School of Chemistry and Biochemistry

Georgia Institute of Technology
July 2004

DRUG/DNA INTERACTIONS AND CONDENSATION
INVESTIGATED WITH ATOMIC FORCE MICROSCOPY

Approved by:

Dr. Lawrence A. Bottomley, Advisor

Dr. L. Andrew Lyon

Dr. Nicholas V. Hud

Dr. William D. Hunt

Dr. Loren D. Williams

June 18, 2004

DEDICATION

This dissertation is dedicated to my Lord and Savior, Jesus Christ, who is the source of my hope and strength. I have been blessed by the prayers raised by my church family.

I could not have accomplished this endeavor without the constant support and encouragement of my loving husband, James. I love you, always!

I am grateful to my parents for their commitment to my education and growth. I appreciate my sisters' companionship and provisions to help sustain me, as well as the cards and words of motivation from my husband’s family. I honor my grandmother, Dr. Helen H. Naugle, as a role model of tenacity and humility and a daily inspiration.

ACKNOWLEDGMENTS

I am particularly grateful to Professor Lawrence Bottomley for his guidance and interest in my research. I appreciate his positive attitude and respect his vision for education. I also appreciate my committee members' time and attention to review my research. I thank Professor Brent Iverson for providing the poly-NDI compounds and his insightful discussions on my results.

This journey would not have been the same without my colleague, Mark Poggi. I appreciate his assistance in the uncountable hours of research and discussions. I also appreciate the efforts of several other students who were involved with portions of this research including Jesse Kumar, Robert Hodges, Tram Dinh, Eric Horowitz, Cathy Santai, and Christine Conwell. I enjoyed working with the TI:GER Green team members— James Hutchinson, Michael Kang, Kankindi Rwego, Benay Sager, and Brandon Walts. I wish them all a successful future.

I appreciate the support of Kimberly-Clark Corporation to allow me to take a sabbatical to pursue this goal. Several key mentors that have inspired me include Steve Englebert, Dr. Dennis Everhart, Dr. Tim McCraw, Dr. Rusty Ross, and Dr. Jerry Zabronsky.

I acknowledge the support from NSF and the Georgia Institute of Technology.

TABLE OF CONTENTS

Acknowledgments iv

List of Tables viii

List of Figures ix

List of Symbols and Abbreviations xiv

Summary xx

Chapter 1 Atomic Force Microscopy 1

1.1 History and Background 1
1.2 AFM Capabilities 3
1.2.1 AFM Instrumentation 5
1.2.2 Cantilevers 7
1.2.3 Piezoelectric Scanner 11
1.2.4 Detectors 13
1.3 AFM Operational Modes 14
1.3.1 Contact Mode 14
1.3.1.1 Friction Force Imaging 18
1.3.1.2 Force Modulation Imaging 18
1.3.2 Noncontact Mode 18
1.3.3 Intermittent Contact Mode 19
1.3.3.1 Phase Imaging 19
1.4 AFM Applications 20

Chapter 2 DNA Intercalation and Condensation 23

2.1 DNA 23
2.2 DNA and Drug Interactions 30
2.2.1 Analytical Techniques 30
2.2.2 Binding Modes 33
2.2.3 Groove Binders 37
2.2.4 Intercalators 37
2.2.5 Clinical Applications 40
2.3 Poly-Naphthalenetetracarboxylic Diimide 42
2.4 Condensation 47

Chapter 3 AFM Analysis of DNA Lengthening 50

3.1 Background 50

3.2 AFM Technique 51
3.3 Sample Preparation 54
3.3.1 DNA Plasmid 54
3.3.2 Poly-intercalator 59
3.3.3 Buffer 59
3.3.4 Surface Immobilization 62
3.4 DNA Lengthening 65
3.4.1 Theoretical Model 65
3.4.2 Contour Length Measurements 69
3.5 Bis-Naphthalenetetracarboxylic Diimide 73
3.5.1 Bis-NDI Lengthening 73
3.5.2 Bis-NDI Secondary Structures 76
3.6 Tris- and Tetra-Naphthalenetetracarboxylic Diimide 81
3.7 Discussion 85
3.8 Interaction Models 89

Chapter 4 Analysis of Toroid Formation with Poly-Naphthalenetetracarboxylic Diimide 94

4.1 Introduction 94
4.2 Formation Driving Force Theories 94
4.3 Toroid Dimensions 96
4.3.1 Toroid Shape 96
4.3.2 Toroid Diameters 96
4.3.3 Toroid Height 102
4.3.4 Toroid Compression 104
4.3.4.1 Contact Mode 104
4.3.4.2 Tapping Mode 111
4.3.5 Toroid Volume 116
4.4 Condensate Structure Distribution 118
4.5 Condensation Process Theories 121

Chapter 5 Commercial Application and Valuation 124

5.1 Program Introduction 124
5.2 Technology Definition 125
5.3 Proposed Uses 126
5.4 Intellectual Property 126
5.5 Target Market 129
5.6 Competition 132
5.7 Commercial Venture Options 133
5.8 Operations 134
5.9 Marketing 134
5.10 Roadblocks and Risks 135
5.10.1 Developmental Risk 136
5.10.2 Operational Risk 136

5.10.3 Market Risk 137
5.10.4 Competitive Risk 137
5.11 Valuation 138
5.11.1 Net Present Value / Discounted Cash Flow 139
5.11.2 Comparable Analysis 141
5.11.3 Venture Capital Analysis 143

Chapter 6 Future Research 145

6.1 DNA Lengthening and Sequence 145
6.2 DNA Binding Ligands 147
6.3 Influence of Cations 151
6.4 Intermediate Condensation Structures 152

Appendix A: pRS316 DNA Sequence 153

Appendix B: Derivation of DNA Intercalation Theoretical Lengthening Equation 156

References 159

Vita 176

LIST OF TABLES

Table 1.1 Scanning Probe Microscope instrument and cantilever manufacturers 4

Table 2.1 List of DNA-interactive drugs used clinically or in clinical research trials 41

Table 3.1 Extinction coefficients of poly-NDI at 386 nm where ε^1 was measured in 10 mM TRIS buffer with 1mM EDTA and 50 mM NaCl and ε^2 was measured in 2% SDS 61

Table 3.2 Concentration-dependent lengthening of pRS316 plasmid with bis-NDI 74

Table 3.3 Length measurements of pRS316 with increasing concentrations of tris-NDI reveal shortening, possibly due to kinking or knotting of the strands 83

Table 3.4 Concentration-dependent lengthening of pRS316 plasmid with tetra-NDI at extremely low concentrations 84

Table 4.1 Toroid dimensions as measured from sectional analysis of AFM images using half-height measurements for diameters 100

Table 4.2 Dimensions of toroids formed with classical condensing agents collected from the literature. These measurements of diameter and height are in good agreement with those found for poly-NDI. 101

Table 4.3 Condensate structure height at increasing set points and corresponding calculated contact forces. Heights were determined as the average of three sectional analysis along the horizontal, vertical, and diagonal axes of the contact mode image. 106

Table 4.4 Toroid, rod, and strand heights at decreasing set points (increasing interaction forces) as measured by sectional analysis of tapping mode topographical height images 113

Table 4.5 Distribution of condensation structures formed with bis-NDI at 100 μM and 150 μM concentrations. The quantity of well defined condensate structures increased with higher bis-NDI concentration, for example the number of toroids doubles. 120

LIST OF FIGURES

Figure 1.1	Publications in the field of Atomic Force Microscopy from its invention through 2003	2
Figure 1.2	Schematic of the key components of an Atomic Force Microscope	6
Figure 1.3	Atomic force microscopy cantilevers imaged by electron microscopy	8
Figure 1.4	AFM image of pBluescript II' plasmid DNA demonstrating double image due to tip contamination	10
Figure 1.5	Plot of AFM tip path above the sample in constant force mode	15
Figure 1.6	AFM force curves tracking the position of the cantilever as the piezoelectric scanner cycles up and down	17
Figure 1.7	Sequential force curves acquired with the AFM that were obtained during the mechanical unfolding of an elastin-mimetic pepetide	22
Figure 2.1	Structural representations of deoxyribonucleic acid (DNA)	24
Figure 2.2	Depiction of double stranded DNA as a spiral staircase with phosphate and sugar backbones represented by orange banisters and basepairs represented by blue stair steps (pdb 8BNA)	25
Figure 2.3	Structural models of three forms of DNA	26
Figure 2.4	Major and minor grooves formed by DNA helix	28
Figure 2.5	"Central Dogma of Molecular Biology" depicting the key cellular processes of DNA replication and translation	29
Figure 2.6	Models of drug and DNA interactions	34
Figure 2.7	Structural models of spermine binding to the phosphate backbone of DNA at two different viewing angles based on X-ray diffraction at 1.9 Å resolution	35
Figure 2.8	Structural model of dystamycin binding to the minor groove of DNA based on X-ray diffraction at 1.85 Å resolution	36

Figure 2.9	Structural model of phenazine binding to the major groove of DNA based on X-ray diffraction at 2.00 Å resolution	38
Figure 2.10	Structural models of DNA with a) daunomycin mono-intercalation based on X-ray diffraction at 1.50 Å resolution and, b) thiazole orange dimer bis-intercalation based on 40 NMR structures	39
Figure 2.11	Structure of 1,4,5,8-Naphthalenetetracarboxylic diimide (NDI) with peptide linker	43
Figure 2.12	Schematic of threading intercalator with ring moiety (pink) inserted between basepairs and linker structures lying in the minor (green) and major (blue) grooves	45
Figure 2.13	NMR structures of bis-NDI compounds with linker structures a) Alanine-Alanine-Alanine-Lysine in the minor groove, and b) Glycine-Glycine-Glycine-Lysine in the major groove	46
Figure 2.14	Classical DNA condensate morphologies of toroid, sphere, and rod	48
Figure 3.1	NIST certified silicon grating (MikroMasch TGZ02) used for the calibration of the Nanoscope IIIa with J scanner	52
Figure 3.2	Horizontal gel electrophoresis UV fluorescence of ethidium bromide-tagged DNA	57
Figure 3.3	UV-vis spectroscopy absorption curve used to determine DNA concentration based on the Beer-Lambert Law	58
Figure 3.4	Structure and cartoon representation of 1,4,5,8-Naphthalenetetracarboxylic diimide (NDI) with peptide linker	60
Figure 3.5	AFM topographical image of mica with 3-aminopropyletriethoxy silane (APTES) coating demonstrating uneven areas of deposition	63
Figure 3.6	Structural model of bisnaphthalimide LU-79553 with double-stranded oligonucleotide based on 15 NMR structures	67
Figure 3.7	NMR structure of related NDI compound (Gly-Gly-Gly-Lys linker) with a space of one open potential site between intercalating rings	68

Figure 3.8	Theoretical lengthening of pRS316 assuming a nearest neighbor exclusion number (n) of 2, lengthening per intercalation (a) of 0.34 nm, and a binding affinity (Ka) of 4.0×10^4 with plateau approaching maximum length limit	70
Figure 3.9	Histogram of measured lengths of pBluescript II' based on AFM images which correlate well with theoretical B-form length of 1.16 μm versus A-form length of 0.89 μm	71
Figure 3.10	Histogram of measured lengths of pRS315 based on AFM images which correlate well with theoretical B-form length of 1.66 μm versus A-form length of 1.27 μm	72
Figure 3.11	Histograms of pRS316 length progressing with increasing bis-NDI concentration affirming retention of B-form conformation and lengthening due to intercalation	75
Figure 3.12	Plot of actual pRS316 lengthening with increasing bis-NDI concentration with corresponding theoretical curve calculating a nearest neighbor exclusion number (n) of 2.5, lengthening per intercalation (a) of 0.34 nm, and a binding affinity (Ka) of 8.0×10^4	77
Figure 3.13	AFM intermittent contact image of pRS316 plasmid on mica under ambient conditions at increasing bis-NDI concentrations illustrating progression of secondary structures through condensation intermediates to fully formed condensed toroid and rod structures	78
Figure 3.14	DNAse footprint where Cmpd. 1 is the mono-NDI, Cmpd 2 is the bis-NDI, Cmpd. 3 is the tris-NDI, and Cmpd. 4 is the tetra-NDI. Note that no bands occur at the higher concentrations of bis-, tris-, and tetra-NDI indicating protection of the DNA strand from enzymatic activity as would be afforded by condensation.	80
Figure 3.15	AFM images of pRS316 with 50 μM bis-NDI at three incubation temperatures: a) ambient (~25 ºC), b) body temperature (36 ºC), and c) elevated temperature (70 ºC) showing no significant difference in secondary structure produced by temperature	82
Figure 3.16	AFM intermittent contact image of pRS316 plasmid on mica under ambient conditions at increasing tris-NDI concentrations illustrating progression of secondary structures through condensation intermediates to fully formed condensed structures	86

Figure 3.17	AFM intermittent contact image of pRS316 plasmid on mica under ambient conditions at increasing tetra-NDI concentrations illustrating progression of secondary structures through condensation intermediates to fully formed condensed structures	87
Figure 3.18	Models of sequential intercalation of each ring moiety of the bis-, tris- and tetra-NDI molecules representing nearest neighbor exclusion numbers of 2.5, 2.67, and 2.75, respectively where there are three open sites between rings of the same poly-NDI molecule and one open site between molecules	91
Figure 3.19	Models involving groove-binding of the poly-NDI ring either exclusively (a) or in combination with intercalation (b). Lengthening measured with increased concentration of poly-NDI confirms that at least some intercalation is occurring, thus excluding model a.	92
Figure 3.20	Models of inter-strand or intra-strand intercalation (a) of ring moieties in which the rings from one poly-NDI molecule intercalate in remote areas of either the same DNA strand or of different DNA strands. Alternatively, one ring moiety may intercalate while the other may undergo groove binding (b). These models can be interpreted to facilitate loop formation which may serve as a template for condensation or to stabilize condensate structures.	93
Figure 4.1	Portfolio of AFM images (400 nm scan sizes) of representative toroid structures formed by pRS316 and bis-NDI illustrating the diversity of toroid shapes and sizes	97
Figure 4.2	Sectional analysis of toroid with half-height measurements of outer diameter (o.d.) and inner diameter (i.d.)	98
Figure 4.3	Representation of toroid with a) circular cross-section and b) oval cross-sectional	103
Figure 4.4	AFM contact mode images (800 nm scan size) of toroids and rod with increasing force exerted by tip on sample	105
Figure 4.5	Plot of toroid height demonstrating no significant change with increasing contact force between the tip and sample using contact mode AFM	107
Figure 4.6	Force curve from with contact mode experiment exported to a spreadsheet and replotted using a macro developed by Mark Poggi. Retraction curve extrapolated to define rebound point.	109

Figure 4.7	Depiction of force curve with sample compression in the repulsive region (3 and 4) and capillary attraction (6)	110
Figure 4.8	AFM tapping mode height and phase images (600 nm scan size) obtained with a Nanoscope IIIa, Extended base, and J scanner with increasing tip interaction forces	112
Figure 4.9	Plot of toroids, rod, and strand heights demonstrating no significant change with increasing contact force between the tip and sample using tapping mode AFM	114
Figure 4.10	AFM tapping mode height and phase images of toroid using Hi'Res probe (slight multiple image due to small extratips) with sectional analysis height of 4.7 nm	115
Figure 4.11	Force curves at increasing setpoints (related to tip/sample force and pressure) that maintain a slope of unity in the repulsive regime	117
Figure 4.12	Relation of DNA plasmid length to toroid height (bars) and toroid outer diameter (line) based on literature values noted in Table 4.2	119
Figure 4.13	AFM images of condensation intermediates formed by pRS316 with poly-NDI a) toroids and strands with radiating strands, b) toroids and strand with radiating loops, and c) rods bending into pre-toroid-like structures	123
Figure 5.1	Trends in Worldwide R&D Expenditure ($ billions) versus US FDA New Drug Approvals	130
Figure 6.1	Chemical structure of ethidium homodimer-- a bis-intercalator composed of one of the most commonly used intercalators, ethidium, linked by a polyamine similar to spermine, a classical condensing agent	149
Figure 6.2	Representative AFM image of pRS316 with 1.0 μM ethidium bromide on mica illustrating strand lengthening due to intercalation, but no significant change in secondary structure	150
Figure 6.3	AFM images of pRS316 with 0.1 and 0.15 μM ethidium homodimer on mica showing secondary structure formation	150

LIST OF SYMBOLS AND ABBREVIATIONS

™	trademark
®	registered trademark
§	subsection
Å	angstrom
A	adenine
a	lengthening per intercalation event
AFM	Atomic Force Microscopy
Ala	alanine
amp	ampicillin
APTES	3-aminopropyletriethyoxy silane
ATP	adenosine triphosphate
α	thermal expansion coefficient
B	number of basepairs per DNA
bp	basepair
C	Celsius
C	cytosine
CAGR	compound annual growth rate
CD	circular dichroism
Cmpd.	Compound
CSDD	Center for the Study of Drug Design
D	total DNA concentration
DCF	discounted cash flow

div	division
DLS	dynamic light scattering
DNA	deoxyribonucleic acid
DNAse	deoxyribonuclease
ΔZ	scanner movement from setpoint to rebound
F	contact force
FDA	Food and Drug Administration
Fmoc	9-fluorenylmethyoxycarbonyl
FTE	Full Time Equivalent
E	Young's modulus
EDTA	ethylenediaminetetraacetic acid
EM	electron microscopy
EtBr	ethidium bromide
EtDi	ethidium homodimer
ε	extinction coefficient
G	guanine
g force	gravitational force
Gly	glycine
Hz	Hertz
h	total height
Δh	deformation
I	total intercalator concentration
i.d.	inner diameter

IP	intellectual property
J.D.	Juris Doctorate
k	spring constant
Ka	binding affinity
kb	kilobasepair
kDa	kiloDalton
kHz	kiloHertz
L	length of intercalated DNA
Lo	length of un-intercalated DNA
l	length
LB	Luria-Bertani base
Lys	lysine
M^{-1}	inverse Molar
m	meter
M.B.A.	Master of Business Administration
MEMS	Micro-Electro-Mechanical Systems
mL	milliliter
mM	millimolar
mm	millimeter
MPa	megaPascal
mRNA	messenger ribonucleic acid
mV	milliVolt
MΩ	megaOhm

μg	microgram
μL	microliter
μm	micron
N	Newton
n	nearest neighbor exclusion number
ND	not determined
NDA	new drug approvals
NDI	1,4,5,8-naphthalenetetracarboxylic diimide
NIST	National Institute of Standards and Technology
nm	nanometer
NMR	Nuclear Magnetic Resonance
nN	nanoNewton
NPV	Net Present Value
o.d.	outer diameter
OTC	over-the-counter drugs
OTL	Office of Technology Licensing
P	pressure
PCR	polymerase chain reaction
pdb	Protein Data Base
PEG	polyethylene glycol
psi	pounds per square inch
PTO	Patent and Trademark Office
R&D	research and development

r.h.	relative humidity
RMS	root mean square
RNA	ribonucleic acid
rpm	revolutions per minute
SDS	sodium dodecyl sulfate
SEM	scanning electron microscopy
SPM	Scanning Probe Microscopy
STM	Scanning Tunneling Microscopy
T	temperature
T	thymine
t	thickness
TBE	Tris Borate EDTA
TEM	Transmission Electron Microscopy
TI:GER	Technological Innovation: Generating Economics Results program
TOTO	thiazole orange dimmer
USA	United States of America
U.S.C.	United States Code
UV	ultraviolet
UV-vis	ultraviolet-visible
V	Volts
VC	venture capitalists
w	width
WLC	worm-like chain

x_0	piezoelectric original dimension
ΔZ	movement of piezoscanner from setpoint to rebound

SUMMARY

Atomic force microscopy (AFM) is a particularly useful tool for obtaining structural information about drug-nucleic acid interactions. The mode of drug binding— intercalation versus groove binding— can be determined from images acquired on individual DNA molecules as the length of a DNA molecule increases in direct proportion to the number of intercalators bound to it.

The efforts of this research were directed toward elucidating the mode of binding of a series of drugs based on multimers of naphthalenetetracarboxyl diimide (NDI) interacting with a linearized DNA plasmid. During the course of the investigation, DNA intercalation was confirmed as the mode of binding and the binding affinity estimated. Unexpectedly, concentration-dependent formation of secondary DNA structures including condensates was observed. DNA toroids, spheres, and rods were imaged and measured. Conformations that are believed to be intermediate condensate forms were also identified at lower poly-NDI concentrations. Models for the DNA condensation process have been proposed.

Ultimately, this research furthers the understanding of DNA condensation which can be applied to gene delivery systems and anti-viral agents. It may also help direct the development of better drugs based on the insight of poly-intercalators interactions with DNA.

CHAPTER 1

ATOMIC FORCE MICROSCOPY

The following chapter was written as a general overview of Atomic Force Microscopy and will be published in the Encyclopedia of Analytical Chemistry (Elsevier, in press).

History and Background

Scanning Probe Microscopy (SPM) is a family of related techniques that provide information about atomic scale structure and processes. The first of these to be developed was Scanning Tunneling Microscopy (STM) by Gerd Binning and Heinrich Rohrer at IBM Zurich in 1981 [1]. They were awarded the Nobel Prize in Physics in 1986 for their invention. Atomic Force Microscopy (AFM) is another SPM technique invented by Gerd Binning, Calvin Quate, and Christopher Gerber in 1986 to expand the types of surfaces on which atomic scale information can be obtained [2]. Digital Instruments (Santa Barbara, California, USA) produced the first commercial AFM in 1989.

These powerful techniques and others have been rapidly adopted by the scientific community and applied in numerous fields ranging from biology to materials science. The number of publications and patents has increased exponentially over the last twenty years (Figure 1.1). SPM accounted for 8% of the microscopy market in 2002 worth $US 78 million and was the most rapidly growing segment.

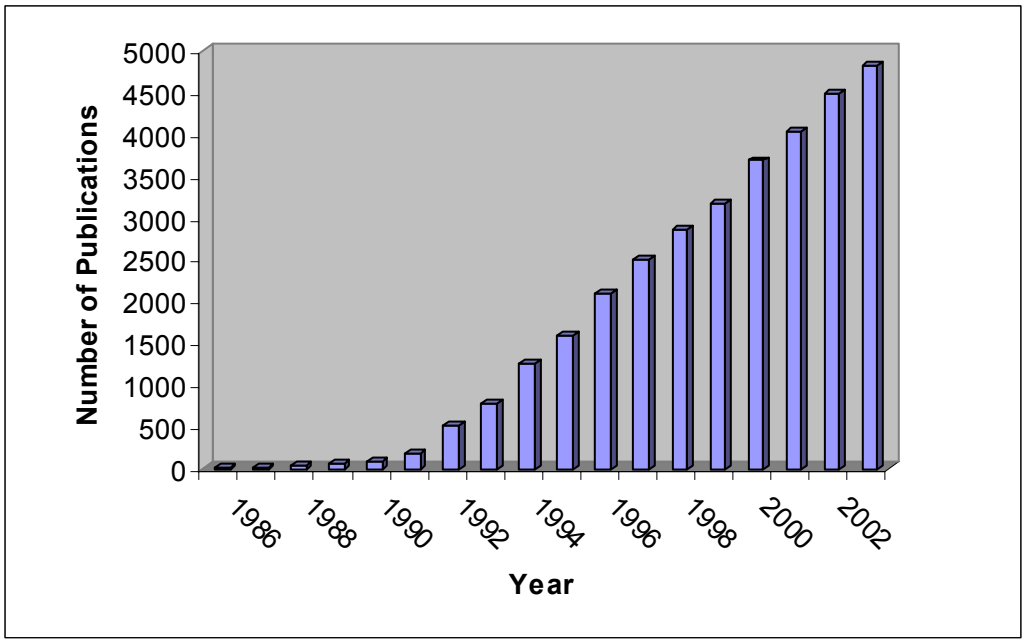

Figure 1.1 Publications in the field of Atomic Force Microscopy from its invention through 2003 (Data based on search in SciFinder Scholar 2004; American Chemical Society.)

The largest producer of SPM instruments is Veeco Instruments, Inc. (Santa Barbara, California, US), which acquired several AFM producers including Digital Instruments, Topometrix and Park Scientific Instruments. Asylum Research, Pacific Nanotechnology, JEOL, Omicron NanoTechnology and Nanonics Imaging are other major manufacturers (Table 1.1).

AFM Capabilities

AFM can achieve atomic resolution under certain conditions; however, surface features are typically resolved on the nanometer scale laterally and the angstrom scale vertically [3]. This resolution is comparable to that of transmission electron microscopy (TEM). Resolution of AFM depends on tip shape, scan domain, and number of measurements per scan. Unlike many other forms of microscopy, AFM does not require any stains, contrast agents, or conductive coatings that can cause partial obstruction of the actual sample. In addition, AFM sample preparation is fairly simple and quick. AFM is a nondestructive method that allows the sample to be reused for additional analyses over time.

AFM has advantages over other techniques such as Nuclear Magnetic Resonance (NMR), X-ray crystallography, and Scanning Tunneling Microscopy (STM). These other techniques lack AFM's ability to image a variety of materials (i.e., nonconductive, magnetic, biological) under a variety of environmental conditions (i.e., ambient air, various gases, different humidity levels and temperatures). AFM provides the ability to

Table 1.1 Scanning Probe Microscope instrument and cantilever manufacturers

Manufacturer Name	Headquarters Location	Website
Accurion	Menlo Park, California, USA	www.accurion.com
Asylum Research Corporation	Santa Barbara, California, USA	www.AsylumResearch.com
Independent Research Engineering	Moscow, Russia	www.mtu-net.ru/nanoscan
JEOL Europe Ltd. / JEOL USA, Inc.	Japan	www.jeol.com
JPK Instruments AG	Berlin, Germany	www.jpk.com
Klocke Nanotechnik	Aachen, Germany	www.nanomoter.de
Molecular Imaging	Tempe, Arizona, USA	www.molec.com
MikroMasch	Tallinn, Estonia	www.spmtips.com
Nanofactory Instruments	Goteborg, Sweden	www.nanofactory.com
Nanonics Imaging Ltd.	Jerusalem, Israel	www.nanonics.co.il
Nanosurf AG	Basel, Switzerland	www.nanosurf.com
Novascan Technologies	Ames, Iowa, USA	www.novascan.com
NT-MDT Co.	Moscow, Russia	www.ntmdt.ru
Omicron NanoTechnology GmbH	Taunusstein, Germany	www.omicron-instruments.com
Pacific Nanotechnology, Inc.	Santa Clara, California, USA	www.pacificnanotech.com
PSIA	Sungnam, Korea	www.advancedspm.com
Quesant Instruments Corp.	Agoura Hills, California, USA	www.quesant.com
RHK Technology, Inc.	Troy, Michigan, USA	www.rhk-tech.com
Surface Imaging Systems GmbH	Herzogenrath, Germany	www.sis-gmbh.com
Triple-O Microscopy GmbH	Potsdam, Germany	www.triple-o.de
Veeco Instruments, Inc.	Woodbury, New York, USA	www.veeco.com
WITec	Ulm, Germany; Savoy, Illinois, USA	www.witec.de; www.WITec-Instruments.com

look at individual interactions and structural conformations instead of the average within a mixture.

AFM Instrumentation

AFM measures the surface topography of a sample on a nanometer scale and the attractive and repulsive forces on a picoNewton scale [3]. An analogy can be made between AFM and a blind person using a cane to navigate along a landscape. The blind person strokes or taps their cane along the ground to feel where the ground is higher or lower, as well as softer or harder and rougher or smoother. In the same way, AFM is able to feel the surface topography and force characteristics of the sample. Figure 1.2 shows a general scheme of the key components of an AFM. AFM works by scanning a sample under an extremely sharp tip (ideally atomically sharp) integrated on the end of a cantilever. The cantilever bends up or down as it contacts features on the surface. The most common method to measure these small movements uses a laser beam focused on the end of the cantilever that is reflected onto a position sensitive detector [4]. Changes in the angle of the cantilever, induced by changes in sample topography, result in different voltage levels out of the detector. These voltages are sent to a computer for processing and display of the topographic image. The user can enter control parameters such as the scan size (the range that the probe tip will travel across the sample), scan rate of the tip above the surface, and feedback control (to maintain a constant height between the tip and substrate) into the computer interface. The commands from the user interface are then sent to a control module that converts these commands (such as a metric scan size) into a series of voltages to be sent to the microscope. A sample-mounting block

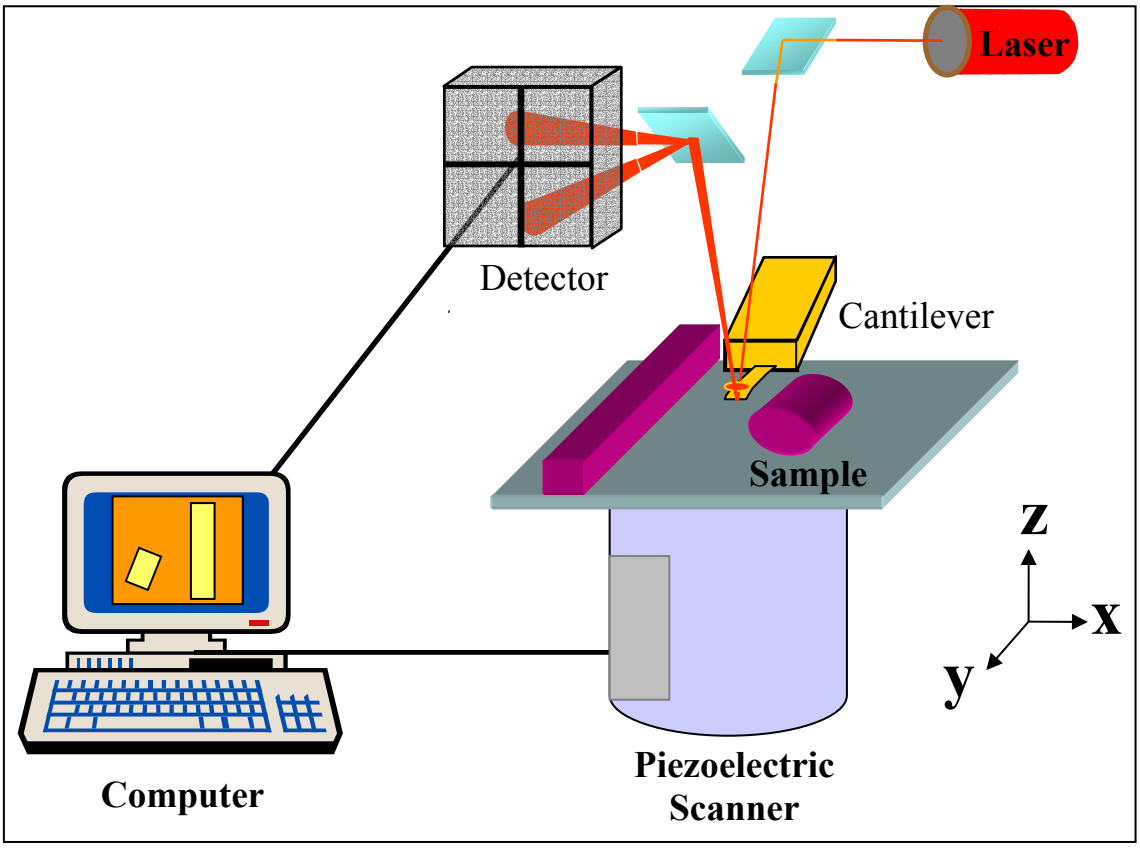

Figure 1.2 Schematic of the key components of an Atomic Force Microscope

holds the sample rigidly in place. Rigidity needs to be emphasized because AFM requires minimization of all sources of electrical and mechanical noise [5]. Typically, electrical wires in the microscope are fully shielded and all mechanical fixtures are held tightly in place. The entire microscope is mounted on an anti-vibration apparatus. These can range from simple homemade anti-vibration units such as a concrete block hanging from bungee-cords (~$100) to anti-vibration tables that have pneumatically suspended tabletops (> $2,500). If these types of noise are not controlled or reduced, visualizing atomic-scale features is impossible.

The AFM instrument system described above and shown in Figure 1.2 is the simplest and most commonly used in commercial instruments. Variations of this scheme include scanning the tip over the sample surface to allow analysis of larger samples and the use of different detectors to allow analysis of rougher samples [6].

Cantilevers

Cantilevers are commercially produced from silicon and silicon nitride using microfabrication processes similar to those employed in integrated circuit manufacture [7]. Cantilevers are often coated with metal on the top side to enhance laser reflection. There are two primary geometries of AFM cantilevers- triangular and rectangular (Figure 1.3a and b). Rectangular cantilevers are susceptible to torsional bending during contact mode imaging whereas, triangular cantilevers have been designed to reduce the lateral forces exerted on the cantilever.

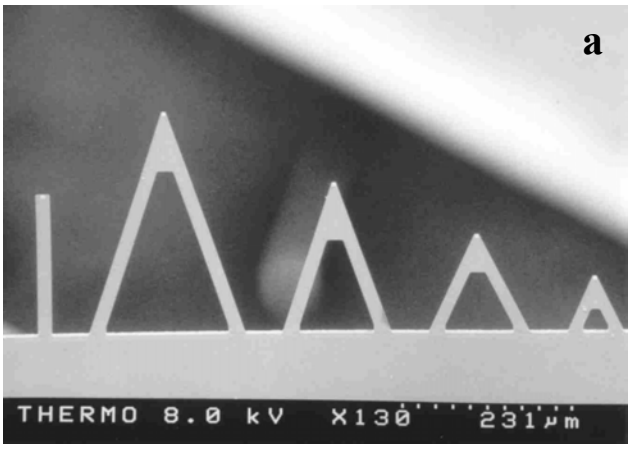

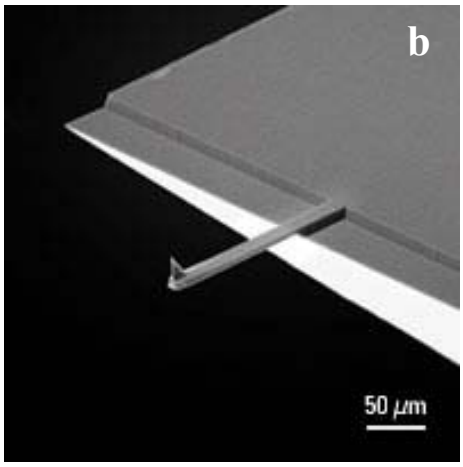

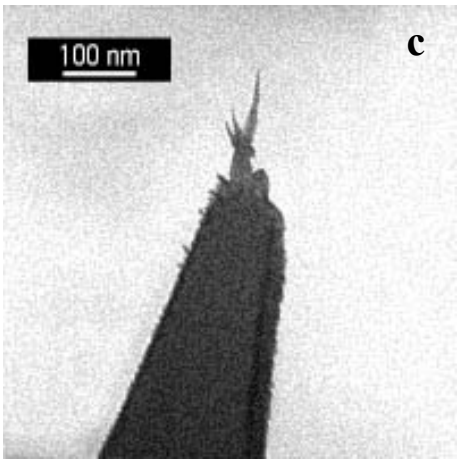

Figure 1.3 Atomic force microscopy cantilevers imaged by electron microscopy; a) Triangular cantilevers (Courtesy of Veeco Instruments, Inc.), b) Rectangular cantilever (Courtesy of MikroMasch), c) Hi'Res cantilever (Courtesy of MikroMasch)

The fundamental resonant frequency of the cantilever should be high in order to avoid interference from building vibrations and acoustic noise [8]. Thermal noise from the cantilever can limit the sensitivity of the AFM and should be minimized by using shorter length cantilevers. A shorter length cantilever also provides greater angular displacement of the laser resulting in greater resolution. The spring constant (k) of a rectangular cantilever is calculated from its geometry (w = width, l = length, and t = thickness) and material properties (Young's modulus, E) [5]. The equation for the spring constant of a rectangular cantilever is:

$$k = \frac{Ewt^3}{4l^3} \qquad \text{Equation 1.1}$$

The spring constant increases with cantilever width and thickness but decreases with cantilever length. Typically stiffer cantilevers are used for dynamic imaging modes [8].

The geometry of the cantilever tip is critical to the quality of the AFM image and for achieving nanoscale images [7]. The overall tip geometry is often square pyramidal resulting from an etching process. The aspect ratio (height to width ratio) of the tip is important for imaging rough samples in order to fully contact recesses. The tip sharpness, or the radius of curvature at the apex, will produce artifacts in the final image. Care must be taken to minimize the possibility of creating a double-tip where multiple points of the probe interact with the sample. This can lead to tip-induced artifacts in the topographical image (Figure 1.4). Recently, carbon nanotubes have become popular tips because of their high aspect ratio, small radius of curvature, and durability (Figure 1.3c) [9]. Tips are often functionalized in order to study tip to sample interactions or to conduct chemically sensitive measurements [10].

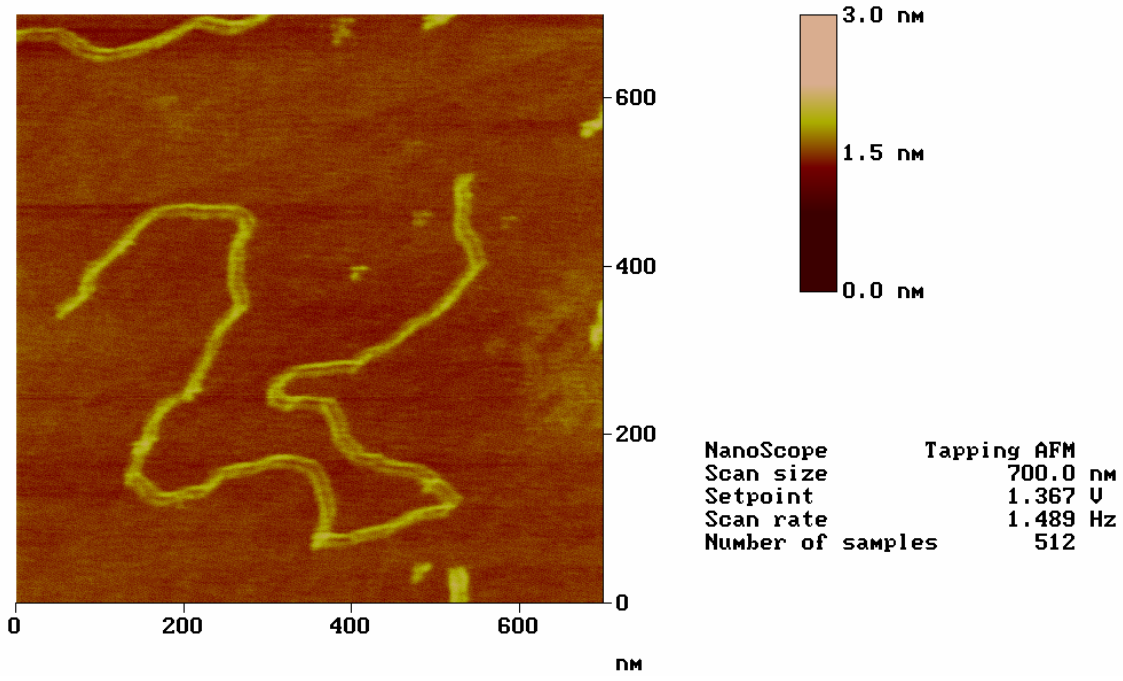

Figure 1.4 AFM image of pBluescript II' plasmid DNA demonstrating double image due to tip contamination

Arrays of parallel cantilevers have been developed for use in sensor applications, data storage, and increasing scan sizes and imaging speed [6].

Piezoelectric Scanner

Piezoelectrics are materials whose crystal structure undergoes a physical change due to an applied electric field. If the voltages that are applied to a piezoelectric are precisely controlled, extremely precise movements can be performed. The geometries of the piezoelectric devices used in AFM are bars, bimorphs or tubes; the most commonly used are tubular [11]. These devices operate at a high resonant frequency, enabling high scan rates. Thermal isolation of the piezoelectric elements is necessary since these ceramics are also sensitive to temperature fluctuation. The sensitivity of a piezoelectric to temperature changes is defined as:

$$\frac{\Delta x}{x_o} = \Delta\alpha * \Delta T \qquad \text{Equation 1.2}$$

where x_0 is the original dimension of the piezoelectric, $\Delta\alpha$ is the difference between thermal expansion coefficients of the different materials and ΔT is the temperature variation [11]. Piezoelectric scanners exhibit both linear and nonlinear responses to an applied voltage. As a result, careful scanner calibration is required. Scanner dimensions must be carefully matched with the desired image domain.

Typically there are two types of scanner placement: 1) a sample is mounted directly to the piezoelectric scanner and rastered underneath the cantilever, 2) the cantilever is

mounted to a scanner tube and rastered over a sample fixed below it [4]. The latter case is advantageous in imaging larger samples and increases the speed of imaging.

Alternatively, the cantilever can be scanned over the sample in the x and y directions and controlled in the z direction using an integrated piezoelectric actuator on the cantilever. This is done by coating the cantilever with a thin film of zinc oxide which a voltage is applied across to yield bending [12]. This system is advantageous in imaging larger samples and increasing the speed of imaging.

The scanner design results in bowing of the image due to the bending motion of the scanner cylinder. This results in the tip moving out of the plane of the sample and the feedback loop causes the scanner to contract in an attempt to maintain a constant deflection [11]. The effect is more predominant in large scan sizes. This artifact is customarily removed from the image using graphics software to mathematically "flatten" the images.

It is imperative that movements of the scanner be frequently calibrated against a certified standard. This will allow users to compare results from one instrument to the next and, more importantly, instills confidence in the length scales of the measured topographical features. The user must remain cognizant that they cannot visually see the sample. The image displayed is a pictorial representation of the changes in cantilever deflection as a function of movement in the scanner. If movement of the scanner is poorly calibrated then there is little reliability in image feature dimensions.

Detectors

The original AFM used an STM to sense the movement of the cantilever in response to interactions with the sample [1]. Optical detectors in most commercial AFM have supplanted this type of electrical detector [4]. The most widely used detection system uses a laser beam reflected off the end of the cantilever onto a position sensitive detector. A change in the angle of the cantilever moves the spot on the detector, producing a change in the voltage sent from the detector and used to generate the topological map.

Interferometry is another detection system where a laser beam is reflected off the end of the cantilever [13]. The phase change of the reflected laser beam is then compared to that of a standard to determine the change in cantilever position. This type of detection offers a better signal to noise ratio but it is more difficult to set up and requires better vibrational and acoustic isolation.

Integration of the detector into the cantilever has also been accomplished using the piezoresistive properties of silica [14]. This is beneficial for samples that are light sensitive and following the movements of cantilevers in an array. It can be used in conjunction with the integrated piezoelectric actuator; however, it can be difficult to decouple the signals.

AFM Operational Modes

Atomic Force Microscopy can be operated in several modes to optimize topographical imaging of different types of samples, to explore different surface properties of samples, or to modify the surface [5, 11, 15].

Contact Mode

Contact mode is the simplest form of AFM. The cantilever tip is brought into intimate contact with the sample surface where the force exerted on the tip is constantly maintained. The difference between the actual force and a predefined setpoint force is corrected via a closed-loop feedback system.

Proportional and integral gains of the instrument can be set by the user to adjust the performance of the feedback system [3]. The proportional gain is multiplied by the difference between the actual force and the setpoint. The integral gain is the time weight that is integrated over the difference between the actual force and the setpoint. If the gains are too high, feedback oscillations may excite the resonance frequency of the scanner. If the gains are too low, resolution is poor due to slow reaction of the feedback loop .

When operating in the constant force mode, the force between the tip and the sample are kept constant. As the tip travels over high or low areas, the changes in the scanner movement in the z-direction are plotted as a function of the x and y position of the scanner (Figure 1.5). The constant force mode requires that the controller maintains a

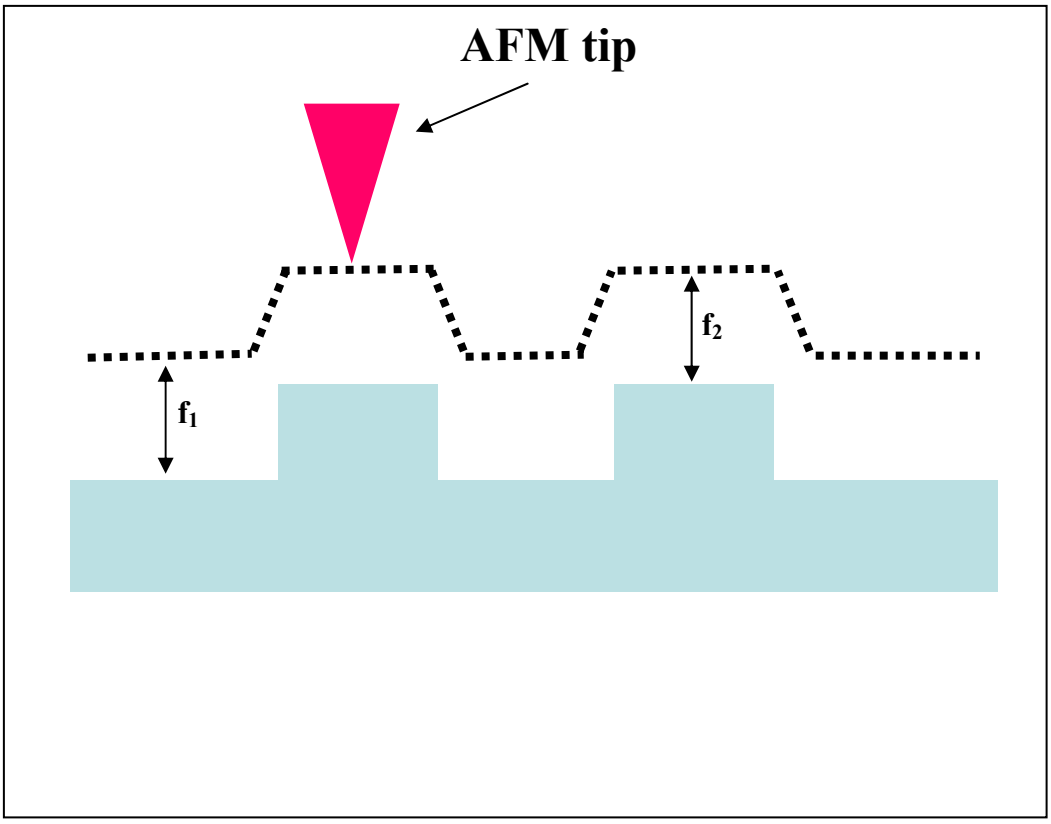

Figure 1.5 Plot of AFM tip path above the sample in constant force mode

constant separation distance between the tip and sample. This is accomplished via the integration of a feedback loop between the scanner and the controller. Thus, the position of the tip is being monitored and if, for example, the tip force gets too high during constant force mode, the controller will increase the separation between the tip and the substrate to maintain the set force level.

Force curves are used to interpret the interaction of the cantilever tip as it comes into contact with the sample [16]. Typical force curves with tapping mode and contact mode are depicted in Figure 1.6. Force curves are obtained by disabling the scanner movement in the x and y directions and oscillating the scanner in the z-direction. As the tip approaches the sample, initially no cantilever bending is exhibited. Once the cantilever tip is extremely close to the sample, the cantilever will be pulled down due to the van der Waals interactions between the tip and the substrate. This jump to contact can also be induced by the presence of a thin hydration layer on the surface. After the tip is in contact with the sample, the sample continues to move upward, which bends the cantilever up. When the sample is then retracted from the tip, the cantilever straightens. However, instead of being released from the surface at the same point as it came in contact, the tip may be held on the surface by the attractive or adhesive forces thus causing the cantilever to bend down. Finally, when the restoring force of the cantilever exceeds the attractive or adhesive forces, the tip releases from the substrate surface and the cantilever returns to its original position.

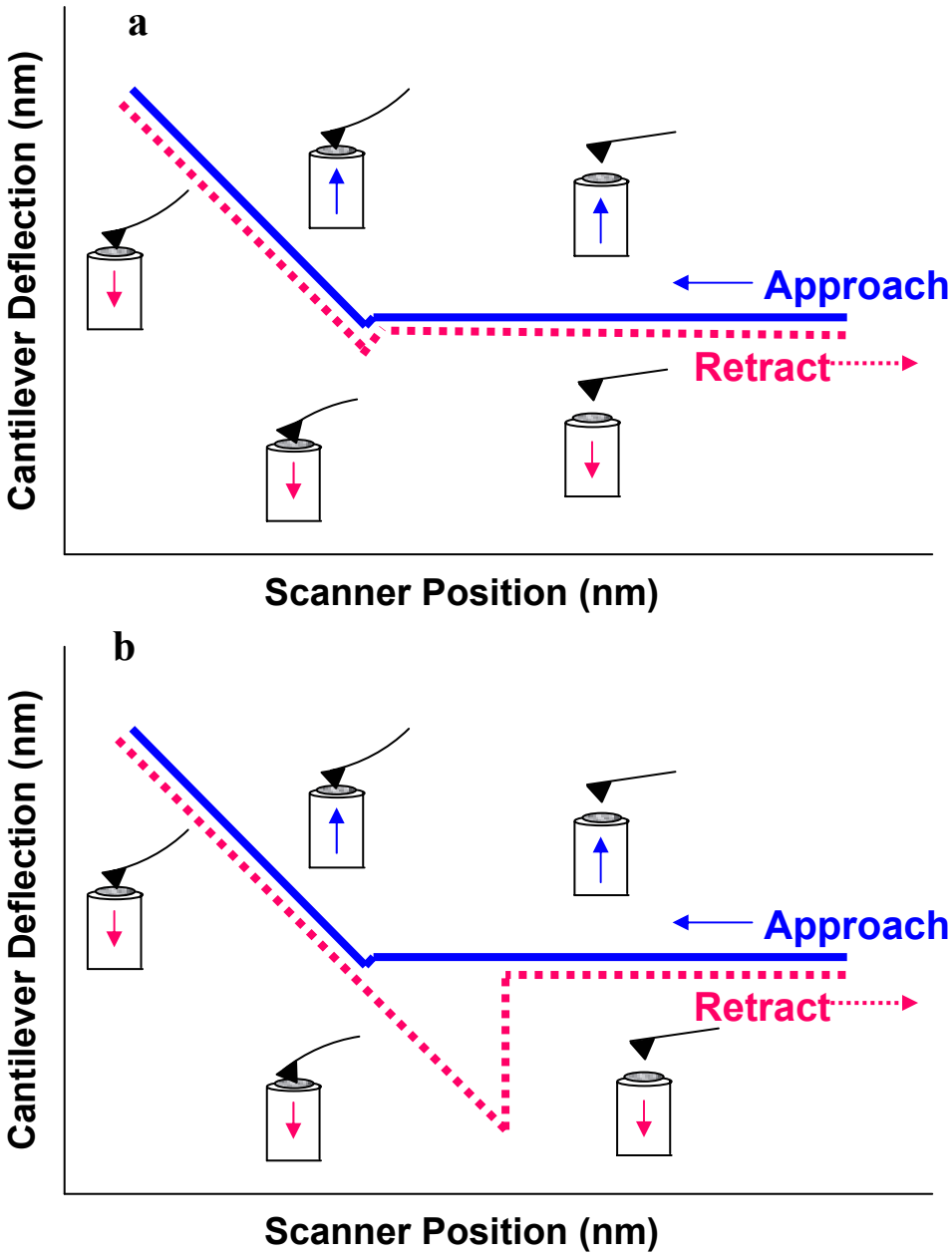

Figure 1.6 AFM force curves tracking the position of the cantilever as the piezoelectric scanner cycles up and down: a) typical tapping mode force curve with limited attractive forces between tip and sample, and b) force curve for highly hydrated sample or contaminated tip demonstrating greater attractive forces between tip and sample

Friction Force Imaging

Friction force mode is an extension of contact mode to measure the local variations of adhesion that may exist between the cantilever tip and the substrate [17]. Lateral forces on the tip cause torsional bending of the cantilever that is detected by horizontal movement of the laser spot on the detector.

Force Modulation Imaging

A relatively new contact mode technique is force modulation imaging [18]. This scanning probe method elucidates both topological and the corresponding elastic properties of a substrate. Force modulation involves placing a bimorph (or piezoelectric) actuator in contact with a cantilever chip. The actuator is then driven at its resonant frequency and when this cantilever/actuator is brought into contact with the sample, the cantilever tip indents the sample. Areas that are more difficult to indent will require that a higher driving voltage be applied to the actuator (representative of a stiff surface) or a very low driving voltage may need to be applied to indent a pliant area of the substrate. This technique has been integral in characterizing the mechanical and topological properties of composite materials.

Noncontact Mode

Noncontact or Dynamic Force mode focuses on longer-range molecular forces [19]. The cantilever is driven to oscillate at its resonance frequency by a piezoactuator. The surface topography is measured by the shift in cantilever frequency based on tip/sample interactions.

Intermittent Contact Mode

Intermittent contact mode was developed by Zhong et al. at Bell Labs in 1993 [20]. Intermittent contact or TappingMode™ is similar to noncontact mode in that the cantilever is driven to oscillate at its resonance frequency [21]. However, the change in oscillation amplitude is used as the control parameter, in comparison to the change in oscillation frequency in noncontact mode. The root mean square (RMS) value of the detector deflection is used to control the tip/sample distance via the feedback loop.

The major advantage of the intermittent contact mode is that lateral forces are greatly reduced [22]. This facilitates its use with soft molecules or molecules that are not strongly attached to the surface. A low drive amplitude and low RMS force are desired to minimize impact on soft molecules; however they must be sufficient to overcome attractive capillary forces. This problem can be resolved by imaging under fluid. Imaging under fluid also provides the opportunity to examine interactions between the substrate and molecules in the liquid environment.

Phase Imaging

Phase imaging is an extension of intermittent contact mode to measure surface properties such as adhesion, friction, and elasticity [23]. Phase imaging detects the phase shift of the cantilever oscillation, which is related to the surface rigidity. Phase shifts above 90 degrees are due to attractive interactions, while phase shifts below 90 degrees are due to repulsive interactions.

AFM Applications

Atomic force microscopy has been applied to similar fields as STM; however AFM enables scientists to visualize nonconducting surfaces that were not possible with STM. This analytical tool has elucidated and coupled mechanical properties with surface morphology. Biological researchers have utilized AFM for studying DNA interactions, protein conformations, enzyme reactions, and cell membrane structures [24-27]. Material scientists have used AFM to study surface properties of polymers, plastics and coatings [6, 28-30].

The AFM has more recently found an application aside from surface characterization. It has been used to test the mechanical properties of a myriad of biological molecules and polymers (single molecule mechanical testing) [31, 32]. The AFM has also been used to measure nano-scale adhesion that may exist between a chemically modified cantilever and a substrate (typically called chemical force microscopy) [10, 33]. The experimental design for the single molecule mechanical testing is an elegant example of the chemist's ability to chemically tailor surfaces on the nano-scale. Generally these experiments are done by tethering a molecule on either a substrate or the end of the cantilever tip via coupling chemistry. The free end of the molecule possesses a reactive group that couples with the opposing surface. The cantilever tip is brought into close proximity with the substrate, leading to the coupling of the free end of the molecule and the surface bound reactive group. The substrate is then pulled away from the cantilever, leading to the mechanical unfolding of the anchored molecule. These experiments are interpreted by closely analyzing the force curves that are generated during the pulling process. Figure

1.7 represents the tensile loading of an elastin-mimetic peptide molecule that is repetitively pulled.

AFM has been employed in manufacturing and quality control of microelectronics, including semiconductor silicon wafers, MEMS devices, CDs/DVDs and computer hard disks [34-36]. Often the defects are smaller than the wavelength of light making optical analysis ineffective.

An evolving area of AFM application is nanomanipulation in which the AFM tip modifies the sample surface at an extremely small scale. This can be achieved by frictional wear, controlled surface oxidation, and/or deliberate material transport between two surfaces. With the latter, molecules or cells can be attached to the AFM tip and transferred to the opposing surface at specific locations. Alternatively, thermal patterning of substrates can be achieved by contacting a heated cantilever tip with the surface. Potential applications include preparation of ultra-high density data storage devices and molecular machines.

In summary, scanning probe microscopy has revolutionized the understanding of chemical phenomena on the nanoscale and will continue to do so in the future.

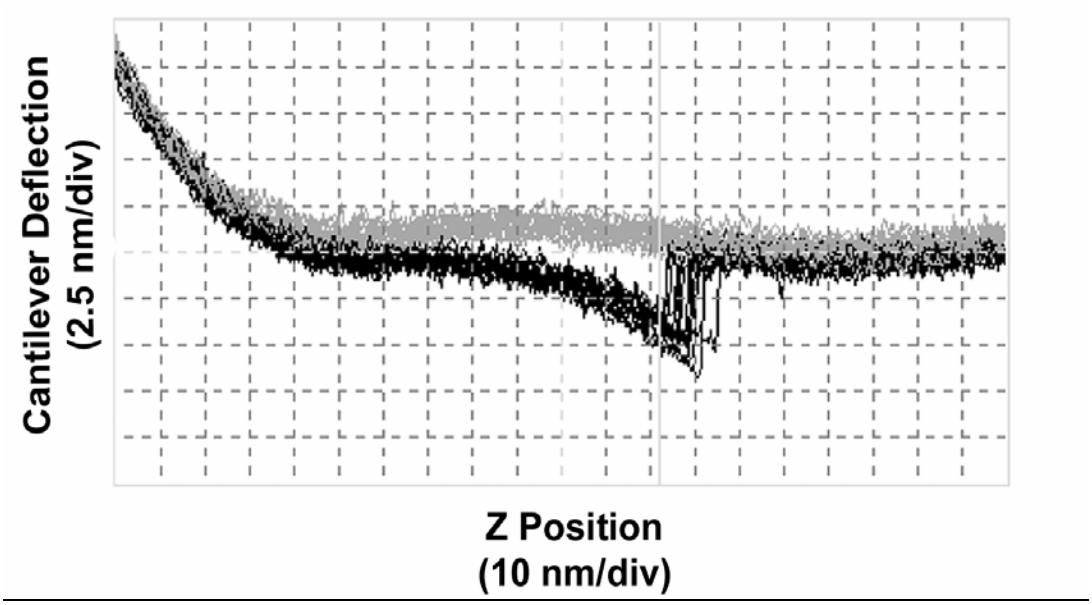

Figure 1.7 Sequential force curves acquired with the AFM that were obtained during the mechanical unfolding of an elastin-mimetic pepetide (data from Mark Poggi)

CHAPTER 2

DNA INTERCALATION AND CONDENSATION

DNA

Deoxyribonucleic acid (DNA) is the "polymer of life". DNA is composed of units of purine and pyrimidine bases attached to a backbone of a 5-carbon sugar (dexoyribose) alternating with a phosphate group. The purine bases— adenine (A) and guanine (G), and pyrimidine bases— thymine (T) and cytosine (C) are paired together A to T and G to C to allow replication of the DNA code (Figure 2.1a). The bases are made up of nitrogen and carbon atoms arranged in planar ring structures (Figure 2.1b). DNA is typically double stranded in a "spiral staircase" structure with the paired bases forming the "steps" (Figure 2.2).

DNA can be found in three principal forms: A, B, and Z (Figure 2.3) [37]. The A form occurs under anhydrous conditions (<75% relative humidity) and is found in bacterial spores. The A form has 11 basepairs per helical turn, a helical rise per basepair of 0.26 nm, and a diameter of 2.6 nm. The B form is the most common form found under natural conditions. It has 10 basepairs per helical turn, a helical rise per basepair of 0.34 nm, and a diameter of 2.0 nm. Both the A and B forms are right-handed helices, however, the Z form is a left handed helix and is believed to serve as a genetic switch. The Z form has 12 basepairs per helical turn, a helical rise per basepair of 0.37 nm, and a diameter of 1.8 nm.

a

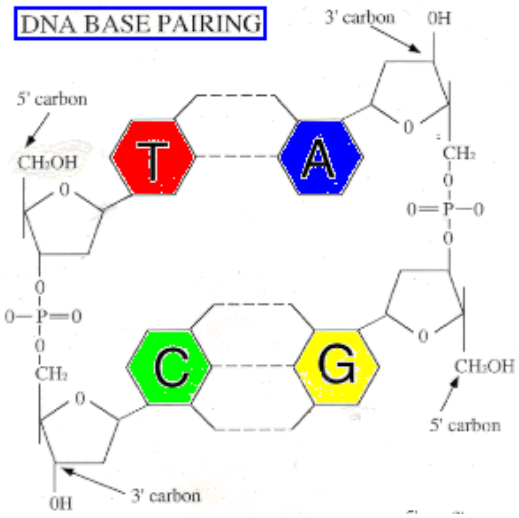

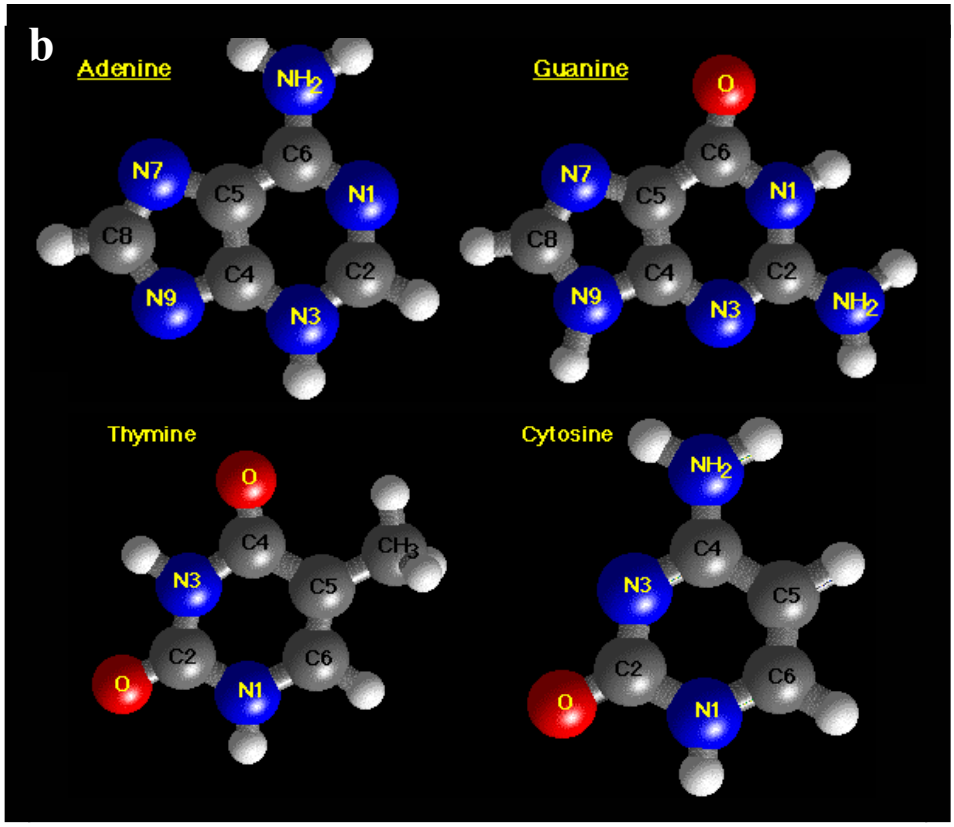

Figure 2.1 Structural representations of deoxyribonucleic acid (DNA) a) backbone and basepairs, b) chemical structures of purine and pyrimidine bases: (A) adenine, (G) guanine, (T) thymine, and (C) cytosine

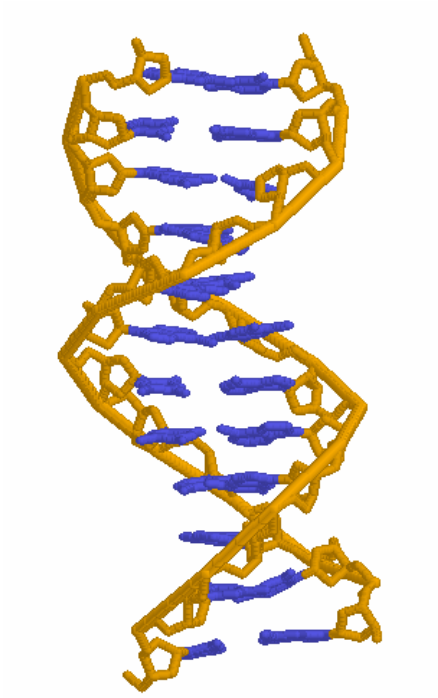

Figure 2.2 Depiction of double stranded DNA as a spiral staircase with phosphate and sugar backbones represented by orange banisters and basepairs represented by blue stair steps (pdb 8BNA)[38, 39]

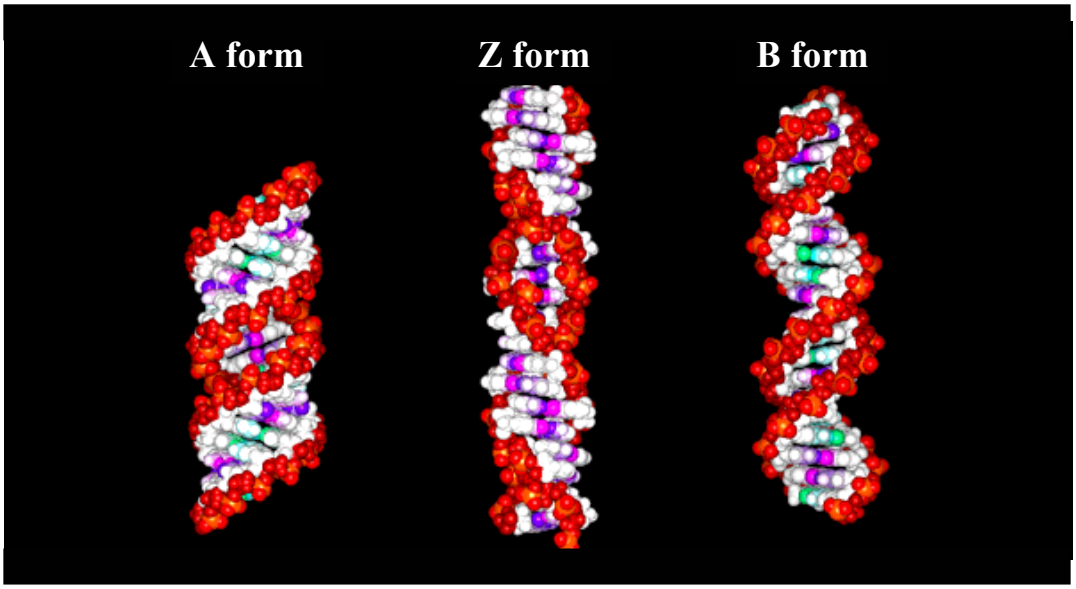

Source: www.lmb.uni-muenchen.de/groups/Biostruc/chap-08/chap-08-slides.html

Figure 2.3 Structural models of the three forms of DNA

A major and minor groove traversing the spiral structure are formed by the DNA backbone (Figure 2.4a). The major and minor grooves differ not only in size, but also in polarity and chemistry [40]. The chemistries present in the grooves are specific to the basepairs which can lead to sequence specific binding in the grooves. In the major groove A-T has a sequence of acceptor-donor-acceptor and G-C has a sequence of acceptor-acceptor-donor (Figure 2.4b). The major groove has more binding sites and exhibits directionality (e.g. AT vs. TA).

DNA is a polyanion which attracts positively-charged counterions such as calcium and magnesium ions in buffer solutions to shield the electrostatic charges. DNA is a fairly stiff molecule with a persistence length of about 50 nm. According to the IUPAC Compendium of Macromolecular Nomenclature, persistence length is "the average projection of the end-to-end vector on the tangent to the chain contour at a chain end in the limit of infinite chain length" [41]. DNA can be treated mathematically using the worm-like chain (WLC) model [42].

DNA serves two central roles. First, it maintains the genetic information and is replicated to pass this information to each new cell. Second, it contains the code which is translated into RNA which is then transcribed into proteins (Figure 2.5). This has become known as the central dogma of molecular biology.

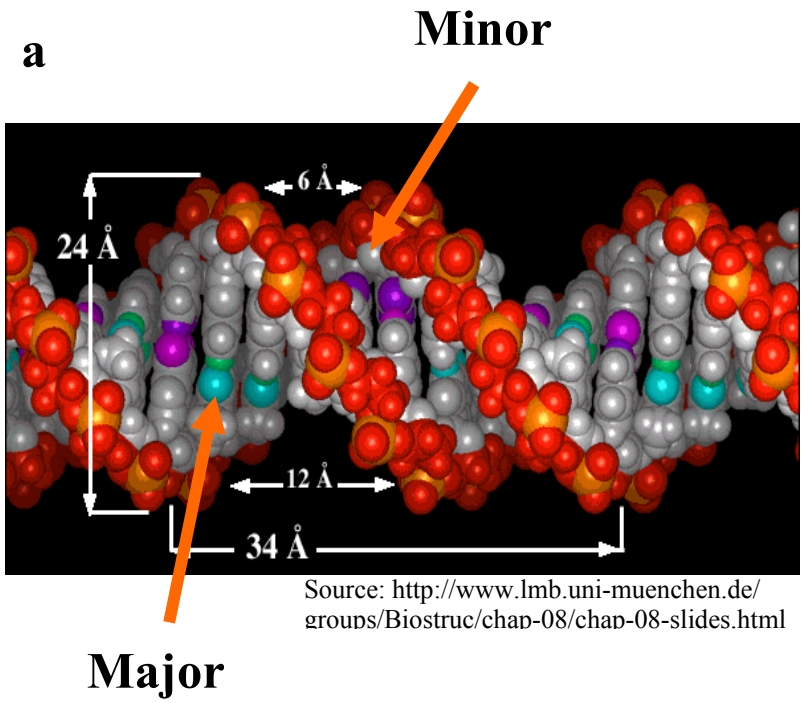

Source: http://www.lmb.uni-muenchen.de/groups/Biostruc/chap-08/chap-08-slides.html

Figure 2.4 Major and minor grooves formed by DNA helix– a) relative groove size illustrated with space-filling model, b) chemical structure of basepairs extending into grooves

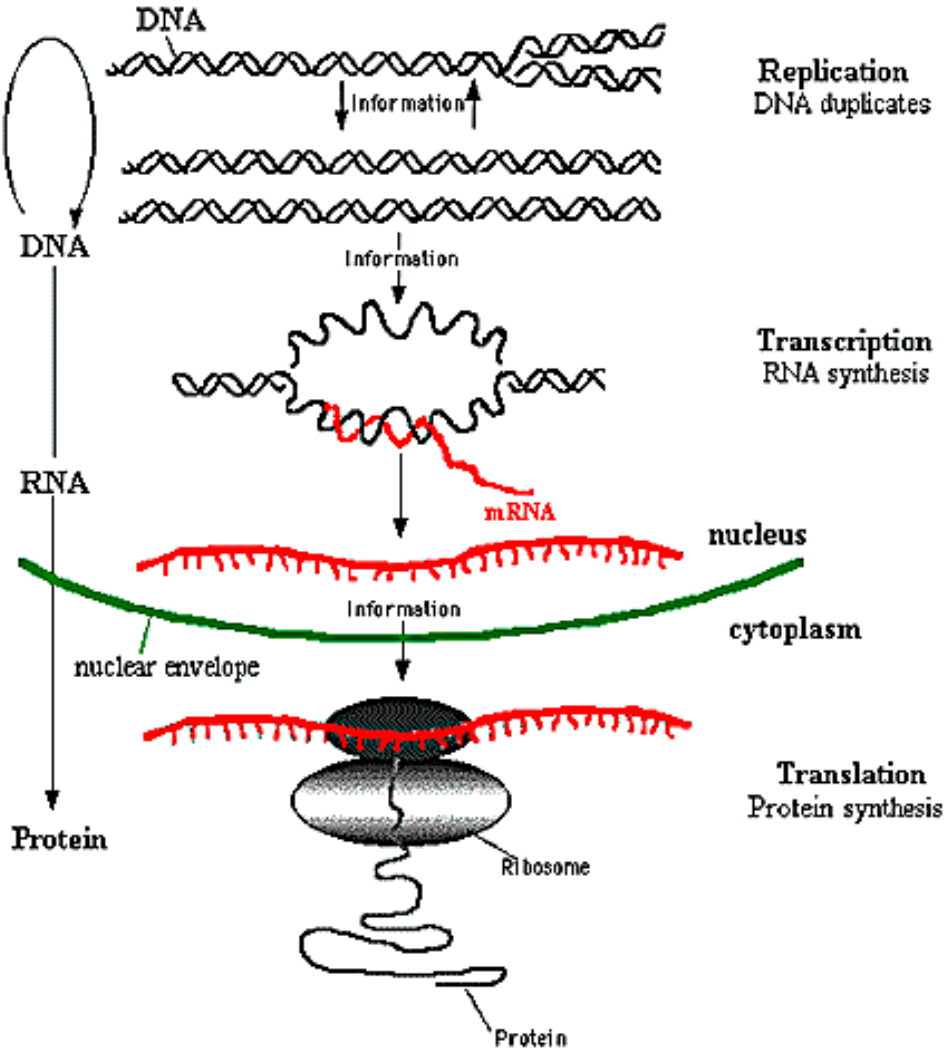

Figure 2.5 The "Central Dogma of Molecular Biology" depicting the key cellular processes of DNA replication and translation (Access Excellence at National Health Museum) [43]

DNA and Drug Interactions

Anti-cancer therapies often target the DNA to inhibit the rapid replication of cancer cells. Many diseases such as diabetes, Lupus, hemophilia, Huntington's disease, and Alzheimer's disease may be traced to over- or under-production of proteins or production of mutated proteins. DNA is the genetic material that codes for proteins; therefore, drug interactions with DNA which can affect this process are potential treatments for these types of diseases. The mode of action of some drugs for the treatment of cancer, genetic disorders, and viral diseases is thought to be based on their binding to DNA and their modification of DNA activity. The activity of the drug is often linked to the binding geometry. Thus, the potential activity of a drug could be assessed by detecting the DNA binding location and fit of the drug candidate. An analytical technique to elucidate the mode of DNA/drug interaction could be important for the design of advanced drugs.

Analytical Techniques

Currently, drug developers assess the interactions of drugs with DNA through indirect assays, computer modeling, and clinical trials. These methods do not provide the insight required to rationally design or screen the compounds. Most clinical drug design and screening methods deduce the effects of compounds based upon the biological products produced downstream in the process, such as amino acids and proteins. AFM is the only method of directly observing interactions of compounds with individual DNA molecules without stains and under natural conditions with simple sample preparation. X-ray crystallography, Nuclear Magnetic Resonance (NMR), absorption spectroscopy, gel electrophoresis, and Scanning Electron Microscopy (SEM) are some of the other

analytical techniques that have been used in attempts to investigate drug interactions with DNA and the resulting DNA conformations; each has distinct advantages and disadvantages.

X-ray crystallography records and analyzes the diffraction pattern of x-rays focused on a highly ordered crystal to determine the molecular structures of the substance that comprises the crystal. This method is highly sensitive to extremely small changes in structure and the position of atoms and molecules in relation to one another. It requires that the material can be highly concentrated into a nearly defect free, highly ordered crystal form. The molecular conformation in the crystal may be significantly different from the conformation in solution. The preparation of the pure crystal sample is challenging and requires hours, days, or weeks of effort. The information about bound compounds is gathered statistically from the numerous molecules in the sample, but is highly accurate.

Nuclear Magnetic Resonance (NMR) spectroscopy uses radiation to induce nuclear spin state changes which are unique for different atoms and their local environment. From the spectrum acquired on solid or liquid samples, the structure of molecules can be deduced. NMR can observe static as well as dynamic interactions between molecules. It requires that the sample be dissolved in a deuterated solvent and averages the results from all the molecules in the sample. The spectrum requires significant expertise to interpret and, depending on their complexity, may not be definitive.

Circular dichroism (CD) spectroscopy and UV-vis spectroscopy provide structural information on molecules based on their absorption of different wavelengths of light. CD spectroscopy measures the absorption of left and right handed circularly-polarized light which differentiates based on the molecules chirality and secondary structure. UV-vis spectroscopy uses the wavelengths of light in the spectrum ranges of 120 to 800 nm. DNA typically absorbs in the region of 160 to 300 nm due to the electronic transitions regions of the bases. These techniques are conducted in solution and are simple to conduct, but average the results across molecules in different states.

Gel electrophoresis separates molecules into bands relating to their characteristics (e.g. length, conformation, charge) which can be compared to standards to draw conclusions about the sample. It also is fairly quick and easy to conduct, but has the same disadvantages of averaging the results of numerous molecules in a sample instead of looking at interactions with an individual molecule and requiring interpretation of the interactions from indirect evidence.

Electron microscopy can directly image individual molecules; however, stains or contrast agents are required which reduce resolution. Electron microscopy is typically done under vacuum; molecular conformation *in vacuo* often differ from those found in natural environments.

Atomic Force Microscopy (AFM) can directly image individual molecules without stains in liquid, gaseous, or vacuum environments. It can measure the three-dimensional surface

profile, as opposed to just providing a two-dimensional image. The main disadvantages of AFM are its limited image size, inability to detect chemical bonds, and requirement that sample molecules are securely immobilized on a solid surface.

Optical tweezers force spectroscopy, a method related to AFM, has recently been employed to study the effect of drug binding on DNA lengthening and elasticity and related these properties to the mode of drug binding [44].

Binding Modes

Most drug binding to DNA does not involve covalent bond formation and, therefore, is an equilibrium process. The binding constant can be determined by measuring the free and bound forms of the drug. The thermodynamics are classically driven by electrostatic attractions, hydrophobic interactions, hydrogen bonding, and van de Waals forces [45].

There are two key modes of noncovalent drug interactions with the DNA helix—groove binding and intercalation (Figure 2.6), as well as combinations of these modes and non-specific binding. Polyamines, such as spermidine and spermine, are considered to be non-specific binders with primary interactions being electrostatic binding to the anionic phosphate backbone (Figure 2.7). Cyanine dyes are known to exhibit a combination of the binding modes [46].

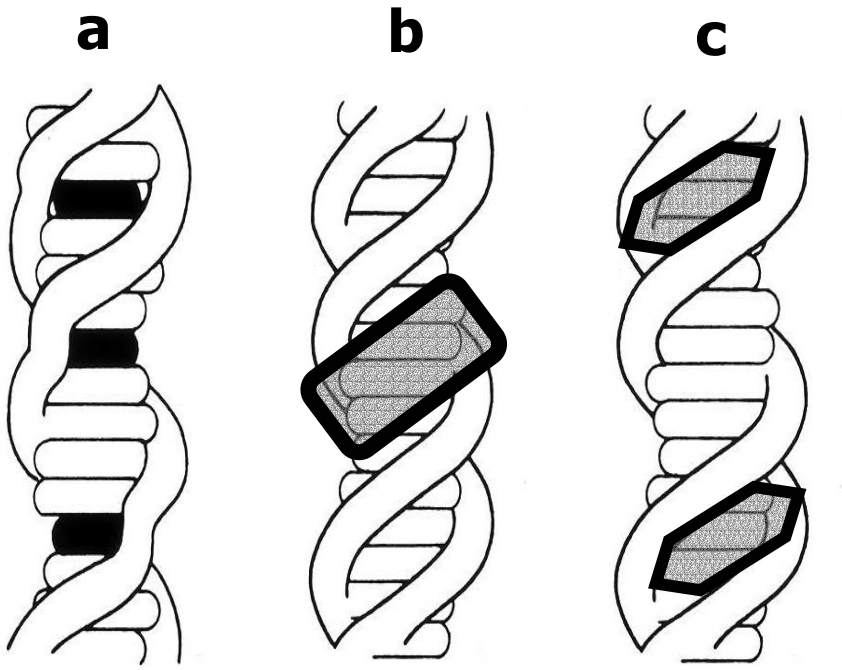

Figure 2.6 Models of drug and DNA interactions— a) intercalation, b) major groove binding, and c) minor groove binding

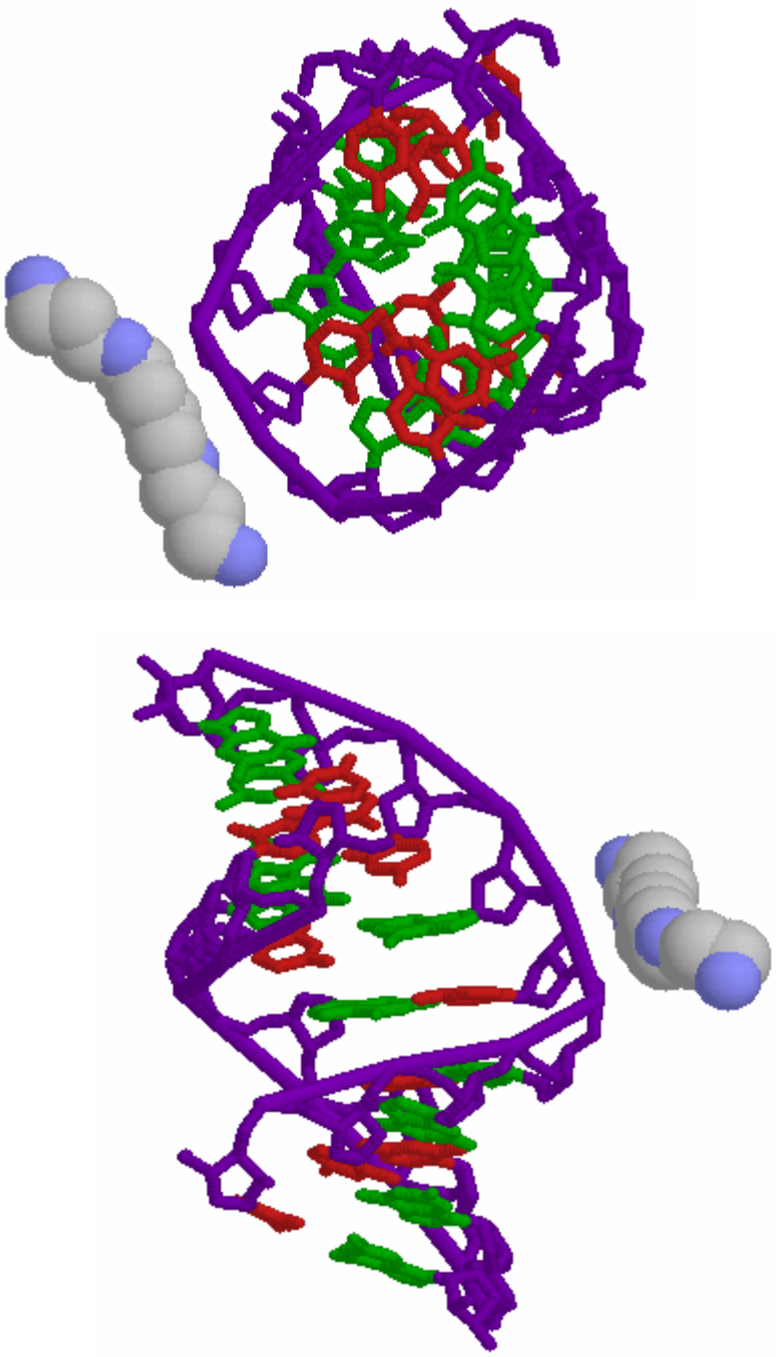

Figure 2.7 Structural models of spermine binding to the phosphate backbone of DNA at two different viewing angles based on X-ray diffraction at 1.9 Å resolution (pbd 100D) [39, 47]

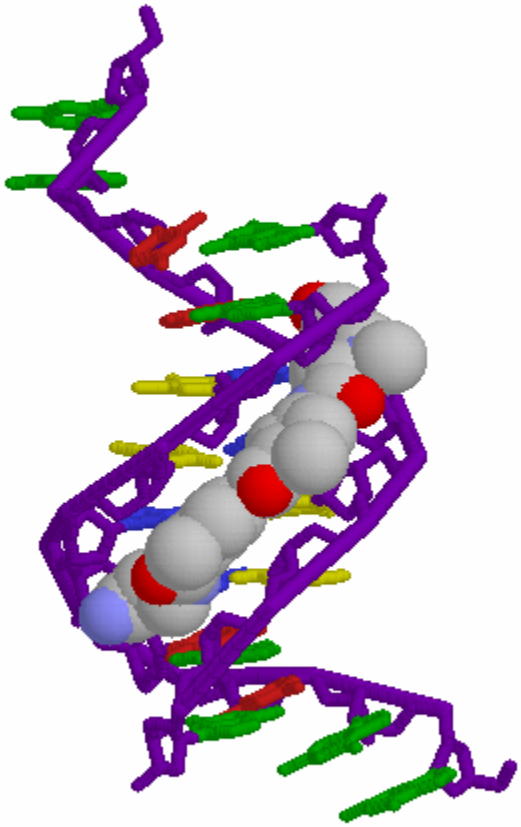

Figure 2.8 Structural model of dystamycin binding to the minor groove of DNA based on X-ray diffraction at 1.85 Å resolution (pdb 1JTL) [39, 48]

Groove Binders

Minor groove binding drugs are typically thin and crescent shaped to sterically fit into the narrow minor groove. Examples of minor groove binding ligands include distamycin, netropsin, Hoechst 33258, and chromomycin (Figure 2.8). They do not change the gross structure of DNA; however, x-ray crystallography has shown that netropsin caused small distortions in widening the groove and causing a slight bend in the double helix [49]. Studies have also detected that monovalent cations bind in the minor groove and produce bending [50].

There are fewer major groove binding drugs, although this is a very common binding mode for proteins to regulate gene expression. Examples of major groove binding drugs include cisplatin, alkylators, and mustards (Figure 2.9).

Intercalators

Intercalation occurs when a planar aromatic structure is inserted between the Watson-Crick basepairs which causes the DNA basepairs to separate and the overall strand to lengthen and slightly unwind. Compounds with two or three fused rings do not completely fill the space between the basepairs while four fused rings correspond in size to stack efficiently with the basepairs [51]. Intercalators generally have a preferential binding between 5' pyrimidine-purine 3' steps [52]. Examples of intercalators include ethidium, daunomycin, echinomycin, actinomycin, and quinacrine (Figure 2.10a). Intercalators are effective drugs based on interruption of DNA replication, transcription, and repair processes.

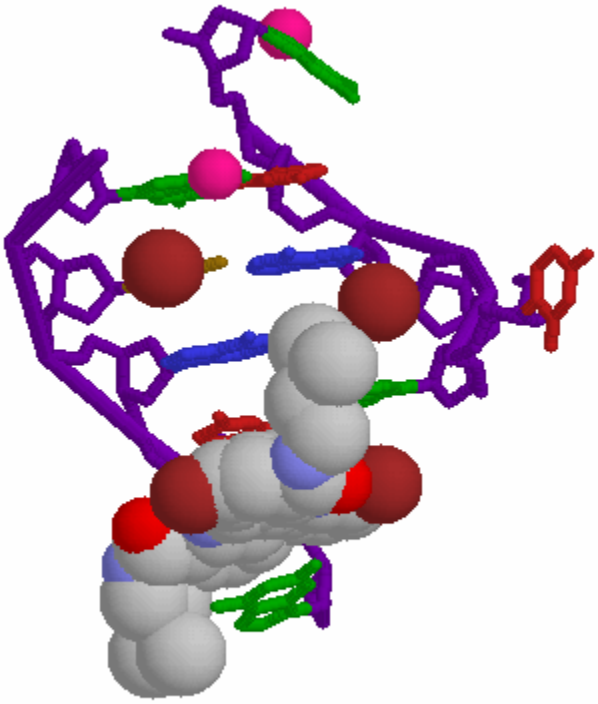

Figure 2.9 Structural model of phenazine binding to the major groove of DNA based on X-ray diffraction at 2.00 Å resolution (pdb 1EG6) [53]

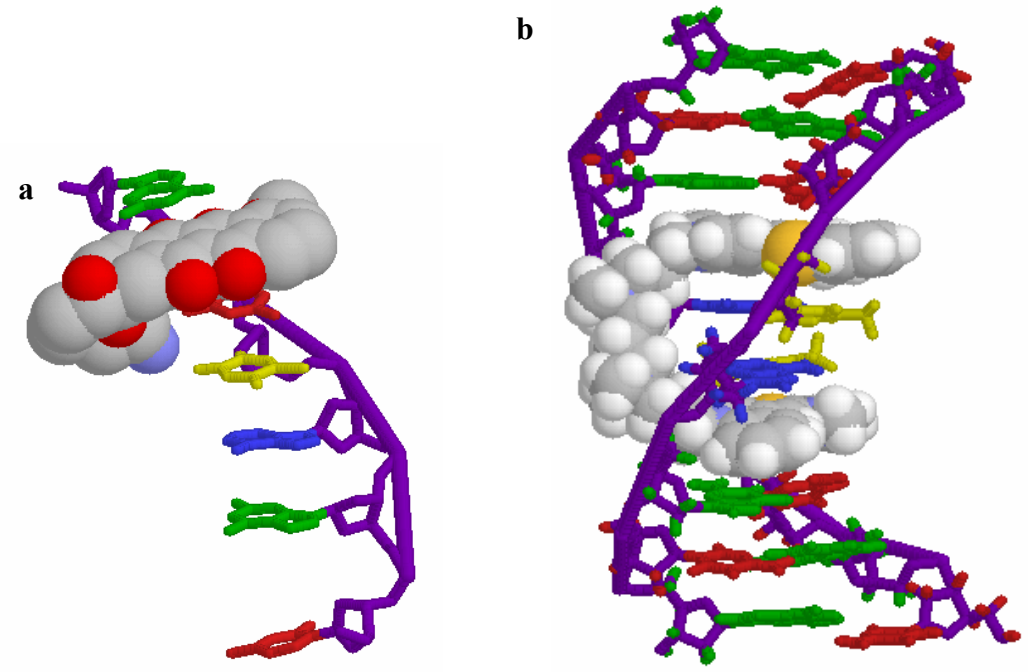

Figure 2.10 Structural models of DNA with a) daunomycin mono-intercalation based on X-ray diffraction at 1.50 Å resolution (pdb 1DA0) [39, 54] and, b) thiazole orange dimer bis-intercalation based on 40 NMR structures (pdb 108D) [39, 55]

Poly-intercalators are a class of intercalators in which multiple intercalating units are joined together with a linker compound. The chemical moieties, physical length, and rotational rigidity of linker compound have an important influence on the binding affinity and selectivity of the intercalator [52, 56]. It has been shown that regional charge densities impact the stacking stability and structure [57]. In addition, distortion of the DNA occurs with some bis-intercalators the degree of which is dependent on the linker structure [58]. Ditercalinium, thiazole orange dimer (TOTO), ethidum acridine, and flexi-di are examples of bis-intercalators (Figure 2.10b) that have been shown to cause twice the DNA helical extension and unwinding of a mono-intercalator.

Traditionally, the detection of intercalation has been based on a spectrophotometric shift which requires that the intercalating moieties are chromophores. Another indirect method of inferring intercalation has been based on the increase in DNA double helix stability resulting in decreased heat denaturation. DNA intercalation can be definitively determined based on strand lengthening which is best measured by AFM [59]. Gel electrophoresis and viscometry studies rely on DNA lengthening to deduce intercalation, but can be complicated by other factors. NMR images of ligands intercalated with DNA have been acquired which help establish the structural position of the ligand binding.

Clinical Applications

Drugs that interact with DNA have clinical significance especially for the treatment of solid tumors, lymphoma, and leukemia. The interruption of DNA replication is effective against rapidly reproducing cancer cells. More efficient and targeted DNA-binding drugs

Table 2.1 List of DNA-interactive drugs used clinically or in clinical research trials (key ref.: http://gucfm.georgetown.edu/welchjj/netscut/heme_onc/dnadruglist.html)

Drug Name	Chemical Name	Mode of Interaction
Actinomycin D		Intercalation
Adolzelesin, U-73,975	Cyclopropylpyrroloindole	Minor groove
Ametantrone	1,4-bis[(2-2((2-hydroxyethyl) amino)ethyl)amino-9,10-anthracenedione]	Intercalation
Amiloride, Midamor	3,5-diamino-6-chloro-N-(diaminomethylene) pyarazinecarboxamide	Intercalation
Bisantrene	9,10-anthracenedicarboxaldehyde bis[(4,5-dihydro-1H-imidazol-2y)hydrazone]	Intercalation
Bizelesin, U-77,779	Cyclopropylpyrroloindole	Minor groove
CC-1065, U-56314	Cyclopropylpyrrolo-indole	Minor groove
Chromomycin A3	Aureloic acid	Minor groove
CI-958, Parke-Davis	Benzo(chalcogeno)[4,3,2-cd]indazole	Intercalation
Daunomycin, Cerubidine		Intercalation, directed into minor groove
DAPI	4',6-diamidino-2-phenylindole dihydrochloride hydrate	Minor groove/ intercalation
DACA	N-[2-(dimethylamino)-ethyl]acridine-4-carboxamide	Intercalation
Distamycin A, Stallimycin	3-[1-methyl-4-[1-methyl-4-(formylamino)pyrrole-2-carboxamido]-propionamidine hydrochloride	Minor groove
Echinomycin		Bis-intercalation
Ethidium bromide	2,7-diamino-10-ethyl-9-phenylphenanthridinium bromide	Intercalation
Hedamycin		Intercalation, threading
Hoechst 33258	2(4-hydroxyphenyl)-5{5-(4-methylpiperzine-1-yl)-benzimidazol-2-yl]benzimidazole	Minor groove
mAMSA, amsacrine	(N-[4-(9-acridinylamino)-3-methoxyphenyl]methanesulphon anilide)	Intercalation, threading
Mitomycin C		Minor/Major groove
Netropsin, T-1384		Minor groove
Nogalamycin		Intercalation, threading
o-AMSA	4'-(9-acridinylamino)methanesulfon-o-anisidide	Intercalation
Tilorone	2,7-bis[2-(diethylamino)ethoxyl]-fluoren-9-one	Intercalation
Tomamycin	Pyrrolo-(1,4)-benzodiazepine	Minor groove

can be achieved by designing new compounds with multiple binding moieties that bind to specific DNA sequences.

Poly-Naphthalenetetracarboxylic Diimide

A unique series of poly-intercalators has been designed in Brent Iverson's lab at University of Texas, Austin based on aedamer stacking studies. The series is composed of 1,4,5,8-naphthalenetetracarboxylic diimide (NDI) aromatic groups linked by four amino acid segments (Figure 2.11) [60]. It includes bis-, tris-, and tetra-intercalators with enhanced binding affinities and was eventually extended to produce the first octakis-intercalator [61]. The NDI units were strung together in a head-to-tail fashion with variable linker polypeptide sequences. The synthesis of the molecules was accomplished using standard 9-fluorenylmethyoxycarbonyl (Fmoc)-based solid-phase methods. A 360-member library of different linker sequences was produced using combinatorial methods [62].

Like their aedamer predecessors, the poly-NDI molecules are initially stacked in solution. The stacking arrangement is identified by the upfield shift of the diimide hydrogen in NMR and the rate-limiting slow unstacking step of the association constant. However, the addition of 2% SDS releases the stacking conformation as revealed by the absorption spectrum maximum returning to that of the monomer measured by UV-vis spectroscopy [60].

Poly-NDI was designed to be a threading intercalator, although UV dissociation

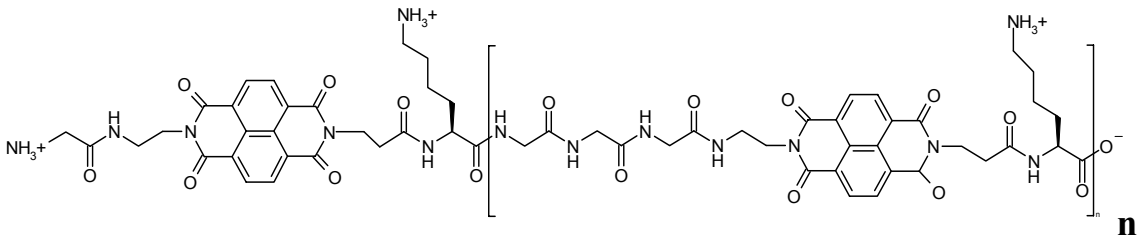

Figure 2.11 Structure of 1,4,5,8-Naphthalenetetracarboxylic diimide (NDI) with peptide linker where n = 1 for bis-NDI, n = 2 for tris-NDI, and n = 3 for tetra-NDI

measurements of some of these compounds are not consistent with this binding mode [63]. Threading involves one side chain of the intercalator being located in the major groove while the next side chain is located in the minor groove. This geometry requires that the intercalator "threads" through the DNA scaffold as shown in Figure 2.12. Other intercalators such as anthraquinone [64], poly-NDI derivatives [65], and the related bis-imide elinafide (LU-79553) [66] were previously demonstrated to exhibit this threading geometry. Advantages of the threading mode stem from its obstruction of both DNA grooves, improved sequence specificity, and slower dissociation rates. This would have implications for drug efficacy to interrupt translation and replication processes.

The specific linker structure of lysine and tri-glycine, has been investigated with UV-vis spectroscopy, viscometry, and DNAse footprinting to preliminarily determine that intercalation is the binding mode [60]. The compounds were found to have a high binding affinity for double stranded DNA, as well as general specificity for GC sequences.

Changing the linker sequences resulted in much stronger sequence specificities allowing NMR analysis to resolve DNA binding interactions (Figure 2.13) [67]. Interestingly, the reversal of the placement of the lysine after the tri-glycine, instead of before it, yielded one of the compounds with greater sequence specificity. In addition, the substitution of alanine for lysine resulted in the alteration of the linker binding in the minor versus major groove [63].

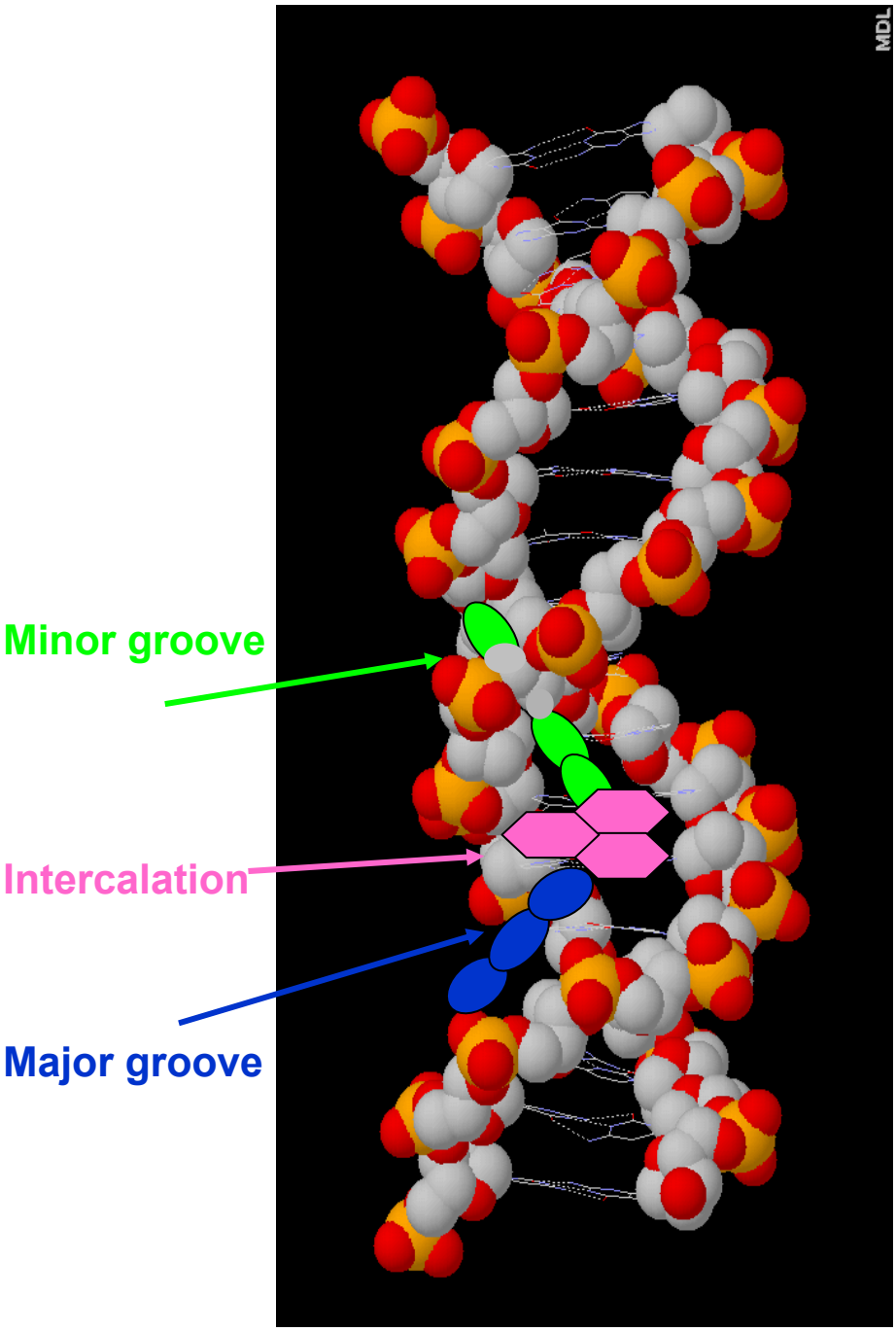

Figure 2.12 Schematic of threading intercalator with ring moiety (pink) inserted between basepairs and linker structures lying in the minor (green) and major (blue) grooves

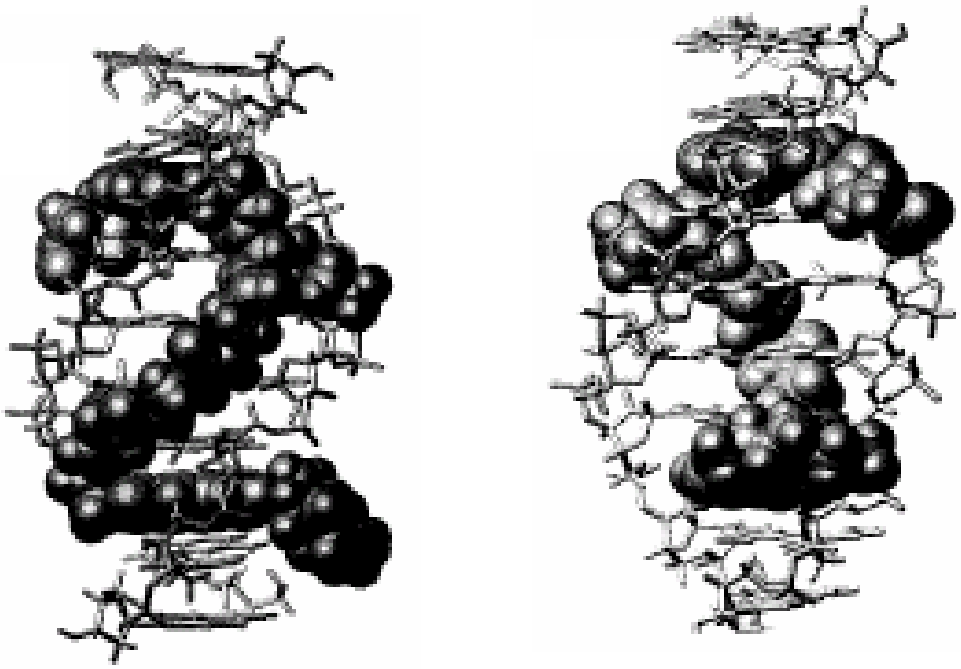

Figure 2.13 NMR structures of bis-NDI compounds with linker structures a) Alanine-Alanine-Alanine-Lysine in the minor groove, and b) Glycine-Glycine-Glycine-Lysine in the major groove [68]

Condensation

DNA condensation is defined as an increase in the volume compression ratio which results in the formation of highly-ordered structures. It is differentiated from aggregation or precipitation based on the order and finite size of the structures. Condensation occurs naturally where replication and transcription are not actively transpiring, such as virus capsids and sperm cells [69]. The mechanism of formation of the unique condensate morphologies (Figure 2.14) of toroids (doughnut-like structures), spheres, and rods has been the focus of much research during the past 30 years, yet it remains elusive.

It is postulated that condensation occurs when 90% of the DNA negative charge from the phosphate backbone is neutralized [70]. This electrostatic effect has not been found to be sufficient to completely account for the condensation forces. Kinetic and thermodynamic based models with electrostatic and hydrostatic mechanisms have been proposed [71]. Polymer physicists have used a "bead-spring" model of semiflexible polyelectrolytes [72] to study this phenomena as a "coil-globule" transition [73, 74], although DNA does not truly behave as a random coil to fit the model.

While *in vivo* condensation is directed by proteins (such as histones), identical structures are formed *in vitro* by a variety of compounds including multivalent cations ($Co(NH_3)_6^{+3}$, spermidine, and polylysine), ethanol, and PEG. There are obvious energetic barriers against the compaction of the DNA molecule to overcome entropy and electrostatic repulsions and significant energy is expended by organisms which is estimated to be approximately one ATP hydrolyzation per two basepairs packaged [75]. It is surprising

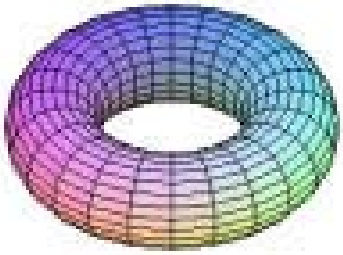

Toroid

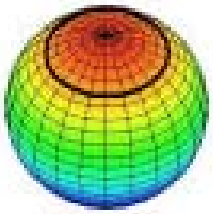

Sphere

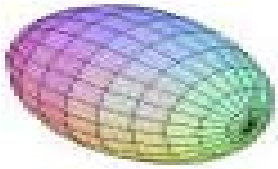

Rod

Figure 2.14 Classical DNA condensate morphologies of toroid, sphere, and rod

that condensation occurs spontaneously *in vitro* under fairly broad conditions with the above listed condensing agents.

Currently, there is much interest in the application of condensation for delivery of DNA in gene therapy to afford protection from nucleases and other enzymes during cellular entry [76]. The folding of DNA during condensation bears some similarities to protein folding which is also of strong interest with numerous applications.

CHAPTER 3

AFM ANALYSIS OF DNA LENGTHENING

Background

As discussed in Chapter 1, Atomic Force Microscopy (AFM) is well suited for the analysis of DNA and drug interactions. AFM is non-destructive and does not require stains or coatings that are potentially obstructive or interfere with the interactions under observation. AFM has the high resolution necessary for detailed analysis of individual DNA molecules. AFM studies with densely packed DNA on a lipid layer under water [77] or with extremely sharp tip under propanol [78] have resolved the helical periodicity of double stranded DNA. More typically, the resolution is about 10 nanometers primarily due to the tip radius of curvature [79]. Humidity has also been shown to affect the apparent width of DNA molecules observed with AFM [80].

As discussed in Chapter 2, the intercalation of DNA results in its lengthening. Coury et al established the use of AFM as an accepted assay for intercalation based on its measurement of DNA contour lengthening which serves as direct evidence for this mode of drug interaction [81]. Bis-intercalation has also been determined using AFM in work with thiazole orange dimer by Jeff Petty's lab [46, 82]. The studies reported herein set out to examine the mode of DNA interaction of a unique series of poly-intercalators using AFM.

Most AFM studies of DNA and intercalator binding have shown lengthening of the DNA strands without noticeable changes in secondary structure [24, 30]. Recently, Berge, *et al.* [82, 83] have observed complex structural changes in DNA with the bis-intercalators ditercalinium and luzopeptin which were attributed to intermolecular crosslinking. Similar DNA structures and complete condensates have been observed by AFM with increasing concentrations of spermidine and polylysine which are known condensing agents [84-86].

AFM Technique

The research reported herein was performed using a Nanoscope IIIa AFM controller with a Multi-Mode base (Veeco, Santa Barbara, CA). The instrument was mounted on a vibration isolation table to reduce environmental noise. TappingMode™ intermittent contact mode imaging was utilized. This mode has become more popular than contact mode because of its lesser force exerted on the soft biomolecules [87]. A Veeco J scanner (125 μm x 125 μm scan size, 5.0 μm vertical range) was used which allowed larger areas of the sample to be examined, while still permitting highly detailed imaging of small features. The scanner was calibrated in the x, y, and z directions using a NIST certified grating (Figure 3.1).

Rectangular silicon cantilevers (MikroMasch Model NSC12 B; Tallinn, Estonia) with approximate dimensions of w = 35 μm, l = 90 μm, and t = 2 μm were used. The spring constant (k), calculated according to the equation given in Chapter 1, is approximately 14 N/m. The cantilevers were ozone cleaned (Jelight Inc., Laguna Hills, CA) prior to each

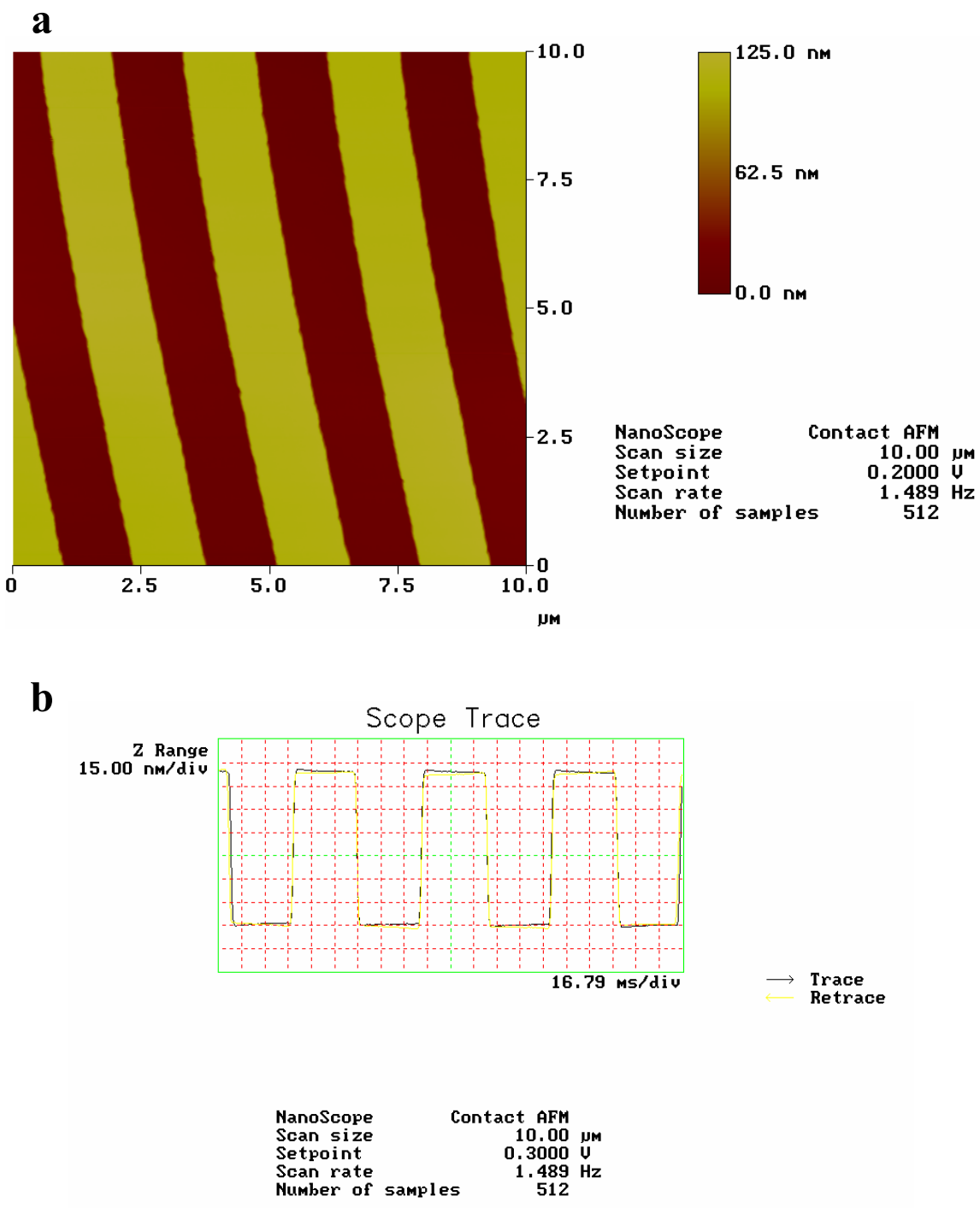

Figure 3.1 NIST certified silicon grating (MikroMasch TGZ02) used for the calibration of the Nanoscope IIIa with J scanner a) AFM topographic image with accurate x and y measurements of 3.0 µm, and b) scope trace with accurate z height measurement of 104.5 nm

imaging session or whenever the tip became contaminated as was detected by a double or multiple trace image (Figure 1.4). The cantilever was tuned to its resonance frequency which was between 250 and 400 kHz and used at the minimum drive amplitude between 10 and 150 mV in order to reduce the pressure exerted by the tip on the molecules during imaging.

All studies were conducted under ambient conditions (20% to 50% humidity, 22º to 23º C). This simplified the experimental set up and accelerated the rate of research. A few experiments were conducted with controlled humidity (22% r.h.), but no noticeable differences in the images were discerned.

Scan sizes ranged from 5 μm to 400 nm at a scan rate of 1.5 Hz and 512 x 512 pixels. This scan speed was preferred to produce better images with higher confidence in length measurements and is commonly recommended for this scan size range [88]. Faster scan speeds may be acceptable for length measurements of long DNA molecules given the already large standard deviations. Significant efforts are aimed at increasing scan speed while maintaining resolution using smaller cantilevers or integrated piezoelectric actuators [89].

AFM data were processed using the Nanoscope software (version 4.22, 5/29/96). Images were flattened using the appropriate order to remove background sloping. The contour lengths of DNA molecules were determined by manually tracing the strands using the top view mode of the software (a tedious and time-consuming process). Several attempts

have been made to computerize these measurements [90]. Contour lengths were also measured using software developed by Dr. Jeff Petty's lab (Furman University) run in Igor Pro (WaveMetrics, Inc., Lake Oswego, OR). Length measurements by both methods were found to be approximately equivalent, however concerns about pixel averaging led to a preference for the Nanoscope software method.

Sample Preparation

DNA Plasmid

All experiments reported herein used plasmid pRS316 DNA (4,887 base pairs) provided by Dr. Nick Hud's lab (Georgia Institute of Technology). This plasmid was selected based on its length, sequence, and selection of restriction enzyme excision sites. It included an ampicillin resistant gene which was useful in expression. The sequence had a 1:1.2 ratio of GC:AT bases and several significant AT tracts were present (see Appendix A for complete sequence).

The plasmid had been maintained in *E. coli* DH5a bacteria in cryogenic storage in a 50% glycerol solution to protect them during freeze/thaw cycles. A small portion of the culture was thawed and plated using aseptic procedures. The bacteria were streaked onto a Petri dish containing a solid Luria-Bertani base and 100 μg/mL ampicillin (LB+amp) in agar. The plate was inverted and incubated at 37º C for 15 hours. In order to reduce colony growth, the Petri dish was sealed with Parafilm and stored in an inverted position in the refrigerator for several hours. A fresh culture was started by inoculating a single colony into 2 mL of LB+amp liquid growth media in a round bottom tube with an air flow cap to

provide maximum air exposure for aerobic bacterial growth. The tube was incubated at 37º C for 5 hours in a shaker at 225 rpm. A large, fast-growing culture was then started by inoculating 1 mL of the smaller culture into 250 mL of LB+amp broth in a flask and incubating in a similar manner overnight. The plasmid was separated from the bacteria and purified using a Quiagen maxi prep kit (Quiagen Sciences, Germantown, MD) following the high-copy instructions provided by the manufacturer.

The plasmid was linearized using *Sca I* restriction endonuclease enzyme (Promega, Madison, WI) to produce a blunt cut at a single site. The buffer K provided by Promega which was optimized for *Sca I* activity was diluted from 10x to 1x. This pH 7.4 buffer contained 10 mM Tris-HCl, 10 mM $MgCl_2$, and 150 mM KCl. The concentration of the plasmid was estimated based on UV-vis spectroscopy with small volume glass cuvettes (Fisher Scientific) and a Shimadzu UV-1601 spectrophotometer. Approximately 10 µg of plasmid and 2 µL of the *Sca I* were added to 28 µL of buffer K. This solution was mixed gently and incubated in a water bath at 37º C (enzyme optimal temperature) for 17 hours, then stored in the refrigerator for a few hours.

Single cut linearization was confirmed with an agarose gel. A horizontal gel was prepared with 0.7% molecular biology grade agarose (International Biotechnologies, Inc, New Haven, CT) in Tris Borate EDTA (TBE) buffer containing 0.01% ethidium bromide to provide a fluorescent marker. The gel was run using a Kodak BioMax OS710 electrophoresis apparatus filled with TBE buffer set at 160 volts for 30 minutes until the

loading dye bands approached the end of the gel. The gel was placed on a UV lamp table to view the fluorescence of the ethidium bromide tagged DNA bands (Figure 3.2).

Final purification of the plasmid was achieved using a Microcon 30 centrifugal filter (Millipore Corp., Billerica, MA). The remaining plasmid solution was mixed with autoclaved, deionized Milli-Q water to a total of 500 μL and filtered through the Microcon 30 filter during centrifugation at 11,000 rpm (~9,880 g force) for 12 minutes in an Eppendorf Microcentrifuge 5415C (Brinkmann Instruments Inc., Westbury, NY). The fluid was decanted from the bottom of the vial and a fresh aliquot of water was centrifuged through the same filter a total of five times to thoroughly rinse the plasmid. Then 100 μL of water was pipetted into the top of the filter which was inverted on top of a new vial and centrifuged at 3,500 rpm (~1000 g force) for 3 minutes. The fluid was returned to the top of the filter and centrifuged a second time to ensure complete removal of the purified plasmid.

A stock concentration of 70 μg/mL DNA in filtered (0.2 μm pore, Nalgene, Rochester, NY), deionized water (>18 MΩ cm-1, Barnstead E-Pure, Dubuque, IA) was determined based on UV-vis spectroscopy absorption at 260 nm (Figure 3.3). Aliquots of the DNA were stored in a bio-freezer (-40º C) and thawed to room temperature for use. Dilutions were made to achieve final sample concentrations of 1 μg/mL pRS316 DNA. This concentration was selected systematically to deliver sample coverage that was not too dense causing molecules to cover one another or too dilute making it difficult to find molecules within the scan size.

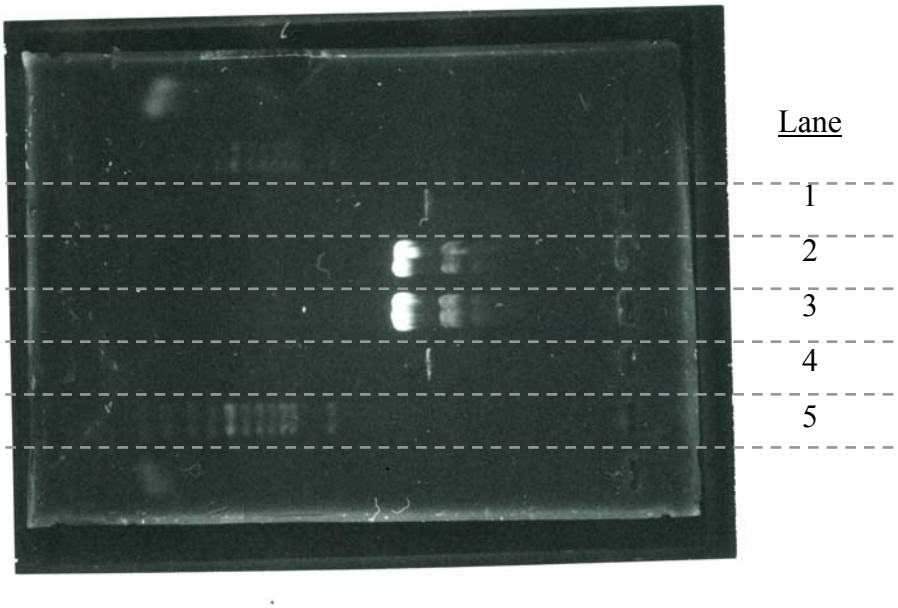

Figure 3.2 Horizontal gel electrophoresis UV fluorescence of ethidium bromide-tagged DNA. Lanes 2 and 3 contain the original, purified circular plasmid with two bands representing the open and supercoiled forms, lanes 1 and 4 contain the linearized plasmid verified by the single band, lane 6 contains a 1,000 kb DNA ladder (Promega G:694A) as a length indicator

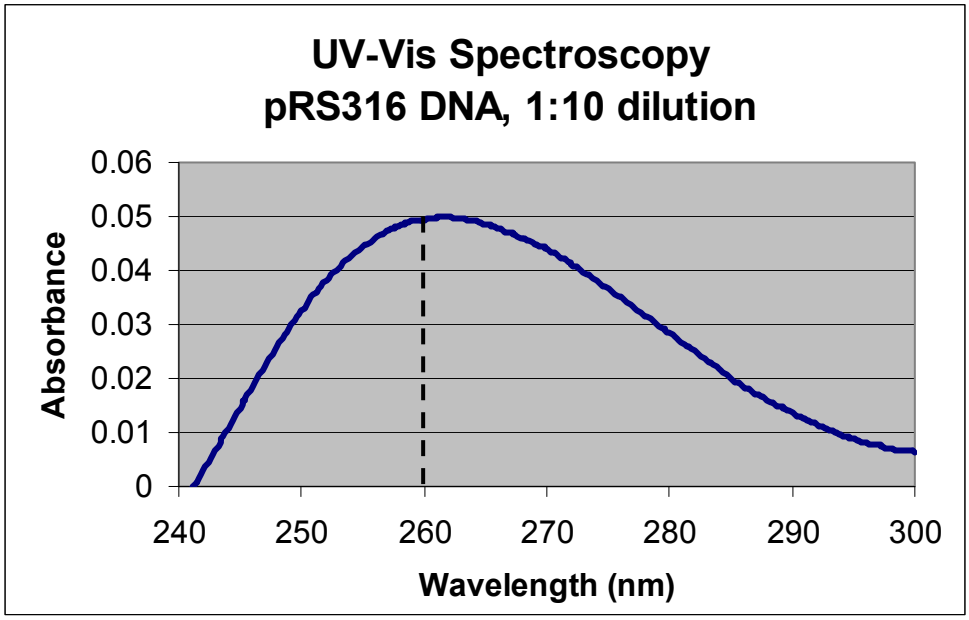

Figure 3.3 UV-vis spectroscopy absorption curve used to determine DNA concentration based on the Beer-Lambert Law

Poly-intercalator

Bis-, tris- and tetra-1,4,5,8-naphthalenetetracarboxylic diimide (NDI) (Figure 3.4) samples were provided by Dr. Brent Iverson's lab (University of Texas at Austin). They had been stored as solids in a bio-freezer for several years. The drugs were yellow powders that dissolved fairly easily into filtered, deionized water. Concentrations were determined using the Beer-Lambert law based on UV-vis spectroscopy absorption measurements and extinction coefficients previously published [60] (Table 3.1). Dilutions were made and stock solutions were stored in a bio-freezer and brought to room temperature and centrifuged before use.

Buffer

A 100 mM magnesium chloride and ammonium acetate buffer stock solution was adjusted to pH 8.0 using sodium hydroxide. All salts were obtained from Fisher Scientific (Hampton, NH) and used as received. The stock solution was stored in a laboratory refrigerator. It was brought to room temperature and filtered through a 0.2 μm pore filter before dilution to a final sample concentration of 10 mM. The Mg^{+2} in the buffer facilitates electrostatic binding of the negatively-charged DNA onto the positively charged mica surface. Other divalent metal cations, such as Ni^{+2} have been shown to efficiently support DNA binding onto mica [91]. Previous studies have established that the DNA is weakly bound to the mica under these conditions and can rearrange on the surface[92].

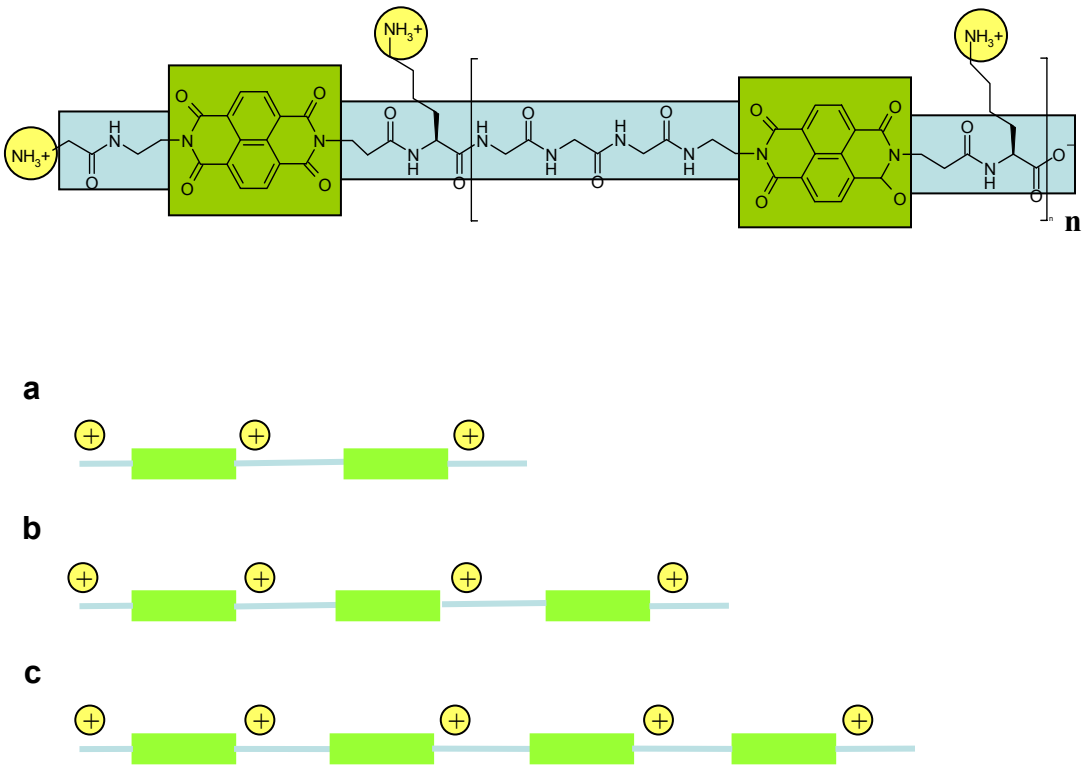

Figure 3.4 Structure and cartoon representation of 1,4,5,8-Naphthalenetetracarboxylic diimide (NDI) with peptide linker where a) n =1 for bis-NDI, b) n=2 for tris-NDI, and c) n=3 for tetra-NDI

Table 3.1 Extinction coefficients of poly-NDI at 386 nm where ε^1 was measured in 10 mM TRIS buffer with 1mM EDTA and 50 mM NaCl and ε^2 was measured in 2% SDS

Compound	ε^1	ε^2
Mono-NDI	20,000	23,400
Bis-NDI	27,000	44,000
Tris-NDI	39,200	74,600
Tetra-NDI	51,300	96,000

Another approach to DNA immobilization on mica is to use 3-aminopropyletriethoxy silane (APTES) [93]. This method was briefly undertaken, but was found to be inferior due to its less uniform background surface deposition (Figure 3.5). Numerous other DNA immobilization techniques are dependent upon covalent bonding using chemical reactions with compounds such as thiols [94]. Concerns about interference with the drug binding under observation are greater under these conditions.

Surface Immobilization

Sample solutions were prepared in plastic microcentrifuge tubes with the following order of addition: filtered, deionized water, magnesium chloride/ammonium sulfate buffer, pRS316 DNA, and poly-NDI. Solutions were mixed using an Eppendorf micropipette and allowed to incubate at room conditions for thirty minutes to an hour to assure sufficient time for complete drug/DNA interactions to take place. Solutions were mixed using the pipette periodically throughout the incubation. Longer incubation times were used for the larger NDI molecules to provide extra time for interactions, especially based on the proposed threading mechanism.

Half inch diameter disks of muscovite green mica (New York Mica Company, New York, NY) were freshly cleaved using transparent tape to peel off the top mica planes. Mica is a naturally occurring layered structure that easily forms atomically uniform planes. The surface is hydrophilic immediately after cleavage; however it can quickly become contaminated in the air and become hydrophobic. Therefore, all solutions were applied to the mica within five minutes after cleavage.

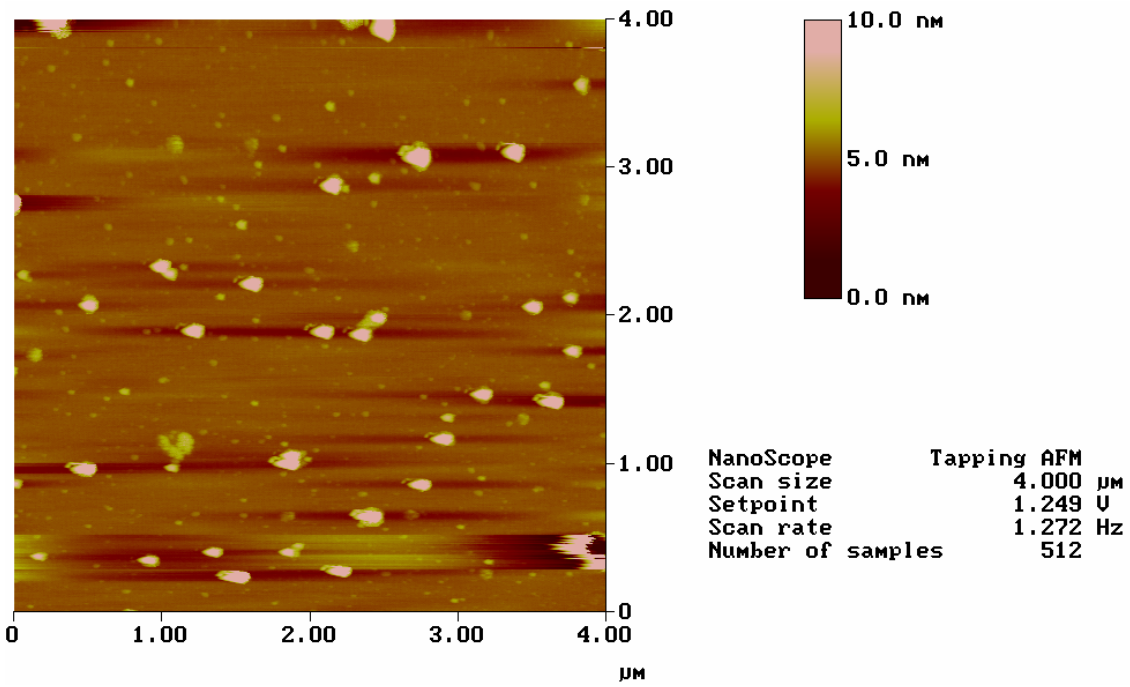

Figure 3.5 AFM topographical image of mica with 3-aminopropyltriethoxy silane (APTES) coating demonstrating uneven areas of deposition

Ten microliters of sample solution was pipetted into the center of the mica disk and allowed to incubate inside a humidity chamber for thirty minutes. The humidity chamber was constructed of a closed glass Petri dish with droplets of deionized water around the inside perimeter. The mica disks were placed on a Parafilm sheet in the center of the dish. This chamber was prepared at least 10 minutes prior to use to allow the humidity level to stabilize. The increased humidity helped reduce the rate of evaporation of the DNA solution on the mica to allow it to attach to the surface electrostatically, as opposed to being deposited during drying. A brief study was undertaken to confirm that both the initial DNA/drug incubation in solution and the application incubation on the mica were sufficient and did not change with increased time periods.

Excess solution was wicked off the mica by touching the edge against a Kimwipe® wipe (Kimberly-Clark Corp., Dallas, TX). The sample was rinsed in 20 mL filtered, deionized water by dipping it perpendicular to the liquid surface three times. Previous studies also included an ethanol rinse to accelerate drying [95], however problems with ethanol contamination and concerns about converting some DNA from B form to A form resulted in the elimination of this step. The sample was thoroughly dried using a stream of nitrogen (~20 psi) at an approximately 60º angle to the sample surface. This process qualitatively seemed to improve the straightening of the DNA strands on the surface without putting them under too much stress.

The use of centrifugal force to straighten the DNA molecules on the surface to facilitate length measurements was also explored. Yokota *et al*. [96] reported spin-stretching of

DNA by spinning at 4000 to 7000 rpm. This high force could result in elongation of the strands thus interfering with the detection of intercalation induced lengthening. A lower force was attempted by mounting the mica disk on a metal shim and attaching it to the center of a mini-centrifuge (VWR Scientific, Model V). Limited success was achieved in consistently applying the DNA and fear of potential damage to the centrifuge led to discontinuation of this approach.

The mica was firmly attached to a 15 mm diameter metal shim (Ted Pella, Inc., Redding, CA) using an adhesive tab (Ted Pella). The metal shim served to mount the sample on the magnetic holder of the AFM piezo stack. It was critical to assure that the mica was well adhered to the surface to prevent movement of the sample during tapping mode imaging.

Samples were stored inside a dessicator at room temperature to reduce hydration of the surface which could interfere with clear imaging of the DNA. However, complete dehydration of the DNA was not desired in order to maintain the natural B form.

DNA Lengthening

Theoretical Model

The DNA lengthening assay can be fit to a theoretical model based on the McGee-von Hippel equation [97] which represents the binding affinity (K_a) as the quotient of the concentration of occupied intercalation sites and the concentration of unoccupied intercalation sites multiplied by the concentration of free drug:

Equation 3.1

$$K_a = \frac{\left(\frac{L - Lo}{a}\right)D}{\left(\left(\frac{DB}{n}\right) - \left(\frac{L - Lo}{a}\right)D\right)\left(Io - \left(\frac{L - Lo}{a}\right)D\right)}$$

where Lo and L are the lengths of un-intercalated and intercalated DNA, D is the total DNA concentration, B is the number of basepairs per DNA, a is the lengthening per intercalation event, n is the exclusion number, and I is the total intercalator concentration [98]. This equation can also be solved for L to more easily be used in modeling (See Appendix B for derivation):

Equation 3.2

$$L = \frac{\left(\frac{2Lo}{a} + \frac{1}{KD} + \frac{B}{n} + \frac{I}{D}\right) \pm \sqrt{\left(\frac{2Lo}{a} + \frac{1}{KD} + \frac{B}{n} + \frac{I}{D}\right)^2 - 4\left(\frac{1}{a}\right)\left(\frac{Lo^2}{a} + \frac{Lo}{KD} + \frac{BLo}{n} + \frac{ILo}{D} + \frac{BIa}{nD}\right)}}{2\frac{1}{a}}$$

The nearest neighbor exclusion number is based on the observed inability of ligands to intercalate between every basepair at saturation concentrations [99]. This limitation has been hypothesized to be due to steric hindrances [100]. In addition, with linked poly-intercalators the rigidity and binding of the linker to the DNA may limit the availability of some sites. Iverson's previous work with this series of NDI predicted a nearest neighbor exclusion number of 2 representing intercalation in between every other basepair [60]. A nearest neighbor exclusion number of 2 was also found for the related bisnaphthalimide LU-79553 based on NMR structural determination [66] (Figure 3.6). Additional research by Iverson's group using an NDI series with a slightly different linker sequence of the same four amino acids showed a nearest neighbor exclusion number of 4 [67] (Figure 3.7).

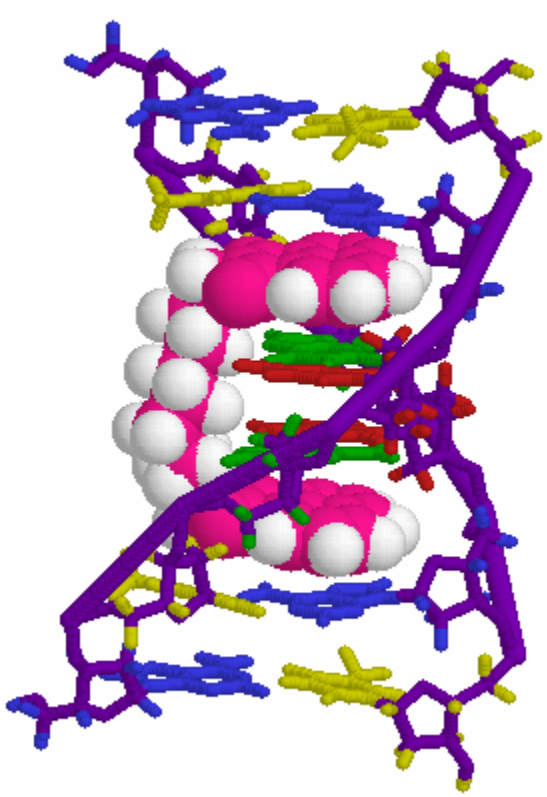

Figure 3.6 Structural model of bisnaphthalimide LU-79553 with double-stranded oligonucleotide based on 15 NMR structures (pdb 1CX3) [39, 66]

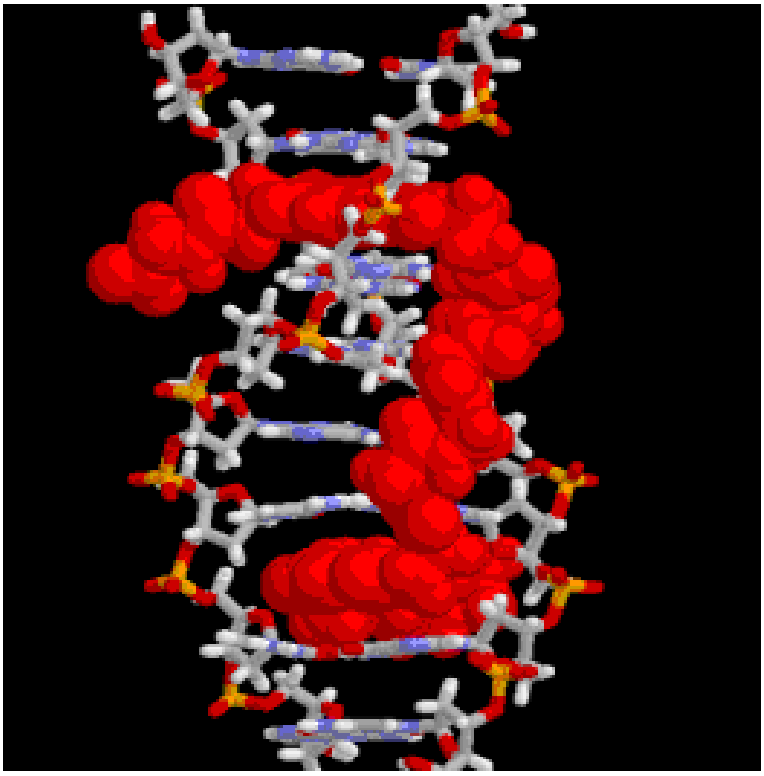

Source: www.cm.utexas.edu/Iverson/dnapolyi.htm

Figure 3.7 NMR structure of related NDI compound (Gly-Gly-Gly-Lys) linker with a space of one open potential binding site between intercalating rings

Lengthening of the DNA molecule due to intercalation by a planar ring structure has generally been assumed to be equal to approximately its van der Waals thickness of 0.34 nm [101]. This is also the distance between basepairs in B form DNA [37].

Using the theoretical lengthening equation and assuming a nearest neighbor exclusion number of 2 and 0.34 nm lengthening per intercalation event, the expected lengthening of pRS316 versus bis-NDI concentration has been calculated (Figure 3.8).

Contour Length Measurements

The contour length of a DNA plasmid pBluescript II' (provided by Nick Hud's lab at the Georgia Institute of Technology) was measured for over one hundred strands and found to be 1155 $\pm$ 85 nm (Figure 3.9). This agrees extremely well with the theoretical length of 1163 nm for B-form DNA with 3421 basepairs. The pRS316 DNA was measured as a control for each set of NDI data and found to be 1660 $\pm$ 118 nm. This also agrees extremely well with the theoretical length of 1662 nm for B-form DNA with 4887 basepairs. A histogram of the strand length measurements is shown in Figure 3.10. The longer pRS316 DNA plasmid was chosen for future experiments. The balance of lower theoretical error with the difficulties finding well laid out strands for longer molecules needs to be considered.

A study of variances between researchers conducting the length measurements was less than 3%. Repeated measurements of the same strand yielded a variation between 0.5 and 5%, primarily dependent upon the quality of the image.

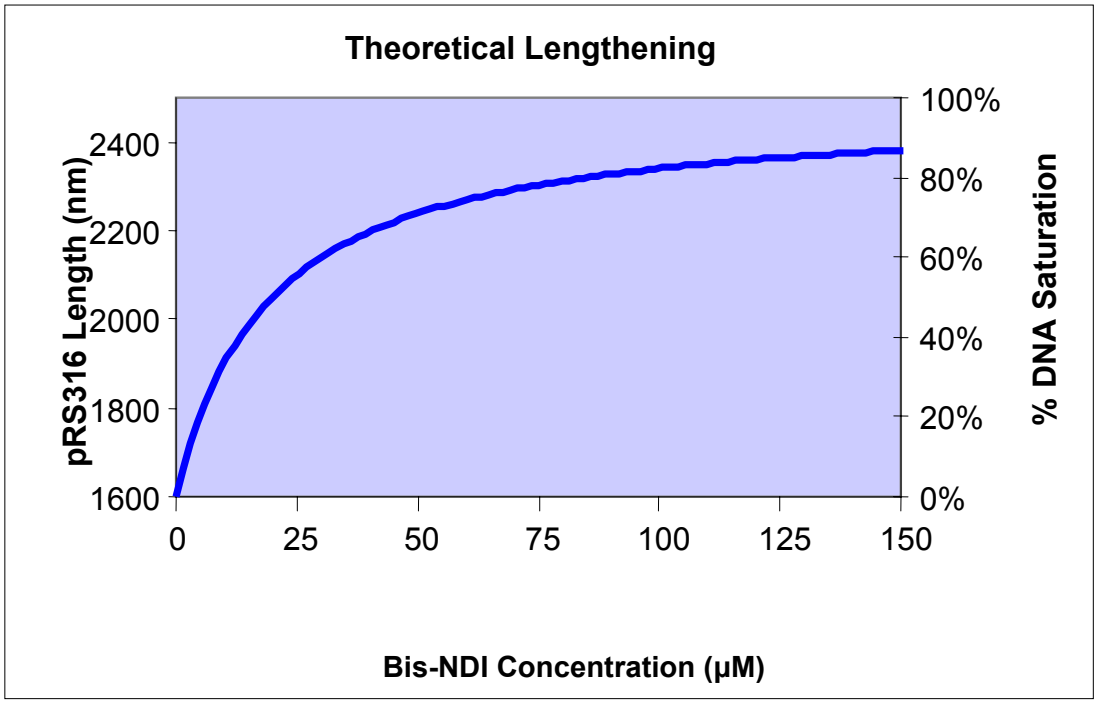

Figure 3.8 Theoretical lengthening of pRS316 assuming a nearest neighbor exclusion number (n) of 2, lengthening per intercalation (a) of 0.34 nm, and a binding affinity (Ka) of 4.0×10^4 with plateau approaching maximum length limit.

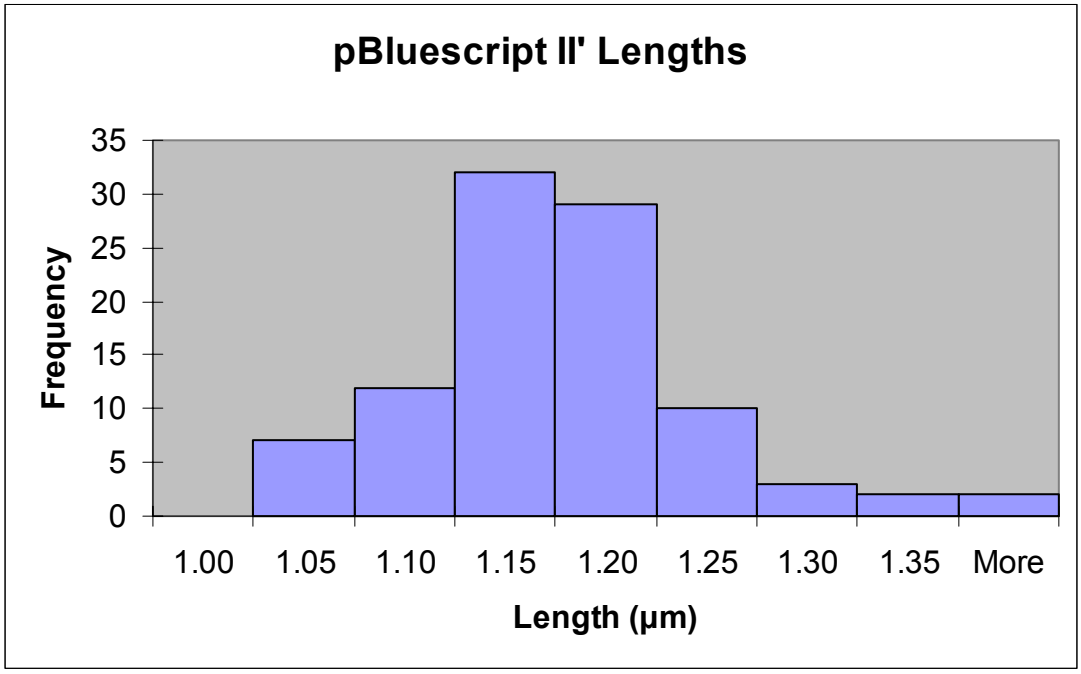

Figure 3.9 Histogram of measured lengths of pBluescript II' based on AFM images which correlate well with theoretical B-form length of 1.16 µm versus A-form length of 0.89 µm

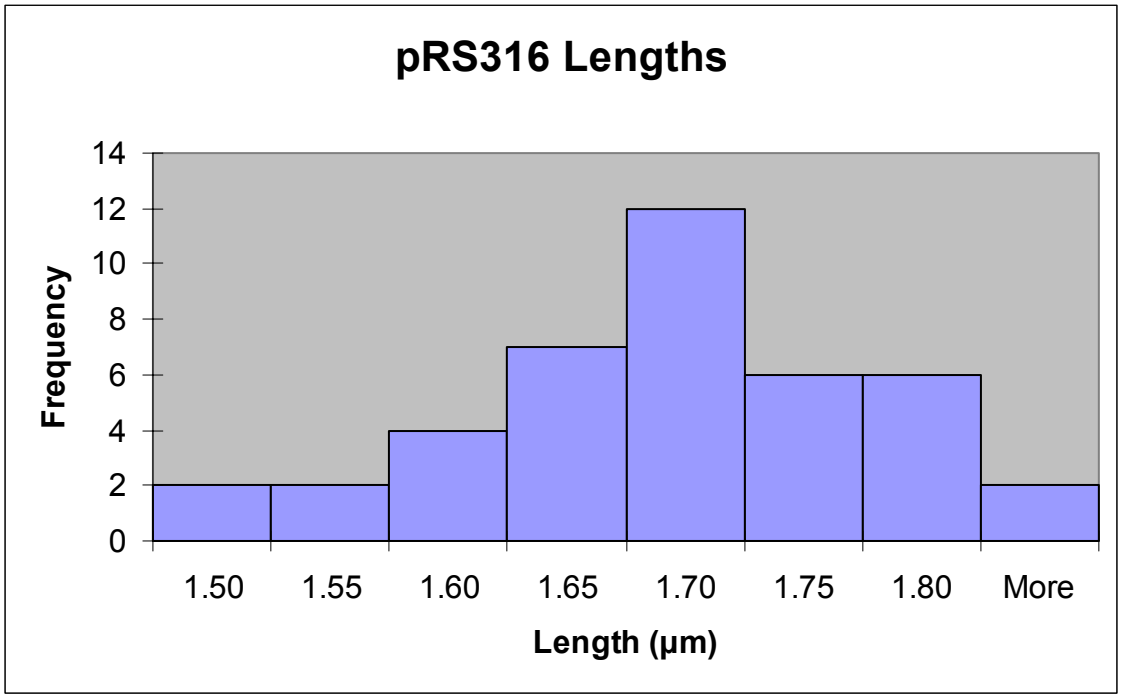

Figure 3.10 Histogram of measured lengths of pRS316 based on AFM images which correlate well with theoretical B-form length of 1.66 µm versus A-form length of 1.27 µm

Bis-Naphthalenetetracarboxylic Diimide

Bis-NDI Lengthening

Concentrations of bis-NDI were selected based on preparatory studies using the mono-intercalator ethidium bromide which confirmed the ability to observe DNA lengthening using these experimental procedures. Bis-NDI concentrations of 10 μM, 25 μM, 36 μM, 50 μM, 100 μM and 150 μM were prepared with a constant pRS316 concentration of 1 μg/mL. The ratios of drug molecules to DNA basepair related to each of these concentrations are listed in Table 3.2.

The average contour length increased with bis-NDI concentration (Table 3.2) confirming intercalation. Similar findings based on UV-vis spectroscopy, viscometry, and DNAse footprinting have been reported [60]. Histograms of the length data indicate that although there were significant standard deviations, the lengths formed a reasonable distribution curve (Figure 3.11). The data also reveals that the strands retained the B-form and did not form a mixture with A-form DNA.

It should be noted that the DNA length actually decreased at a low concentration of 5 μM with a length of 1455 $\pm$ 226. This is still greater than the expected length of A-form DNA (1271 nm). This apparent shrinkage of the DNA could be the result of kinking and bending of the DNA upon drug binding. DNA distortions have previously been described and attributed to cation binding [50, 101].

Table 3.2 Concentration-dependent lengthening of pRS316 plasmid with bis-NDI. Lengths at higher concentrations were Not Determined (ND) due to secondary structure formation

Bis-NDI Concentration (μM)	**Bis-NDI Compound : pRS316 Basepair Ratio**	**Average Strand Length (nm)**	**Standard Deviation (nm)**
0	0	1660	118
5	4 : 1	1455	226
10	9 : 1	1893	177
25	23 : 1	2114	333
36	33 : 1	2150	99
50	47 : 1	2193	417
100	94 : 1	ND	ND
150	141 : 1	ND	ND

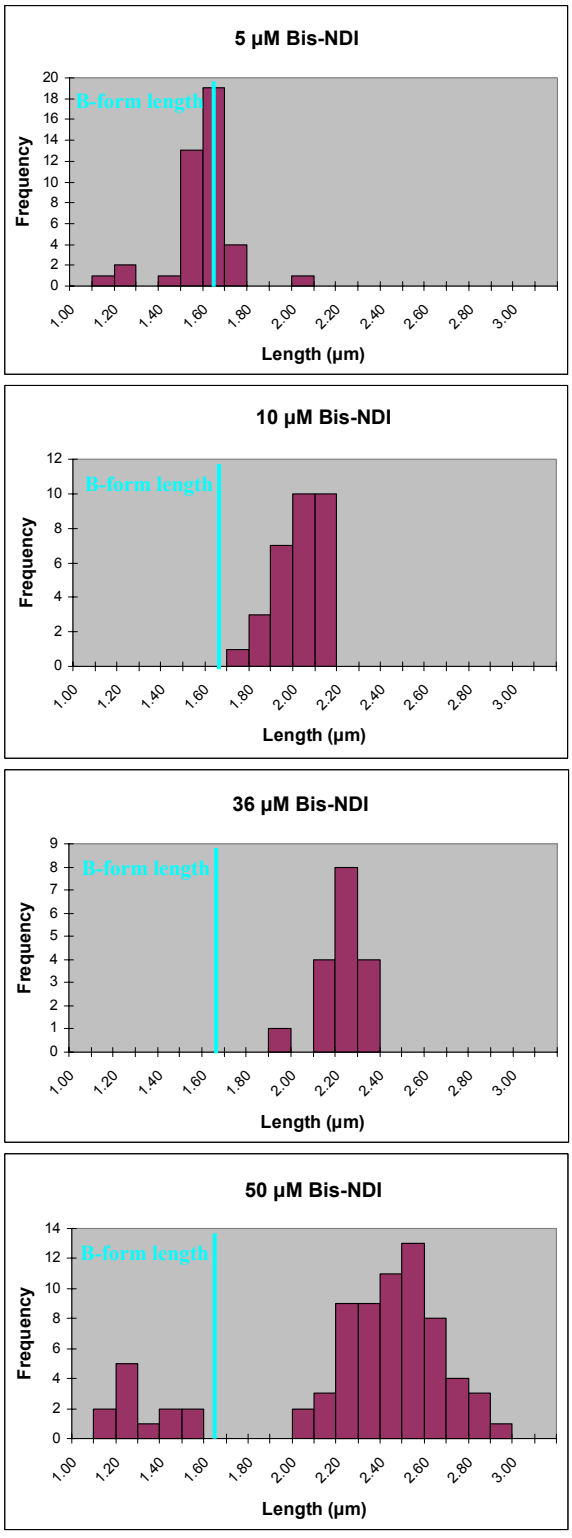

Figure 3.11 Histograms of pRS316 length progressing with increasing bis-NDI concentration affirming retention of B-form conformation and lengthening due to intercalation

DNA lengthening is expected to plateau as complete saturation of the intercalation sites is approached. However, at concentrations greater than 50 μM bis-NDI, secondary structures formed which did not permit accurate length measurement of single strands. More details about these secondary structures will be discussed in the following section.

The measured lengths were matched to the theoretical model supposing a binding affinity of 4.0×10^4 M^{-1} and an exclusion number of 4 basepairs (Figure 3.12). The binding affinity is based on individual intercalation events and would be about 10^8 per bis-NDI molecule. This closely agrees with the binding affinity of $>10^7$ estimated from DNAse footprinting studies [60]. The exclusion number of four corresponds to one un-intercalated site between each linked intercalating NDI rings and one un-intercalated site between bis-NDI molecules.

Bis-NDI Secondary Structures

The studies not only measured DNA lengthening due to intercalations, they clearly identified conventional condensate structures of toroids, rods, and spheres, as well as the apparent intermediate structures of loops formed by increasing concentrations of bis-NDI. This was particularly interesting because while the compounds were anticipated to intercalate into the DNA, they were not expected to cause DNA condensation

Interactions within single strands and between multiple strands to form complex secondary structures occurred progressively with higher bis-NDI concentrations (Figure 3.13). At bis-NDI concentrations less than 5 μM, the DNA is found primarily as

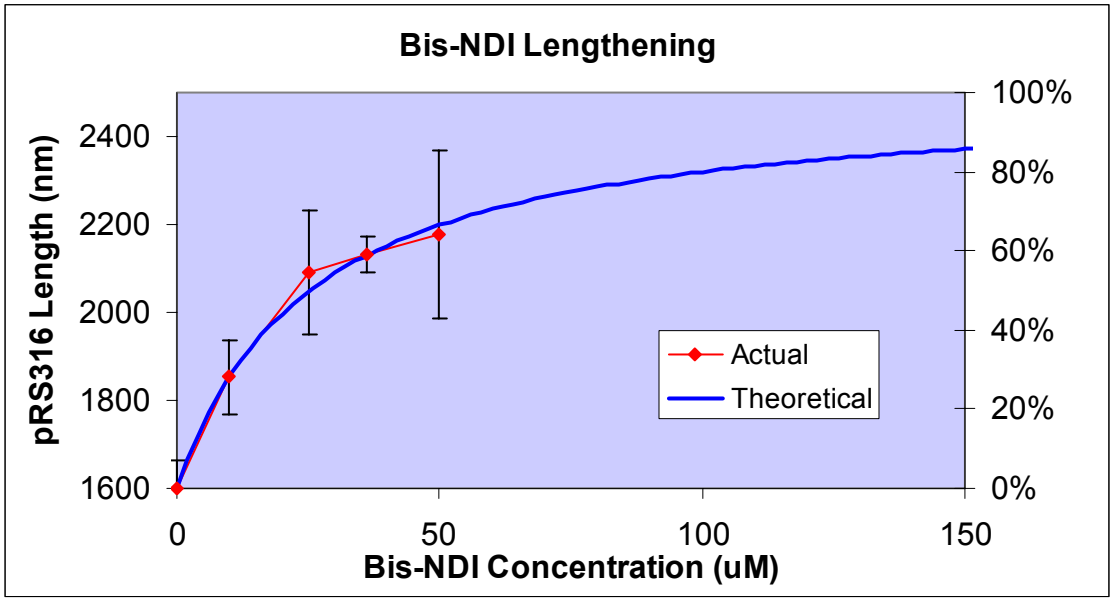

Figure 3.12 Plot of actual pRS316 lengthening with increasing bis-NDI concentration with corresponding theoretical curve calculating a nearest neighbor exclusion number (n) of 4 lengthening per intercalation (a) 0.34 nm, and a binding affinity (Ka) of 4 x 10^4

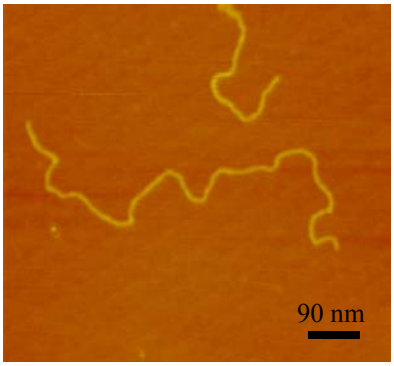

0 μM bis-NDI

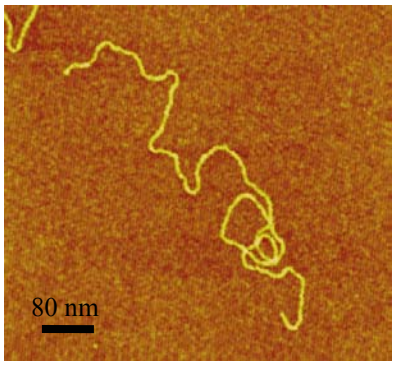

10 μM bis-NDI

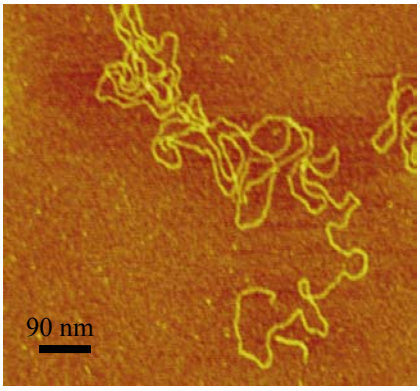

25 μM bis-NDI

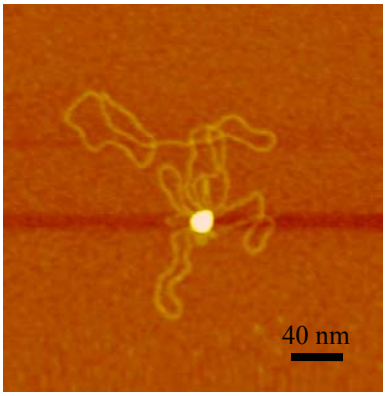

50 μM bis-NDI

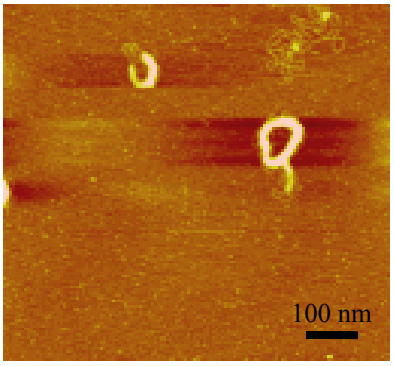

100 μM bis-NDI

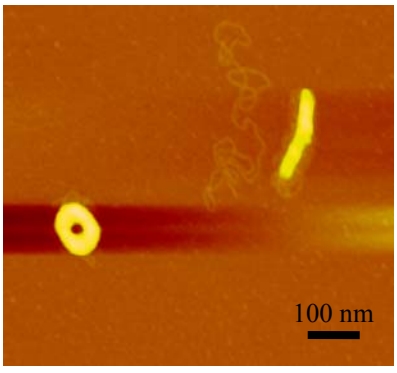

150 μM bis-NDI

Figure 3.13 AFM intermittent contact image of pRS316 plasmid on mica under ambient conditions at increasing bis-NDI concentrations illustrating progression of secondary structures through condensation intermediates to fully formed condensed toroid and rod structures

individual linear strands with only coincidental overlaps. At concentrations between 5 and 10 μM, single and multiple loops began appearing within the strands. At concentrations between 25 and 50 μM clusters of loops that may be formed by multiple strands were observed, sometimes with clear foci at the intersection of several loops. Finally, at concentrations of 100 μM and higher, fully formed toroids, rods, and spheres were observed. Loose strands or loops radiated from many of the toroids and rods. A mixture of the structures were identified at the higher concentrations, as looped strands existed along with the completely condensed structures.

The toroids, rods, and spheres are traditional condensate structures and potential intermediate structures that are similar to those observed by others [84, 85]. The initial phases follow an analogous pattern found by Berge using the bis-intercalator luzopeptin in $MgCl_2$ buffer [82]. Yet Berge did not find complete condensate structures, probably because his studies used short (292 to 500 basepairs) DNA strands. It is necessary for DNA strands to be at least greater than 400 base pairs to form toroids [102].

DNAse footprinting results with this poly-NDI series had puzzling results at high poly-NDI to DNA basepair ratios where all DNAse activity was suddenly lost [60]. These results now make sense in light of the condensation that appears to be occurring which would protect the DNA from ligation. The mono-intercalator did not have this effect (Figure 3.14). The DNAse footprints of the related poly-NDI compounds with a variety of linkers that contained a lysine also showed the same loss of DNAse activity at high

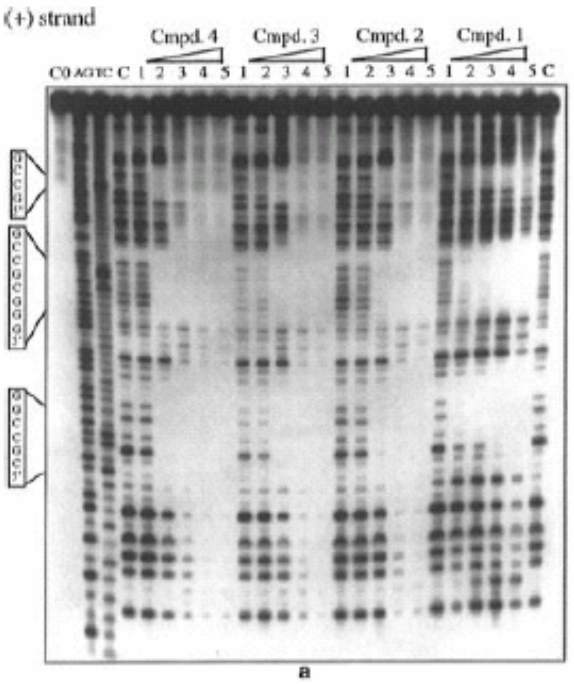

Figure 3.14 DNAse footprint where Cmpd. 1 is the mono-NDI, Cmpd 2 is the bis-NDI, Cmpd. 3 is the tris-NDI, and Cmpd. 4 is the tetra-NDI. Note that no bands occur at the higher concentrations of bis-, tris-, and tetra-NDI indicating protection of the DNA strand from enzymatic activity as would be afforded by condensation [60].

concentrations. Based on this, one can hypothesize that condensation is occurring with all of these molecules regardless of the position of the linker in the major or minor groove.

The intermediate structures formed with bis-NDI were stable through the water rinsing and drying procedures, in contrast to those found by Hoh's group using spermidine [84]. The effect of temperature during incubation of the drug with the DNA was examined with 50 μM bis-NDI at room temperature (25º C), body temperature (36º C), and elevated temperature (70º C). No change in morphology or distribution was found (Figure 3.15).

Tris- and Tetra-Naphthalenetetracarboxylic Diimide

Tris-NDI only had a limited effect on DNA lengthening (Table 3.3). It appeared that the plasmid lengths were slightly shortened, perhaps due to kinking and knotting of the strands. The formation of secondary structures begins at a low concentration of about 1 μM, preventing measurement of individual strand lengths.

Tetra-NDI also demonstrated slight concentration-dependent lengthening at extremely low drug concentrations (Table 3.4). The formation of secondary structures occurs at concentrations greater than 0.1 μM, again preventing measurement of individual strand lengths. Using the limited lengthening data and the direction provided by the bis-NDI model, the binding affinity was estimated to be 4×10^{12} with an exclusion number of 8 basepairs for tetra-NDI. This exclusion number is consistent with the bis-NDI pattern of one un-intercalated site between each linked intercalating NDI rings and one un-intercalated site between poly-NDI molecules.

a

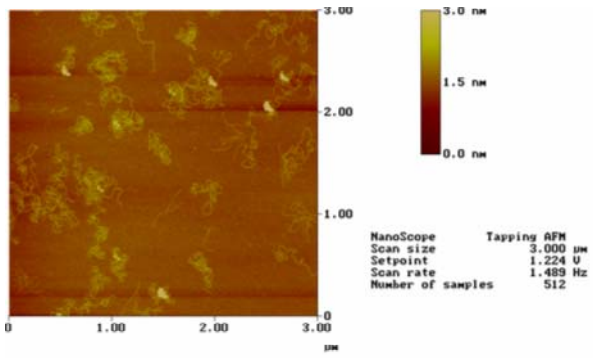

b

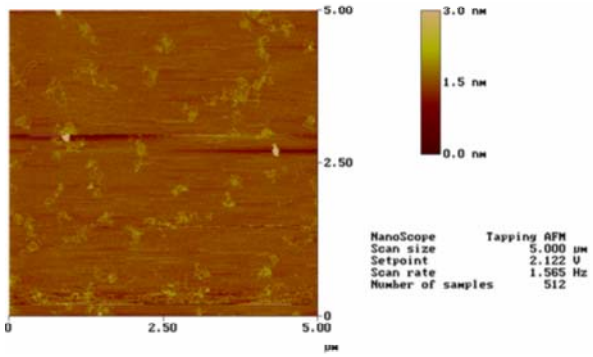

c

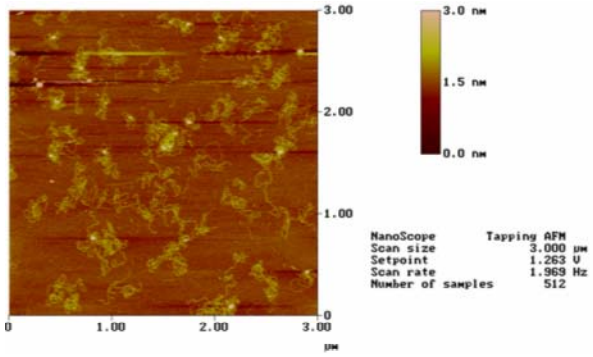

Figure 3.15 AFM images of pRS316 with 50 µm bis-NDI at three incubation temperatures a) ambient (~25˚ C), b) body temperature (36˚ C), and c) elevated temperature (70˚ C) showing no significant difference in secondary structure produced by temperature

Table 3.3 Length measurements of pRS316 with increasing concentrations of tris-NDI that reveal shortening, possibly due to kinking or knotting of the strands

Tris-NDI Concentration (μM)	Tris-NDI Compound : pRS316 Basepair Ratio	Average Strand Length (nm)	Standard Deviation (nm)
0	0	1660	118
0.0014	1: 1000	1535	79
0.014	1:100	1525	87
0.07	1:50	1630	131

Table 3.4 Concentration-dependent lengthening of pRS316 plasmid with tetra-NDI at extremely low concentrations

Tetra-NDI Concentration (μM)	Tetra-NDI Compound : pRS316 Basepair Ratio	Average Strand Length (nm)	Standard Deviation (nm)
0	0	1660	118
0.0014	1: 1000	1735	69
0.014	1:100	1823	100

Tris-NDI and tetra-NDI followed the same morphology sequence as bis-NDI, but at much lower concentrations, even when corrected on a per intercalation unit (Figures 3.16 and 3.17). This may indicate that cooperativity is occurring between the intercalation units of the molecule and perhaps between NDI molecules. At extremely low concentrations of tris- or tetra-NDI, linear strands could be found, but with a slight increase in concentration loops began to form. At slightly higher concentrations thick loops which looked like pre-toroids formed within strands, then rods, spheres, and toroids were identified (Figure 3.16).

Thus, it has been determined using AFM that poly-NDI compounds interact with pRS316 DNA and change its length and conformation. It has been conclusively demonstrated based on plasmid lengthening and bis- and tetra-NDI are intercalating with high binding affinities. Low concentrations of tris-NDI may also be intercalating, but the data was complicated by suspected strand deformations. In addition, the unexpected ability of these poly-intercalators to cause DNA condensation was demonstrated.

Discussion

The condensation process is induced by poly-NDI intercalation. The role of Mg^{+2} in this process is unknown since the $MgCl_2$ buffer concentration remained constant. Control samples with $MgCl_2$ but without poly-NDI were devoid of DNA condensates. The $MgCl_2$ was required for immobilization of the DNA on the mica surface for AFM imaging. It has been shown that magnesium ions make DNA more flexible, especially in the AT regions

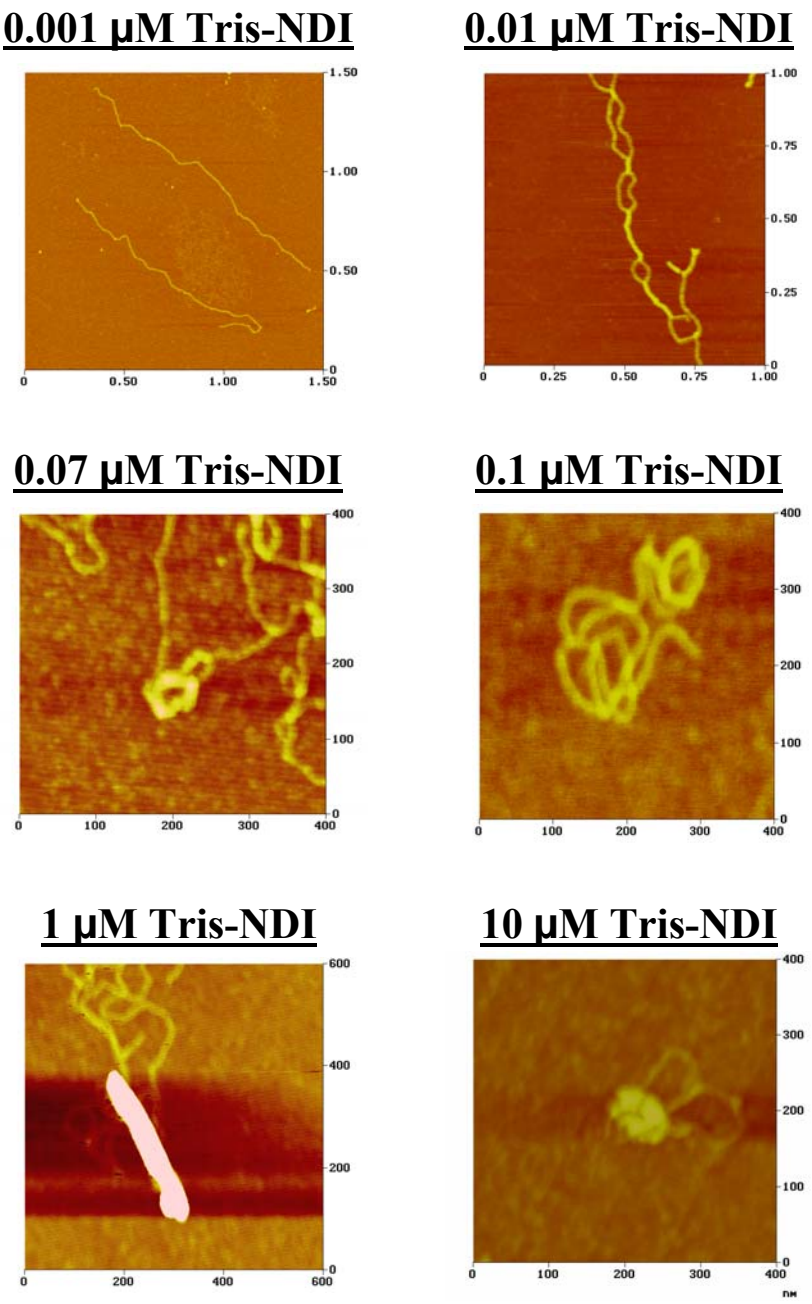

Figure 3.16 AFM intermittent contact image of pRS316 plasmid on mica under ambient conditions at increasing tris-NDI concentrations illustrating progression of secondary structures through condensation intermediates to fully formed condensed structures

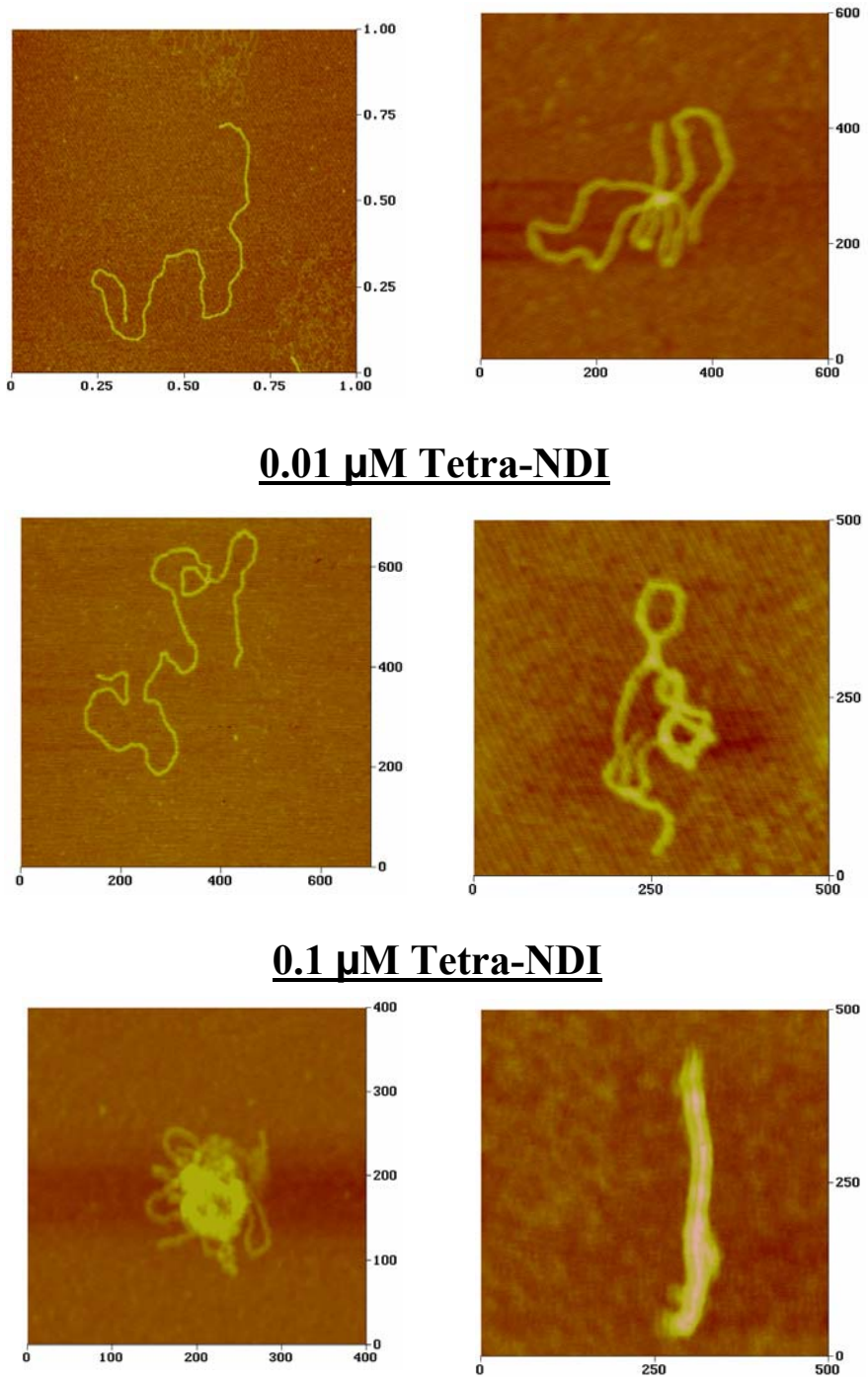

Figure 3.17 AFM intermittent contact image of pRS316 plasmid on mica under ambient conditions at increasing tetra-NDI concentrations illustrating progression of secondary structures through condensation intermediates to fully formed condensed structures

[103], leading to bending and stabilizing side-by-side association of DNA [104], conformational changes [105], including major and minor groove binding and changing width [106]. It has been determined that divalent cations, such as Mg^{+2} cause aggregation at high concentrations (> 200 mM), but are not capable of DNA condensation on their own [107].

The lysine in the NDI linker provides a positive charge that may promote condensation. As mentioned in Chapter 2, condensation has been shown to occur with 90% neutralization of the anionic phosphate backbone. Because the poly-NDI molecule does did not have strong DNA sequence specificity, stable electrostatic interactions could not be formed at any sequence location. Therefore, the location of the lysine in relation to the DNA grooves cannot be specifically determined using NMR.

A linker composed of the same amino acids in a different order with the lysine at the C-terminus end of the tri-glycine had a substantial binding preference for a GC-rich palindrome sequence. NMR analysis of this molecule indicates that the lysine amine group extends from the major groove where it can interact with the anionic phosphate backbone [67]. A linker with tri-alanine substituted for the tri-glycine had a significantly different binding preference for an AT-rich palindrome sequence. NMR analysis of this molecule indicates that the linker binds in the minor groove, instead of the major groove, but again allows the lysine amine group to extend where it could interact with the anionic phosphate backbone [68].

The lengthening of the DNA at lower poly-NDI concentrations confirms that intercalation is occurring. The loops that are formed may be the result of intra- or inter-strand intercalation or merely stabilization of interactions at the cross-over points. Loop formation has been hypothesized as the initial template for toroid formation [108].

Interaction Models

Several models are proposed to describe the interaction of the poly-NDI molecules with DNA. The first set of models are based on sequential intercalation of all of the ring structures occurs (Figure 3.18). These models are generally consistent with the NMR images of the related poly-NDI compounds. As discussed above, the driving force for condensation in the model would primarily be based on the neutralization provided by the lysine. In addition, this model could rely on the bound intercalator to stabilize quadruplex-like structures that could arise in the condensate tertiary structures, as has been shown to be facilitated by other molecule/DNA complexes [109].

The second set of models require both mono-intercalation and groove binding of the second ring structure (Figure 3.19).This model infers that the binding affinity of poly-NDI for the groove is comparable to that for intercalation. The binding affinity to the groove cannot be determined by AFM and is presently unknown. Models of only groove-binding or non-classical interactions were eliminated based on the evidence of DNA lengthening which substantiates that some intercalation is occurring. A third set of models is based on intrastrand or interstrand cross-over binding (Figure 3.20). In these models one ring intercalates and the second ring either intercalates, groove-binds, or

otherwise binds to a remote area of the DNA. It can be envisioned how these models would account for loop formation that was observed in the secondary structures with lower poly-NDI concentrations believed to be condensate intermediates. It has been conjectured that loops may serve as a template for condensation [110]. Condensation theories and formation process hypotheses will be discussed further in the next chapter.

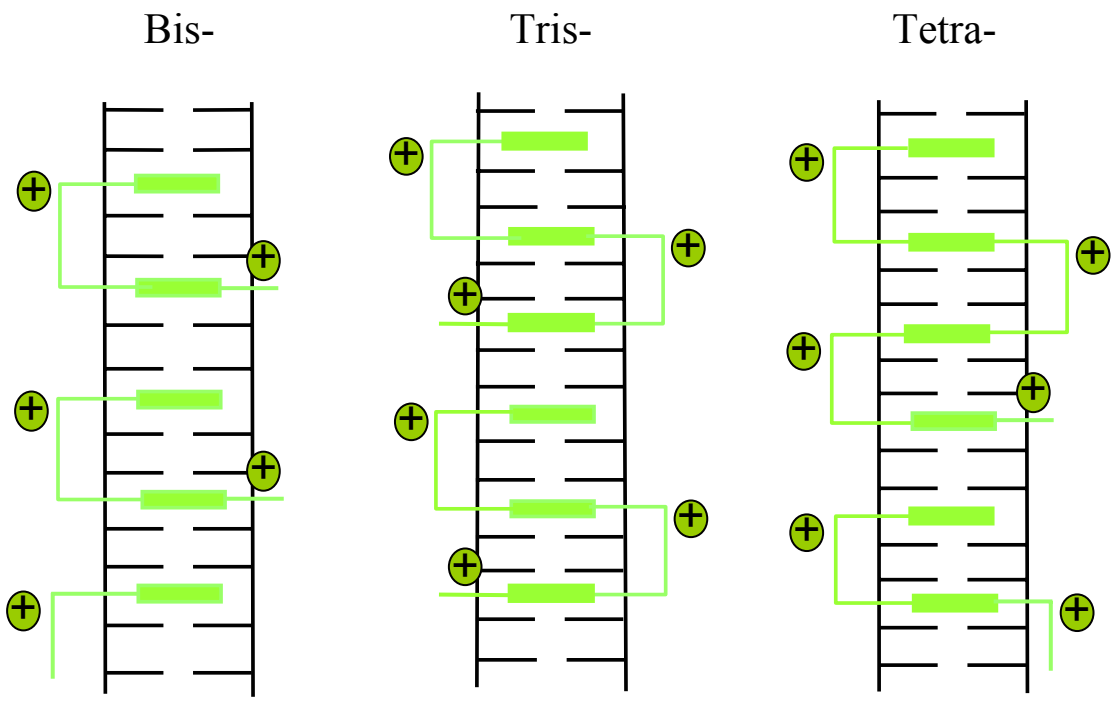

Figure 3.18 Models of sequential intercalation of each ring moiety of the bis-, tris- and tetra-NDI molecules representing nearest neighbor exclusion numbers of 4, 6, and 8, respectively where there is one open site between rings of the same poly-NDI molecule and one open site between molecules

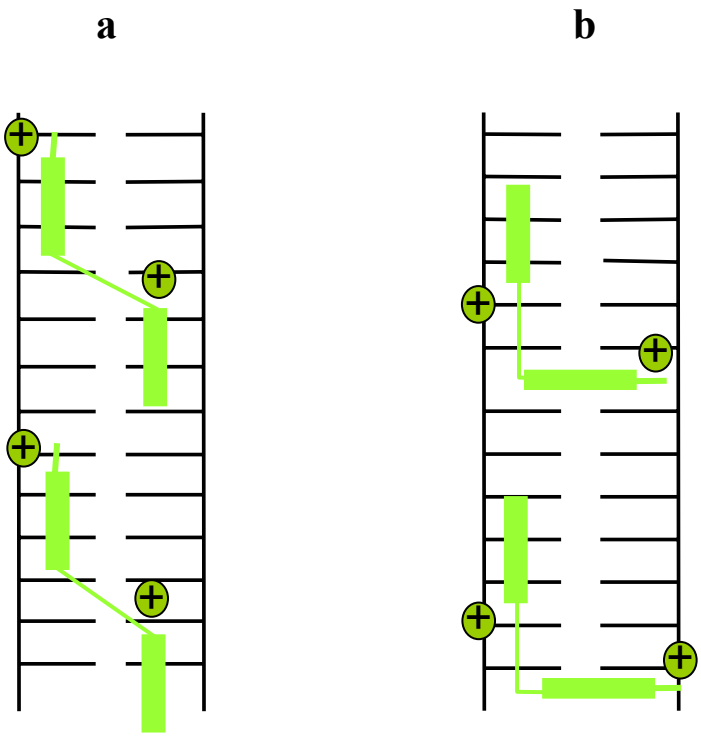

Figure 3.19 Models involving groove-binding of the poly-NDI ring either exclusively (a) or in combination with intercalation (b). Lengthening measured with increased concentration of poly-NDI confirms that at least some intercalation is occurring, thus excluding model a.

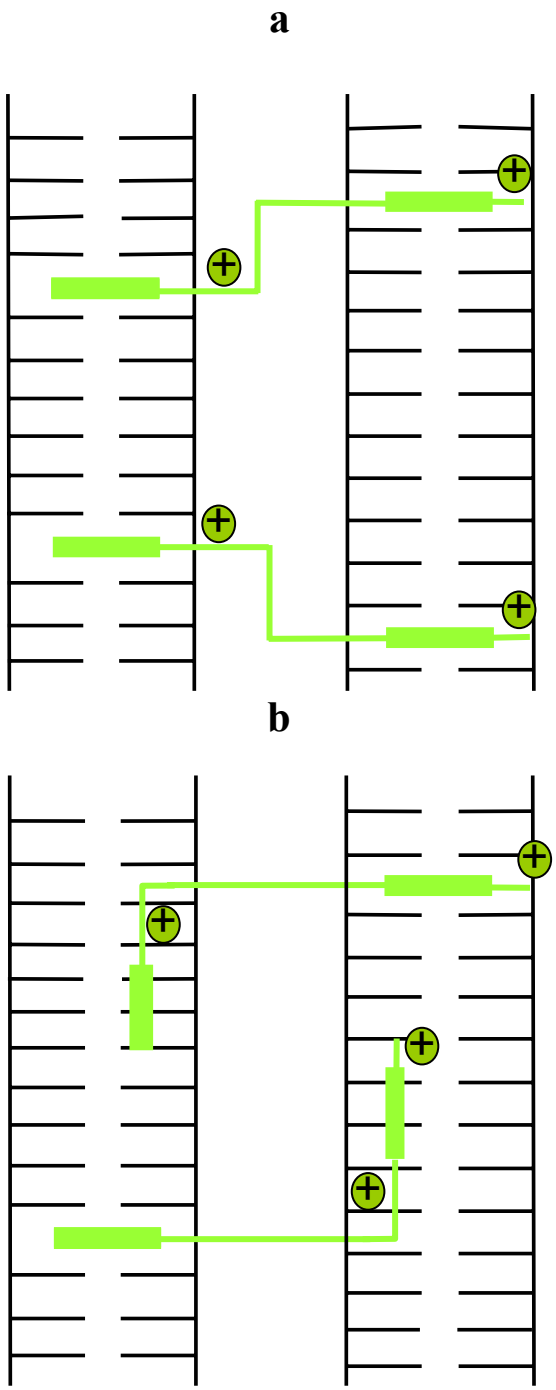

Figure 3.20 Models of inter-strand or intra-strand intercalation (a) of ring moieties in which the rings from one poly-NDI molecule intercalate in remote areas of either the same DNA strand or of different DNA strands. Alternatively, one ring moiety may intercalate while the other may undergo groove binding (b). These models can be interpreted to facilitate loop formation which may serve as a template for condensation or to stabilize condensate structures.

CHAPTER 4

ANALYSIS OF TOROID FORMATION WITH POLY-NAPHTHALENETETRACARBOXYILIC DIIMIDE

Introduction

The toroid form is quite striking and the driving forces that lead to it, in preference to other geometries, are perplexing. Its spontaneous formation by DNA *in vitro* in the presence of condensing agents that mimic those found *in vivo* has facilitated studies into the energetics of DNA toroid formation. While toroids were first identified in 1972 by Evdokimov *et. al* [111], a clear understanding of the mechanism of formation has yet to be determined. Over a hundred journal articles on DNA toroids have been published in the past five years. They are of key interest for applications in gene therapy delivery and antiviral treatments.

Formation Driving Forces Theories

There are several theories about the condensation process and its driving factors. One of the keys appears to be the stiffness of the DNA caused by the weak attractive force between DNA segments [69]. Some contend that condensation is due to electrostatic interactions which dominate entropy [112]. Others contend that hydration is the dominating attractive force responsible for condensation. The original Manning counterion condensation theory is based on the ratio of Bjerrum length to the charge separation distance being greater than one in order for condensation to occur [113]. This

is independent of counterion valency; therefore condensation must be more complex, as it has been shown the condensation is dependent on valency. The Debye-Huckel and Poisson-Boltzmann theories are not valid for DNA, especially with multivalent cations, because the Coulombic interactions are strong compared to the Boltzmann constant. The Poisson-Boltzmann theory would predict that the negatively charged DNA molecules should repel each other regardless of the charge of the neutralizing couterion [114]. Multivalency increases the magnitude of Coulombic interactions which allows it to overcome entropy for net attraction between like-charged ions. Manning later proposed that DNA bending occurs at this critical charge neutralization fraction which leads to the spontaneous formation of toroids [115]. A general notion exists that condensation takes place with 90% neutralization [103]. The correlated counterion fluctuation theory which accounts for attractive forces between the polyelectrolyte with same charge regions has a strong following and estimates greater counter ion adsorption than the Manning condensation model [116, 117].

Small angle neutron scattering experiments measured the partial structure factors of DNA and polyamine density correlations and determined that the polyamines are too large to penetrate into the grooves, which implies that their function in condensation is primarily electrostatic, rather than based on multivalent cation binding [118]. Based on NMR structures of related compounds, it has been hypothesized that the lysine which provides the positive amine charge to the poly-NDI structures is extending from the major groove which would place it in good proximity to the negatively charged phosphate backbone.

Toroid Dimensions

Toroid Shape

The toroid structures that were formed by pRS316 linear plasmid DNA in the presence of high poly-naphthalenetetracarboxylic diimide (NDI) concentrations varied in size and shape (Figure 4.1). Many were oblong and several had "tails" or loops. The angle at which the toroid may be lying on the surface also distorts the shape. The variation is not unusual based on other published images of toroids analyzed with AFM [119, 120].

A true hole, as opposed to a cavity or indention, appears to be present based on sectional analysis of toroids with larger inner diameters (Figure 4.2). The height of the center of toroids with smaller inner diameters does not clearly show a return to surface level, but this is likely an artifact of the AFM's ability to adjust to sudden changes in height or due to the orientation of the toroid on the surface

Toroid Diameters

Measurement of toroid outer and inner diameters was of interest to validate that the toroids formed with poly-NDI were similar to those formed with traditional condensing agents. It could also be used to determine the toroid volume to help elucidate the number of DNA strands composing each toroid.

Measurements of toroid diameters were performed using the Nanoscope software in the top view mode and section analysis mode (using half-height values) along the horizontal and vertical axes of the toroid (Figure 4.2). Results from both modes were similar

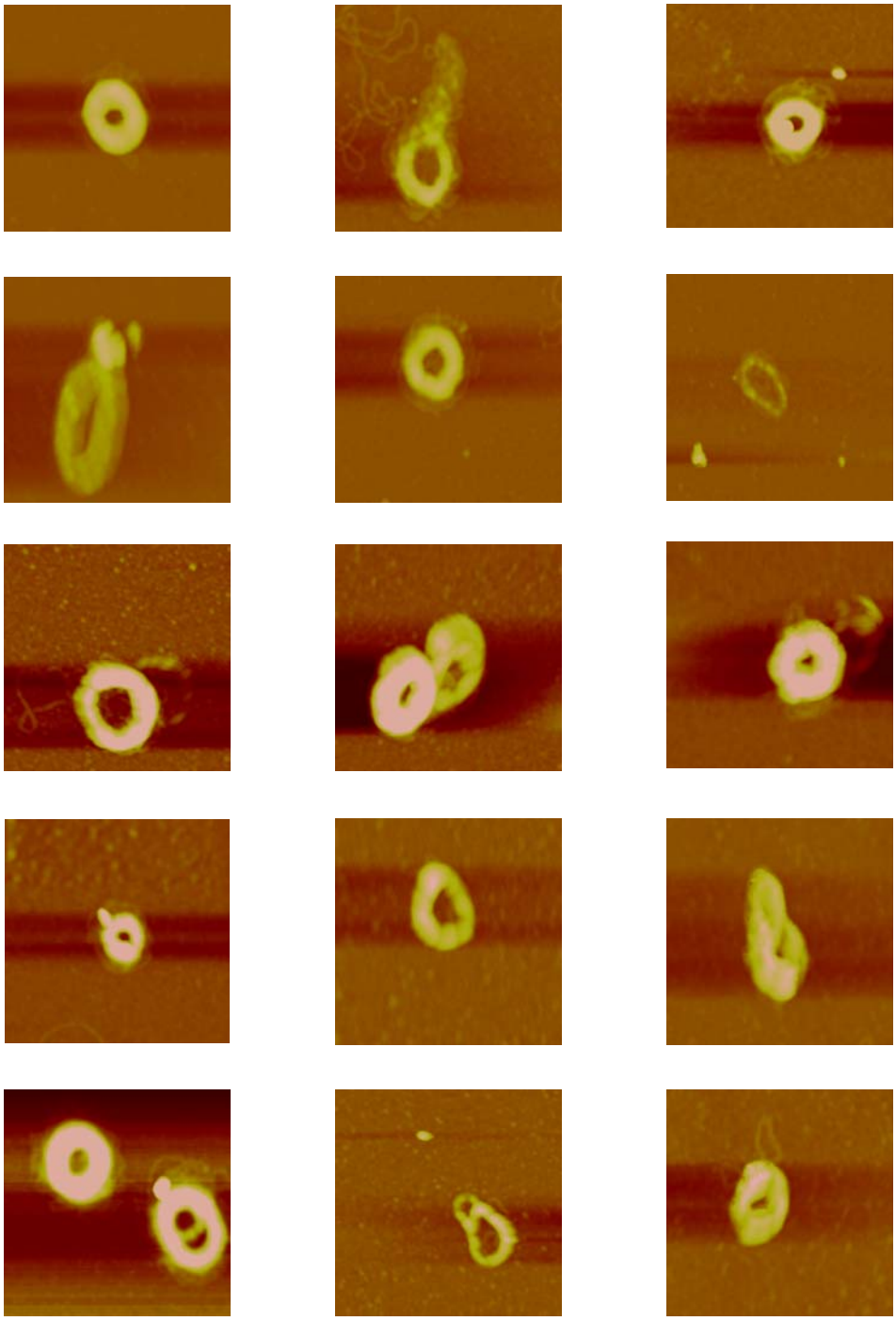

Figure 4.1 Portfolio of AFM images (400 nm scan sizes) of representative toroid structures formed by pRS316 and bis-NDI illustrating the diversity of toroid shapes and sizes

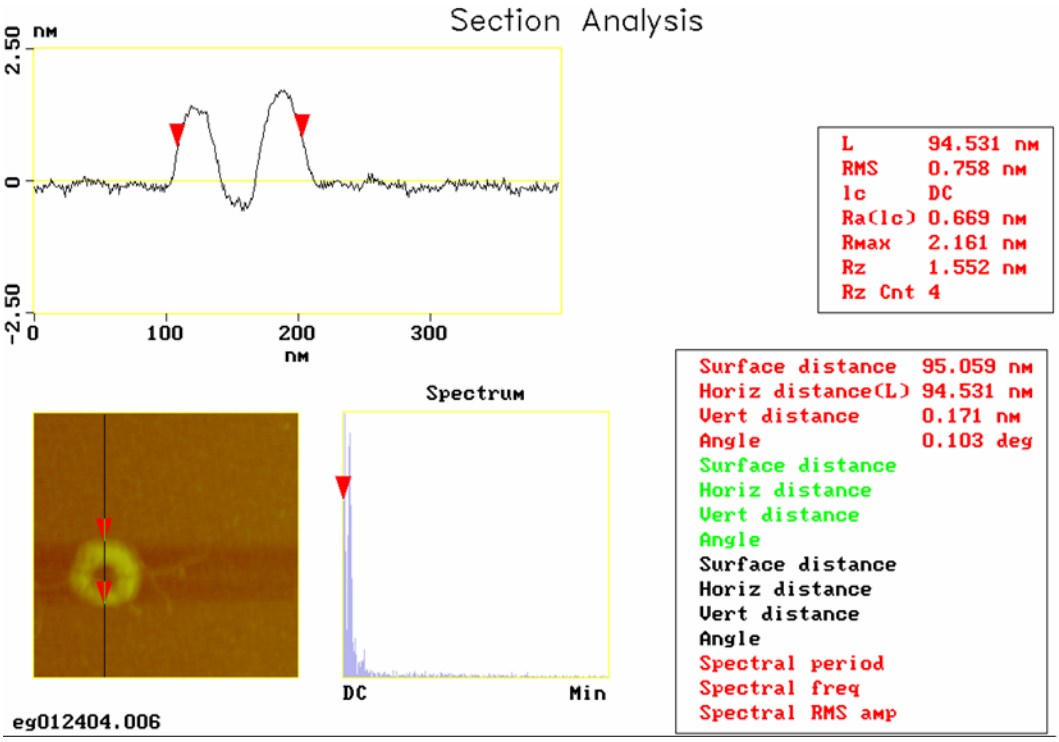

Figure 4.2 Sectional analysis of toroid with half-height measurements of outer diameter (o.d.) and inner diameter (i.d.)

although the top view tended to be greater, as expected based on the use of half-height values for the sectional analysis. Half-height measurements are generally accepted as providing more accurate data by reducing the impact of tip geometry on measured widths; therefore, these measurements were used in these studies.

The toroids formed with poly-NDI had measurements averaging 90 to 150 nm outer diameter and 25 to 45 nm inner diameter (Table 4.1) which matches that of toroids formed with traditional condensing agents such as spermidine [121], polylysine [85], pegylated polymers [122], and others as measured by AFM and electron microscopy (EM) (Table 4.2). Dynamic light scattering (DLS) studies measured hydrodynamic radii of 40 to 60 nm for toroids in solution [70] [123] which has been interpreted to generally correspond well with the measurements similar to those obtained in our studies. Toroids formed with bis-NDI and tetra-NDI were similar in diameters. Very few clear individual toroids were identified with tris-NDI, although spheres and thick loops within strands were frequently formed with tris-NDI (Figure 3.16).

The poly-NDI / pRS316 strand loops were found to be approximately 60 nm outer diameter which was about half of the diameter of the toroids and spheres. The radius of DNA loops in solution and the radius of toroids have been found to be similar [108]. This may support the notion that DNA loops that spontaneously form or are designed into the molecule serve as nucleation points for toroid formation [110].

The impact of the AFM tip diameter on width measurements should be taken into

Table 4.1 Toroid dimensions as measured from sectional analysis of AFM images using half-height measurements for diameters

Poly-NDI Compound	Outer Diameter (nm)	Inner Diameter (nm)	Width (nm)	Height (nm)
Bis-NDI (150 μM)	129 ± 42	42 ± 19	44	5.0 ± 3.0
Bis-NDI (100 μM)	146 ± 44	36 ± 19	55	5.1 ± 1.0
Tris-NDI*	58 ± 14			4.2 ± 1.7
Tetra-NDI	91 ± 11	28 ± 8	32	2.2 ± 1.1

* spheres, not toroids

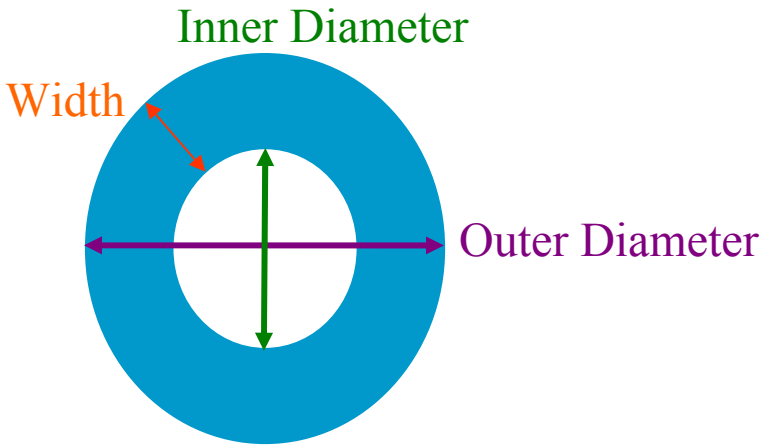

Table 4.2 Dimensions of toroids formed with classical condensing agents collected from the literature. These measurements of diameter and height are in good agreement with those found for poly-NDI.

Reference	OD (nm)	Height (nm)	Condensation Agent	DNA Plasmid	Method of Analysis
[120]	117 to 191	2.61 ± 0.77	spermine, polyamines	5256 bp, circular	AFM
[85]	142.1 ± 3.1	3.7 ± 0.1	polylysine-AsOR	6832 bp, circular	AFM
[124]	82.8 ± 9.7	9.6 ± 1.6	protamine	7500 bp, linear	AFM
[125]	120 ± 15	17 ± 2	spermidine	48000 bp	AFM
[122]	133 ± 23		pegylated polymer	4365 bp and 6000 bp	AFM
[24]		8	Ni II		AFM
[126]	95 to 185	~50	hexammine cobalt	48000 bp	TEM
[127]	200		spermidine	T4 (large)	EM
[108]	80 to 118		hexammine cobalt	4500 bp	TEM
[114]	111.8 ± 37.8		Ni II	800 bp	AFM
[128]	90		hexamine cobalt	2700 and 1350 bp	EM
[129]	40		silanes AEEA	4361 bp	AFM

consideration. An increase of the apparent DNA strand width has been demonstrated to be dependent upon humidity [80]. Tip deconvolution was not conducted for the analysis of the toroids due to its small impact compared to the significant deviations between toroid samples.

Toroid Height

As noted in chapter 1, AFM is known for its high resolution in the z-direction. The heights of toroids, loops, and strands were measured using the Nanoscope software sectional analysis tool. Toroids and rods had irregular heights and, therefore, were measured along the vertical, horizontal, and diagonal axes and averaged. Toroid heights with poly-NDI / pRS316 ranged from 0.7 to 15 nm, with a majority of the heights between 2 and 10 nm and a mean of 5 nm. This is in general agreement with previously published heights for toroids formed with traditional condensing agents such as spermine [120], polylysine [85], protamine [79], and others as measured by AFM (Table 4.2).

It was surprising that the heights of the toroids were about an order of magnitude less than the width of the toroid ring which would lead to an interpretation of an oval cross-section (Figure 4.3). Most studies using EM, which lacks the ability to determine z-range distances, have assumed that the toroids were of the classic mathematical torus structure with a circular cross-section, hence their name. It is known that AFM measurements of DNA strand heights are lower than the theoretical height of DNA. A recent study by Moreno-Herrero, *et al*. [130] explored this anomaly and concluded that the molecules

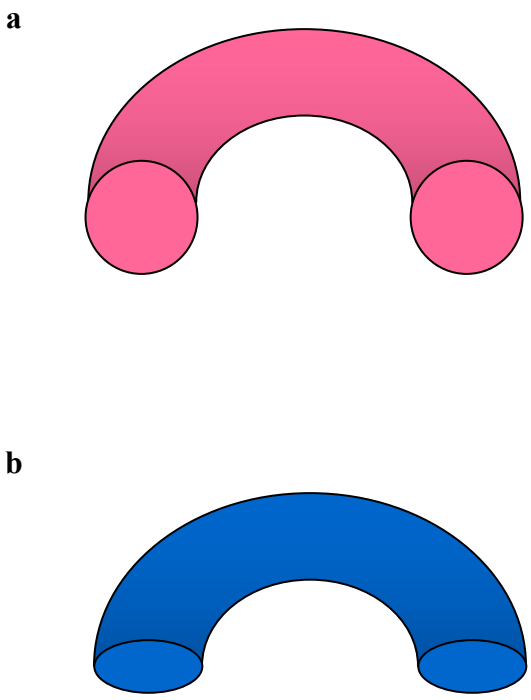

Figure 4.3 Representation of toroid with a) circular cross-section and b) oval cross-sectional

may be embedded in a salt layer covering the mica surface which could account for part of the height difference, while the force exerted by the oscillating tip during imaging could further distort the apparent height [79].

Toroid Compression

Contact Mode

In order to determine if the force exerted by the AFM tip on the sample was compressing the toroids, a series of experiments were conducted using different imaging modes and cantilevers with different spring constants. Contact mode AFM was performed using a Sharp Microlever™ (model MSCT-A4FW) triangular cantilever at a range of setpoints from the minimum required to maintain contact to a force large enough to dislocate structures on the surface. The topographical images correspond to the increased force (Figure 4.4). However, the height of the toroid and rod, as measured with the sectional analysis, did not change with the exception of when they were reoriented on the mica surface (Table 4.3 and Figure 4.5). These results indicate that the condensate structures were either being compressed fully upon the initial setpoint or not compressed significantly even at the highest set point.

The forces between the tip and the sample were calculated using Hooke's law and the data from the AFM force curve using the following equation:

$$F = k(\Delta Z) \qquad \text{Equation 4.1}$$

where F is the contact force, k is the cantilever spring constant, and ΔZ is the movement of the piezoelectric scanner required to move the sample from the setpoint value to the tip

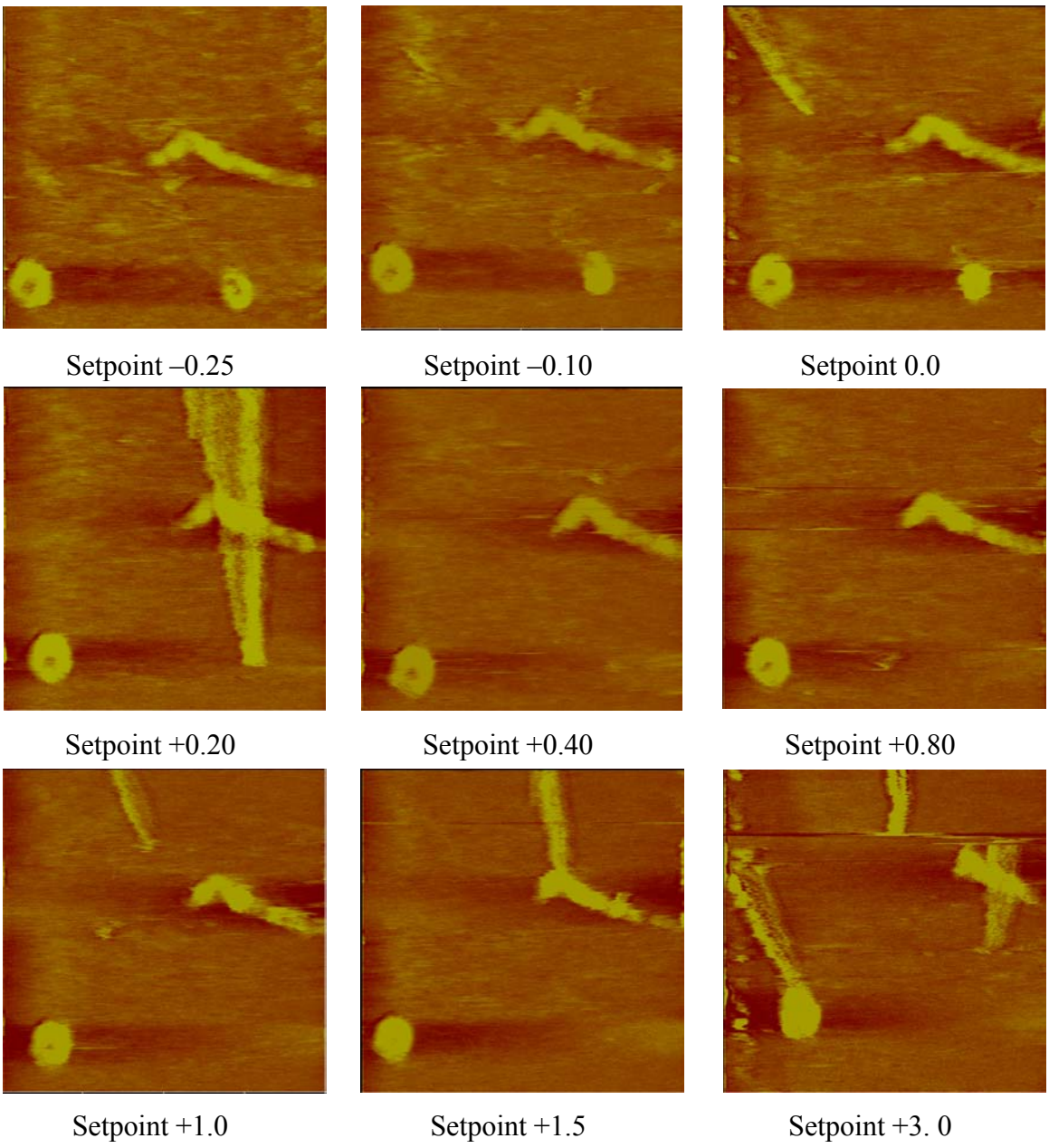

Figure 4.4 AFM contact mode images (800 nm scan size) of toroids and rod with increasing force exerted by tip on sample

Table 4.3 Condensate structure height at increasing set points and corresponding calculated contact forces and pressures. Heights were determined as the average of three sectional analyses along the horizontal, vertical, and diagonal axes of the contact mode image.

Set Point (V)	**Total Force (nN)**	**Repulsive Force (nN)**	**Pressure (megaPa)**	**Toroid Height (nm)**	**Rod Height (nm)**
-0.25	24.3	-0.66	-0.21	2.98	2.63
-0.10	24.7	-0.27	-0.08	2.92	2.65
0.00	25.0	0.00	0.00	3.03	2.23
0.20	25.5	0.53	0.17	2.94	ND
0.40	26.0	1.06	0.33	2.97	2.56
0.80	27.1	2.13	0.67	2.85	3.09
1.00	27.6	2.66	0.84	2.87	3.59
1.50	28.9	3.99	1.25	2.98	4.32
3.00	32.9	7.97	2.51	4.50	ND

ND= not determined
Note: Underlined values denote that the structure was visibly reoriented on the mica surface (see Figure 4.4)

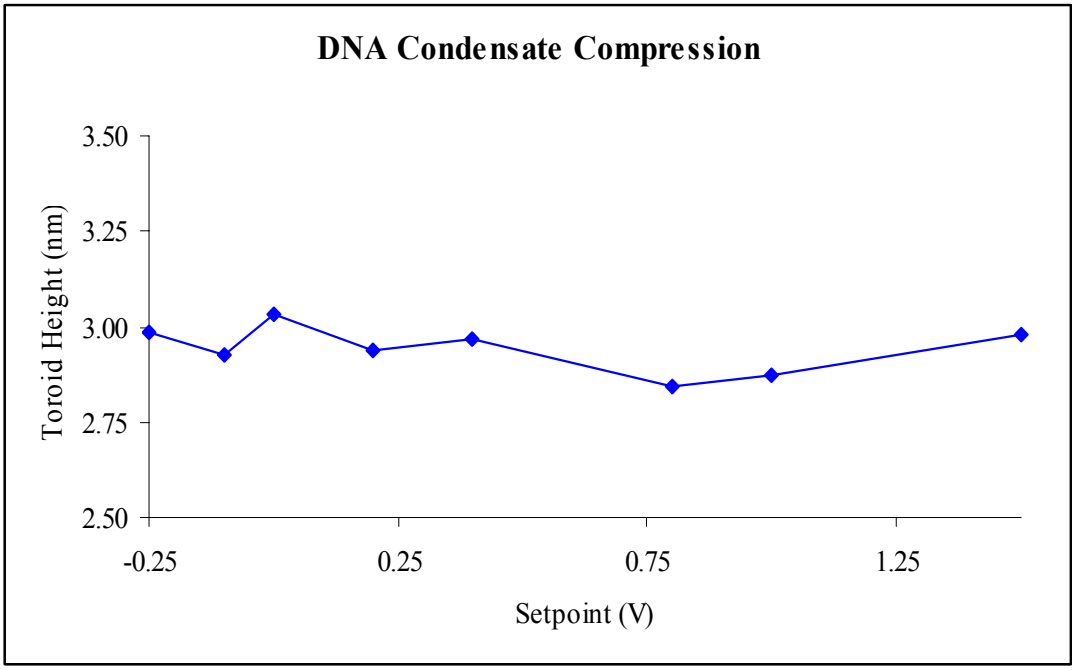

Figure 4.5 Plot of toroid height demonstrating no significant change with increasing contact force between the tip and sample using contact mode AFM

pull-off (rebound) point. The strong capillary forces of the hydration layer caused the rebound point to be outside the range of the detector; therefore, the retraction lines were extrapolated to determine the ΔZ value (Figure 4.6). The spring constant (k) of 0.03 N/m provided by the manufacturer was used for the calculations. The total force between the tip and the sample ranged from 24 nN to 33 nN (Table 4.3). However, a majority of this force can be attributed to the capillary force in which the water layer is pulling down on the cantilever, as opposed to force of the tip on the sample (Figure 4.7). A repulsive force of only a maximum of about 8 nN and a pressure of 2.5 megaPascals was obtained when the capillary force was deducted (Table 4.3).

These are extremely low forces and would not be expected to compress the toroid. The theoretical pressure and force required to deform the toroid from a circular cross-section to an oval cross-section were estimated using Hooke's law of elastic deformation:

$$\frac{\Delta h}{h} = \frac{P}{E} \qquad \text{Equation 4.2}$$

where Δh is the deformation, h is the total height, E is Young's modulus, and P is pressure. To estimate the deformation that would take place to compress a toroid with a width of 55 nm from a circular cross-section to an oval cross-section with a measured height of 5 nm, it would be assumed that the original total height would have been 55 nm. However, due to known tip artifacts that can broaden AFM width measurements, a conservative estimate of 45 nm was used. Another conservative assumption was made to use the Young's modulus of a DNA strand (0.34×10^9 N/m^2) [130] which would be expected to be significantly lower than that of the compact toroid structure. Based on these assumptions, the required compression pressure would be approximately 300 MPa.

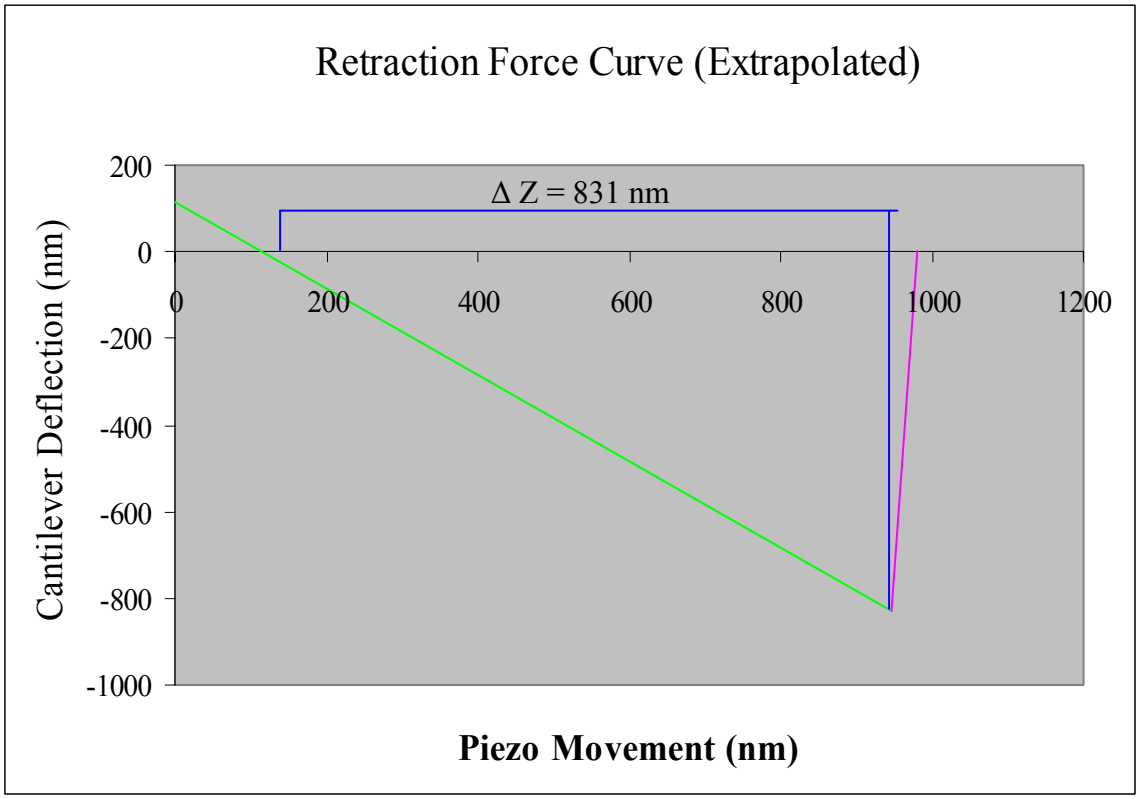

Figure 4.6 Force curve from with contact mode experiment exported to a Microsoft Excel® spreadsheet and replotted using a macro developed by Mark Poggi. Retraction curve extrapolated to define rebound point.

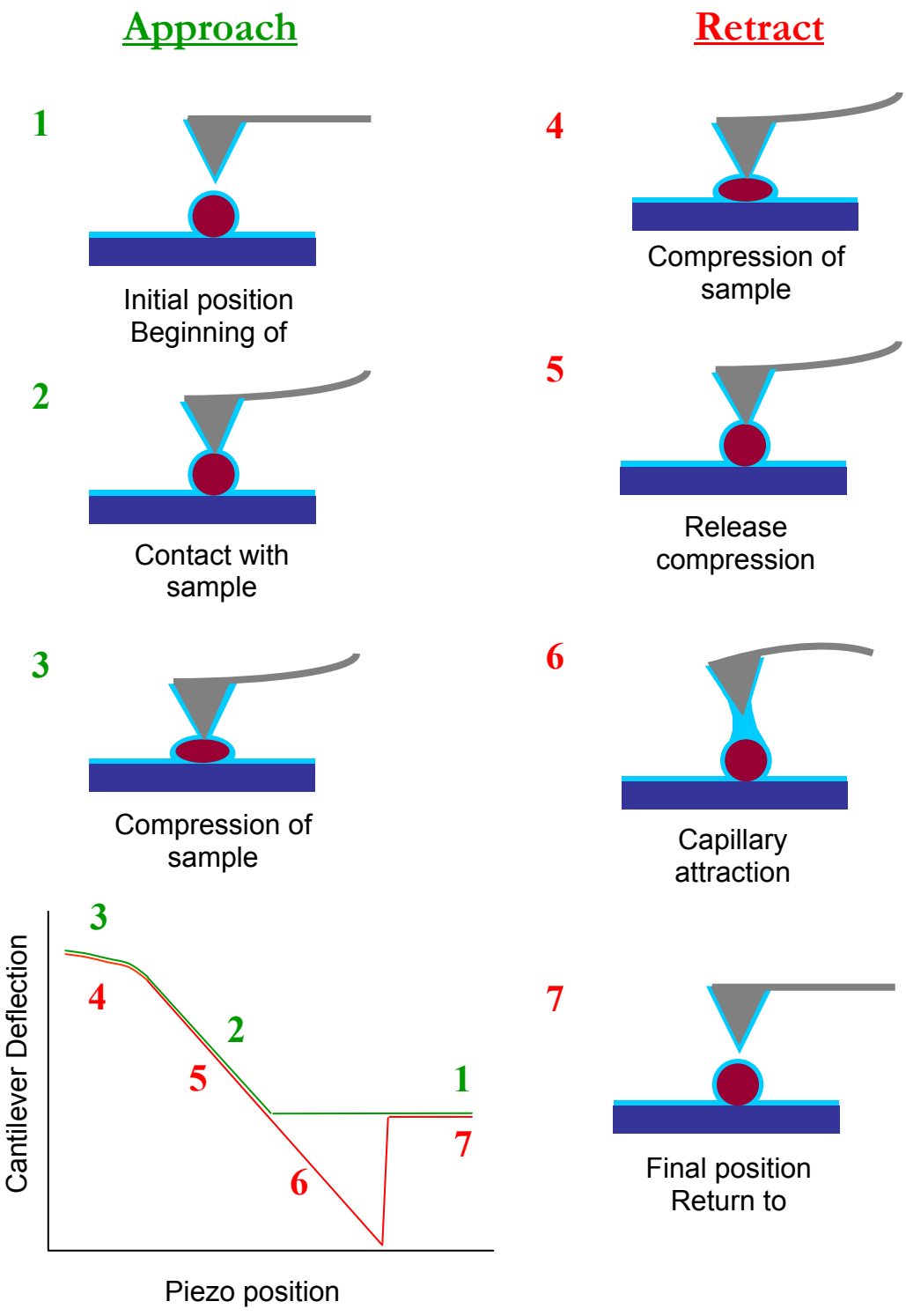

Figure 4.7 Depiction of force curve with sample compression in the repulsive region (3 and 4) and capillary attraction (6)

The estimated tip radius of curvature is 10 nm which would give a tip contact area of about 300 nm, resulting in a necessary compression force almost 100 nN. This is clearly several orders of magnitude greater than the repulsive forces calculated for the toroid imaging.

The experiment was repeated under a nitrogen environment and the results were equivalent. In addition, a force volume experiment was attempted under nitrogen, but the capillary forces were greater than the deflection that would be associated with compressing a several nanometer sized structure.

Tapping Mode

The original toroid measurements were acquired using tapping mode which is the preferred mode for soft biomolecules due to its minimal force exerted on the sample. The actual force exerted by the tip on the sample was not calculated due to the complex nature of determining the cantilever mass and amount of dampening. Height and phase images were acquired at decreasing set points (related to increasing interaction forces) starting at the RMS value. The height images do not show any notable changes, while the phase images have reduced contrast with increased force, as would be anticipated due to higher forces reducing the amount of oscillation change (Figure 4.8). Again, the height of the toroid and rod did not change, as measured with the sectional analysis (Table 4.4 and Figure 4.9). A brief tapping mode study using the Hi'Res probe (Figure 1.3c) at a minimal contact force due to the delicate nature of the tip also determined a similar toroid height (Figure 4.10).

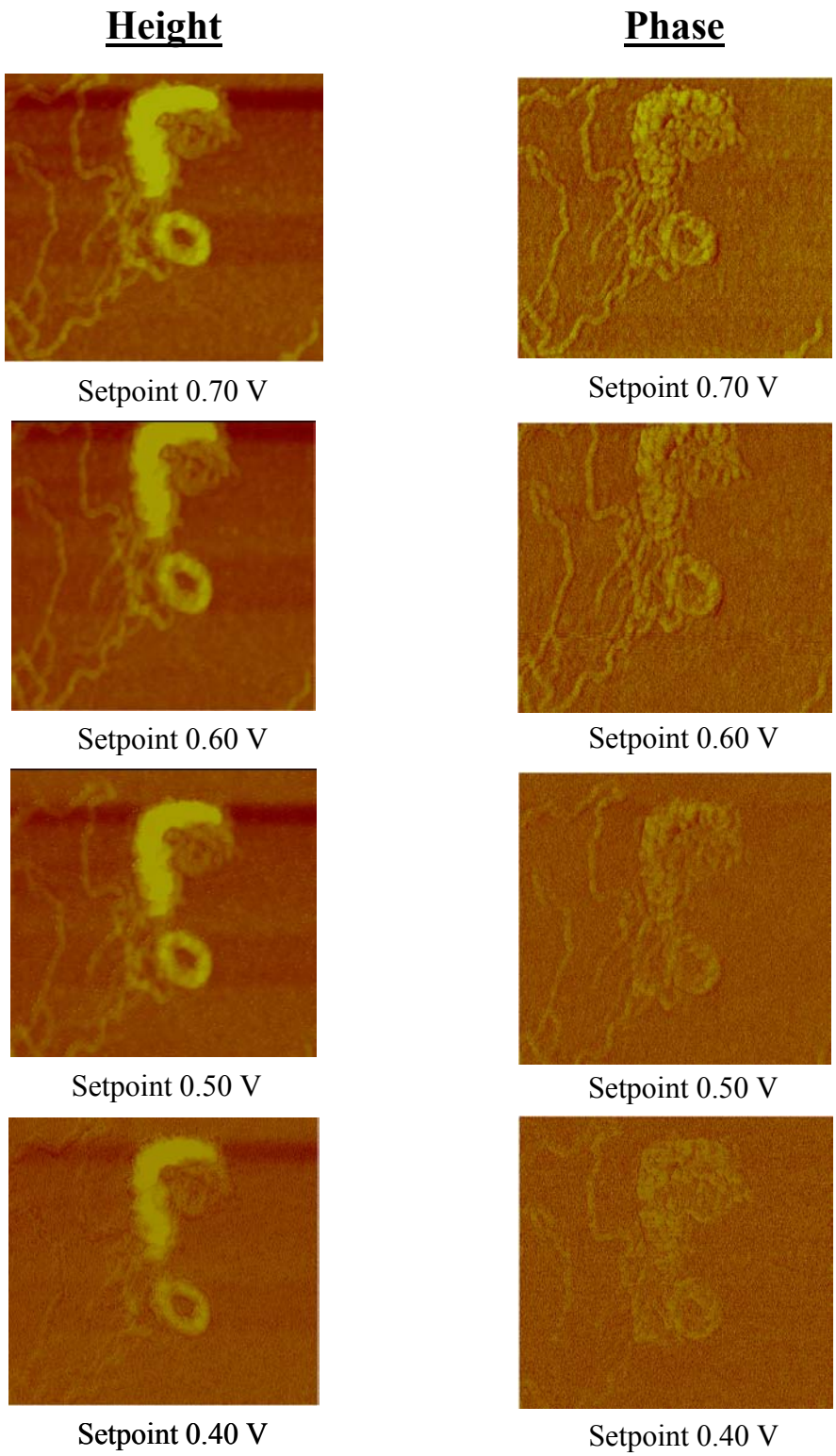

Figure 4.8 AFM tapping mode height and phase images (600 nm scan size) obtained with a Nanoscope IIIa, Extended base, and J scanner with increasing tip interaction forces

Table 4.4 Toroid, rod, and strand heights at decreasing set points (increasing interaction forces) as measured by sectional analysis of tapping mode topographical height images

	Height (nm)			
Setpoint (V)	Toroid 1	Toroid 2	Rod	Strand
1.15	2.11	ND	ND	ND
1.12	2.09	ND	ND	ND
1.00	2.07	ND	ND	ND
0.90	2.09	ND	ND	ND
0.80	2.00	ND	ND	ND
0.70	2.09	1.81	3.14	0.42
0.60	2.15	1.73	3.00	0.48
0.50	1.95	1.78	3.08	0.42
0.40	2.02	1.76	2.98	0.46
0.30	1.99	ND	ND	ND

ND = not determined

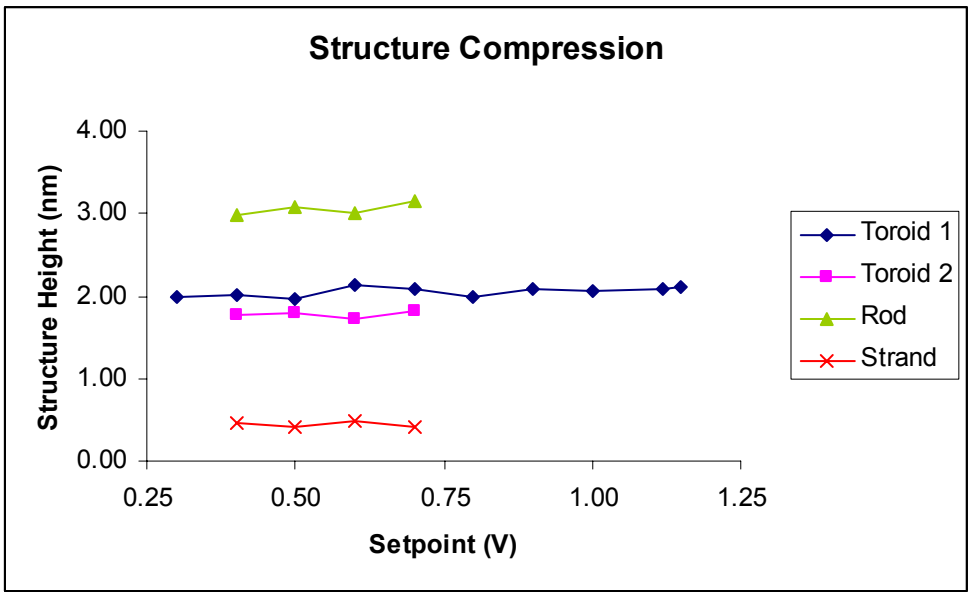

Figure 4.9 Plot of toroids, rod, and strand heights demonstrating no significant change with increasing contact force between the tip and sample using tapping mode AFM

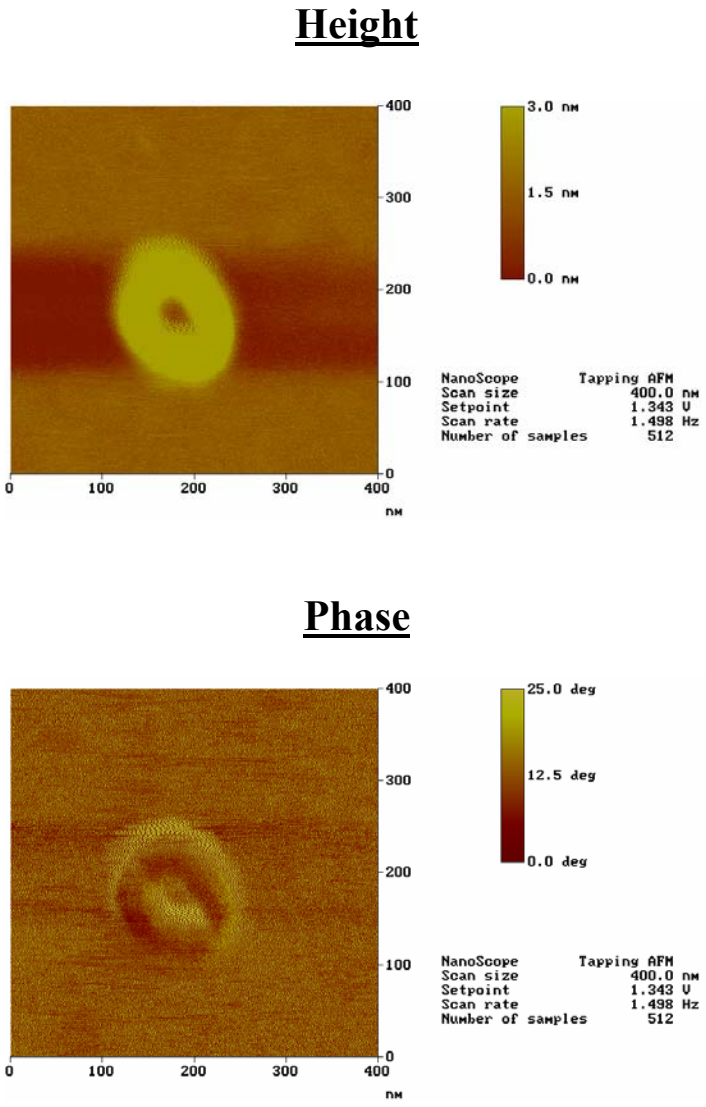

Figure 4.10 AFM tapping mode height and phase images of toroid using Hi'Res probe (slight multiple image due to small extratips) with sectional analysis height of 4.7 nm

Another key finding was that the repulsive regions of the force curves, both in contact and intermittent contact modes, had a slope of unity (Figure 4.11). This means that the movement of the scanner was proportional to the deflection of the cantilever which would not occur if compression or indentation were taking place (Figure 4.7).

These determinations along with the fact that the condensate structures are highly compact and not expected to be easily compressible and are under 30 atmospheres of pressure within a viral capsid [131], support the conclusion that the height measurements are accurate and not significantly reduced by compression.

The height of toroids induced with cobalt hexamine viewed from their edge has been shown with cryoelectron microscopy to have heights of approximately 50 nm [126]. This opens the question of whether the buffer-coated mica surface is involved in producing the oval cross-sectioned toroids seen in AFM samples in contrast to the toroids formed in solution for cryoEM.

Toroid Volume

The irregular dimensions of the toroids and rods made it unreasonable to calculate their volume or number of DNA strands per condensate structure. Some researchers have assumed a classical torus shape to calculate the volume, but we have shown that this is not valid based on the height and width differences. Others have used the packing fraction for hexagonal close packing of parallel cylinders [128], however, they also have made assumptions about the uniformity of the toroids.

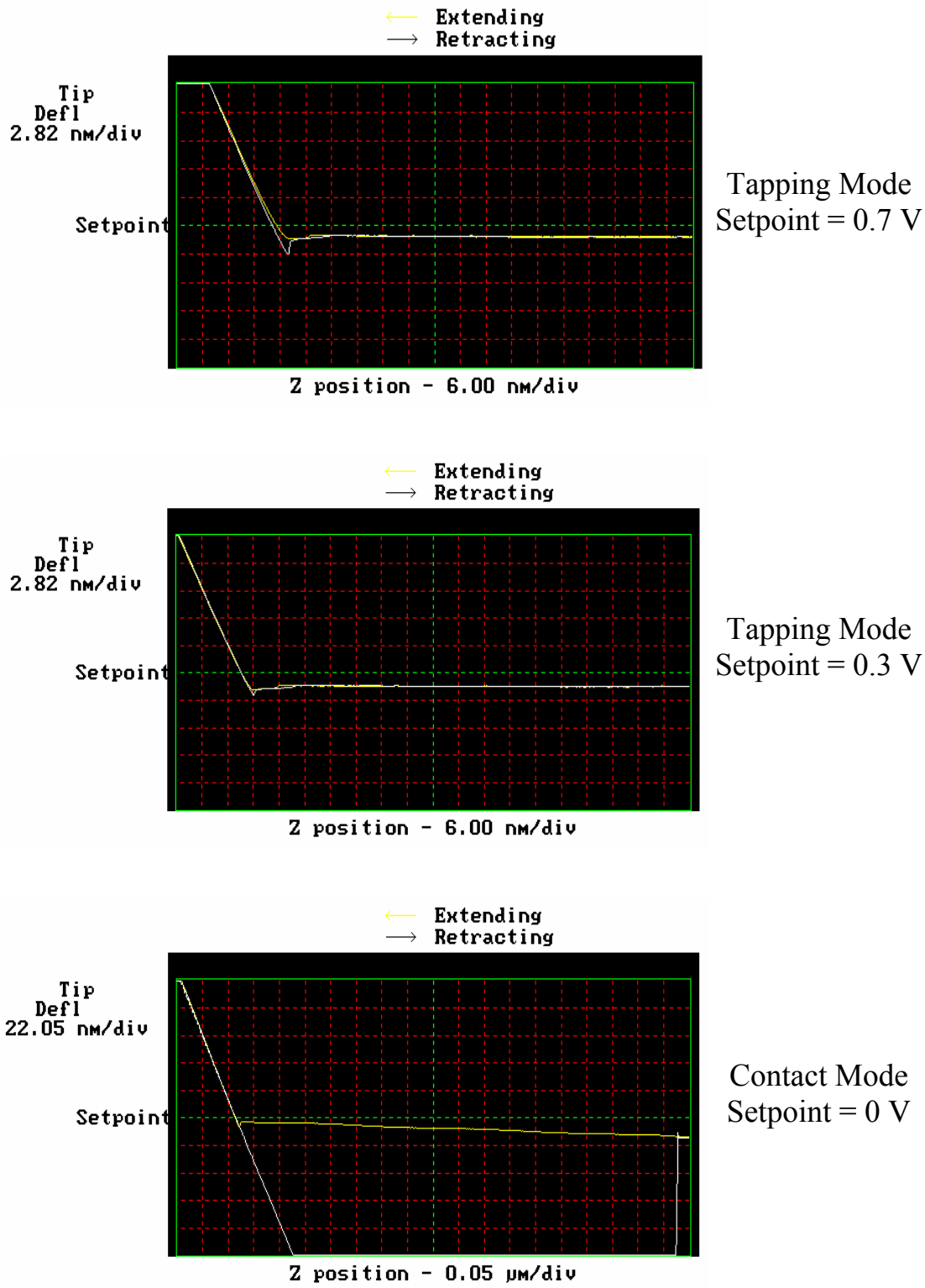

Figure 4.11 Force curves at increasing setpoints (related to tip/sample force and pressure) that maintain a slope of unity in the repulsive regime

It has been proposed that multiple small DNA molecules or a single large DNA molecule form a single toroid because toroids seem to have similar outer and inner diameter distributions regardless of the DNA length [121]. The outer diameter remained fairly constant, while toroid height was influenced by λ-DNA (48 kb) concentration in AFM studies conducted by Lin *et al*. [125] using spermidine. They observed what they described as multimolecular toroids formed with DNA concentrations between 1 and 10 ng/μL which had heights up to 60 nm (in increments of 11 nm), compared to monomolecular toroids with an average height of 17 $\pm$ 2 nm that formed at lower DNA concentrations around 1 ng/μL. Accordingly, it has been suggested that most toroids only consist of single DNA molecules until higher concentrations provide pressures to force multiple strands together for toroid formation.

Based on the literature summary (Table 4.2), it was noticed that there may be a relationship between the DNA length and the average toroid height (Figure 4.12), but there is insufficient evidence to draw a strong conclusion from this data because of the many other complicating variables involved in each of these experiments.

Condensate Structure Distribution

There is debate about the relationship between toroids and rods and the conditions that favor each morphology. The ratio of toroid to rod structures was found to increase from 1:2.2 to 1:1.6 with bis-NDI concentration (Table 4.5). Rods seem to predominate with nonpolar solvents, such as ethanol [132], or condensing agents, such as permethylated spermidine [133]. Rods are said to favor sharp local kinking due to lower free energy of

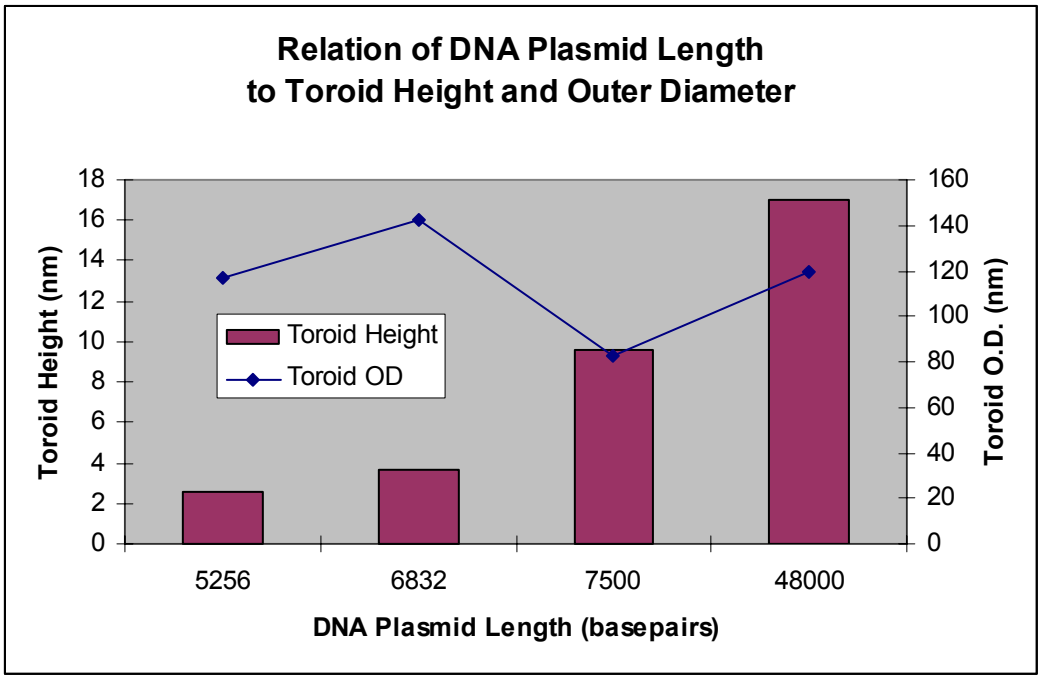

Figure 4.12 Relation of DNA plasmid length to toroid height (bars) and toroid outer diameter (line) based on literature values noted in Table 4.2

Table 4.5 Distribution of condensation structures formed with bis-NDI at 100 μM and 150 μM concentrations. The quantity of well defined condensate structures increased with higher bis-NDI concentration, for example the number of toroids doubles.

Structure	100 μM Bis-NDI	150 μM Bis-NDI
Toroid	6%	12%
Rod	13%	19%
Coiled Strand	27%	29%
Other	54%	40%

exposed hetrocyclic bases [132]. Spherical globules, which were also observed with the poly-NDI, become predominate with increased cobalt hexamine concentration which has been attributed to greater compressive forces [134].

The width of the poly-NDI toroids (outer radius to inner radius) averaged 55 to 32 nm and generally matched the width of the rods which averaged 34 and 31 nm formed with bis-NDI and tetra-NDI, respectively (Table 4.1). Other researchers also have found that the diameters and lengths of rods are similar to the thickness and circumference of toroids [135].

Condensation Process Theories

Several theories exist about the toroid formation process. These will briefly be discussed in light of the data obtained with poly-NDI condensation of pRS316.

A solenoid model has been proposed which purports that the DNA is wound like a string on a spool with the loops packed into a hexagonal lattice. Arguments against this model point out that crossover points between loops of different radii would have to be present [108]. Cryoelectron microscopy observations and modeling support regular hexagonal packing without crossover points [126].

A competing model has been proposed by Hud*, et al*. [108] which contends that DNA loops form a template for additional loops of DNA to accumulate to create a toroid structure. This has been supported by studies that demonstrated that the toroid size can be controlled by using DNA with engineered A-tract loops of varying diameters.

Other models have been proposed based on the potential relationship between toroids and rods in that the rod may bend around [136] or open up [86] to form a toroid. Arscott *et al*. have proposed that toroids are formed by circumferential winding of the DNA strand, while rods are formed by abrupt bending and kinking of the DNA strands [128].

AFM images acquired through these studies can be interpreted to support almost any of these theories depending on the viewpoint of the examiner; therefore, it does not seem practical to assign them as the basis for any particular model. There are images that show strands extending out of the toroids and rods (Figure 4.13a) which could imply a solenoid-like toroid formation model. There are images that show loops extending out of toroids and rods (Figure 4.13b) that could endorse the loop based formation models. Further, there are images with u-shaped and tennis racquet-shaped rods (Figure 4.13c) that could substantiate the rod bending models.

One could speculate the following progression of events for condensation based on the results reported. First, the divalent cations in the buffer allow the DNA to become more flexible due to electrostatic shielding. Then, the first poly-NDI ring intercalates into the DNA and the lysine groups further charge neutralize the DNA phosphate backbone. The second poly-NDI ring could then intercalate to stabilize loop structures. With further charge neutralization from increasing poly-NDI concentrations, the loops may collapse into rod structures. Finally, some of the rod structures bend into toroids.

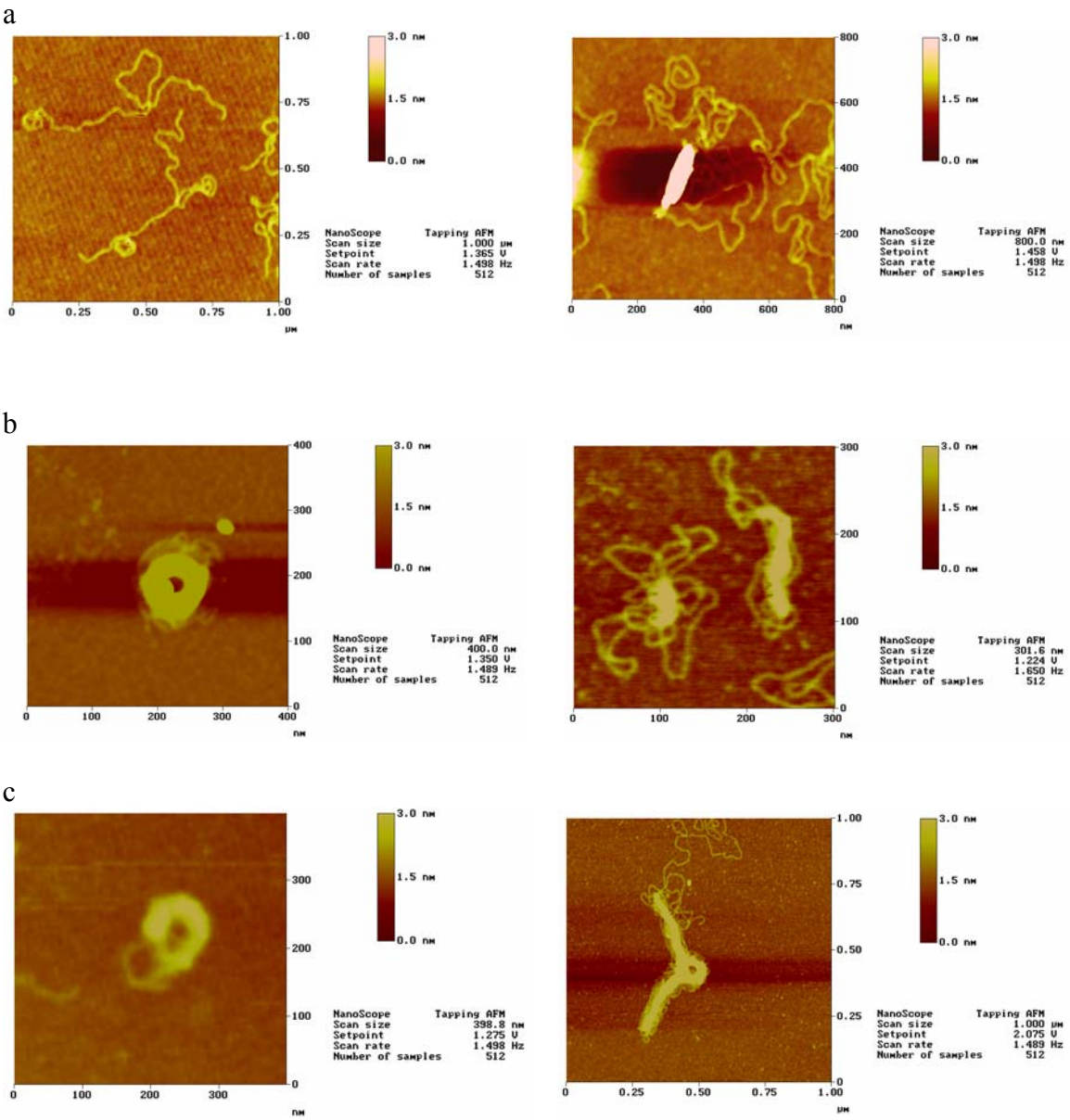

Figure 4.13 AFM images of condensation intermediates formed by pRS316 with poly-NDI a) toroids and strands with radiating strands, b) toroids and strand with radiating loops, and c) rods bending into pre-toroid-like structures

CHAPTER 5

COMMERCIAL APPLICATION AND VALUATION

Program Introduction

An assessment of commercial applications of this technology was made as a part of the TI:GER (Technological Innovation: Generating Economics Results) program. The TI:GER program was a joint program between the Georgia Institute of Technology and Emory University, funded by the National Science Foundation, and modeled after Purdue University's Innovation Realization Lab. It was a multidisciplinary program that brought together Georgia Tech Ph.D. students in science and engineering, Georgia Tech M.B.A. students, and Emory University law students. This program aimed to bring together the different students to focus on the interface of technical, management, legal, and economic issues involved in taking fundamental research into the marketplace.

The TI:GER program officially started in the Fall of 2002 with 21 members.
The program was recognized for its leadership in teaching entrepreneurship. Founder Dr. Marie Thursby and program director Alan Flury accepted the Price Institute Innovative Entrepreneurship Educators Award in 2003 on behalf of the program.

The central goal of program was to give student members a unique experience working first hand with the commercialization process for new technology. The multidisciplinary teams worked together to resolve real commercialization and intellectual property issues

and developed the skills to advance early-stage research into real market and business opportunities.

The research reported herein, investigating the use of Atomic Force Microscopy (AFM) to study drug and DNA interactions, was one of the first Ph.D. research areas chosen suitable for TI:GER. A TI:GER team to determine the commercial suitability of the technology was formed during the first semester of the program. The team was composed of two Ph.D. students (Elizabeth Gadsby, Benay Sager), two M.B.A. students (James Hutchinson and Brandon Walts), and a J.D. student (Kankindi Rwego, then Michael Kang).

Technology Definition

The technology was defined to be a novel application of the AFM for observing and analyzing the binding of compounds with DNA. AFM was demonstrated to allow direct imaging of DNA molecules and its interactions with drug compounds, including the binding location, twisting and kinking, and lengthening. The activity of the drug is often linked to the binding mode and resulting geometry. Thus, the potential activity of a drug could be assessed by detecting the DNA binding mode and fit of the drug candidate. By having specific knowledge about the interactions researchers could be better able to design new drugs. A trademark, DrugDock™, was selected to give a unique identity to the technology.

Proposed Uses

The DrugDock™ technology could be used to observe a broad variety of compounds interacting with DNA. The primary use that was proposed is a target validation tool for drug design. In addition, DrugDock™ could be used for drug screening through verification of the desired DNA-drug interactions. The method could also be applied to disease research to observe interactions of cellular compounds or viruses with DNA. Another possible application is in the field of environmental and ecological research investigating the effects of contaminants and other compounds on DNA.

Intellectual Property

The proposed technology to be known as DrugDock™ is an intangible process comprised mostly of a method for facilitating drug research, design, and screening. Intellectual property protection to support commercialization was studied. The TI:GER team explored the possibilities that the DrugDock™ method could be the subject of trade secret, patent, copyright, and trademark protection.

A trade secret would require that the technology or commercially valuable information be kept confidential. Trade secret protection would not be suitable in this situation because of public policy and the disclosure necessary for drug development. The Georgia Institute of Technology, as a public institution, has a responsibility to make its research available for the benefit of the community according to the Bayh-Dole Act. This public policy coupled with the reality of the Food and Drug Administration's stringent disclosure requirements for drug approval suggest that the method could only be used for its

intended purpose of drug development and design if the method and its results were publicly available.

Patent protection gives an inventor or patent assignee the right to prevent others from using, making, or selling the invention. According to 35 U.S.C §101, a drug design research method, such as DrugDock™, is a process that is eligible for patent protection in the United States. The DrugDock™ method most likely surpasses the law's minimal utility requirements. Patentability also depends on the novelty of the process. A patentability search was conducted in order to appraise the likelihood of patent protection. The results of patentability searches showed that the DrugDock™ technology has not been the subject of a patent. Broader searches surveying the landscape of AFM technology showed alternative uses of AFM.

Although patent protection is stronger than trade secret protection, it is only for a limited time. Patents typically endure for a term of twenty years after the application date. A provisional application does not require claims or examination, is fairly inexpensive, and provides protection for up to twelve months (35 U.S.C. §111(b)(2002)). According to the American Intellectual Property Law Association, law firms charged a median of $2,501 for provisional patent in 2000 [137]. During the twelve months of protection, DrugDock™ can be labeled "patent pending" thereby giving notice to others of the intent to file a patent application (35 U.S.C. §111(b)(2002)). An original non-provisional patent application on a relatively complex biotechnology or chemical invention has a median law firm price of $9,967. In addition, application amendment arguments for relatively

complex biotech/chemical patent applications have a median cost of $2,499. Considering that the PTO claims that a challenge-free patent application averages three years, applying for a patent in the United States alone is time consuming and expensive [137].

Based on discussions with the Georgia Tech Office of Technology Licensing (OTL), an invention disclosure was prepared. Georgia Tech OTL decided not to apply for patent coverage.

Copyright protection of original written documents is provided under 17 U.S.C. §102(a) (2002). Instructional manuals and promotional materials and articles describing the benefits of DrugDock™ could be copyrighted. There are a variety of media which could engender sources of copyright including internet web sites, academic journals, and advertisements in industry publications.

A trademark is a distinctive name that informs consumers of a single source for a product. It can be federally registered with the Patent and Trademark Office (PTO) under the U.S.C. §1051(Lanham Act§1)(b)(3)(2002). The TI:GER team brainstormed several potential names for the technology and selected the name DrugDock™ to represent the ability to investigate the "docking" of drugs into DNA and to provide a play on words of "doctor" since it is related to the pharmaceutical field. A search of the PTO database revealed that DrugDock™ was not registered, however DrugDoc, a mark for a bioinformatics software program, had been abandoned. The registration of the trademark

name DrugDock™ could distinguish this AFM method from other research tools and add reputation-related value to the technology.

Target Market

The primary market contemplated was pharmaceutical research and development (R&D). Pharmaceutical manufacturers, independent contract research laboratories, government research laboratories and academic research labs all perform R&D of new drug compounds for human use. Additionally, there are possible veterinary applications, though they are not typically as well-funded as drugs for human use. Other research applications might be in medical disease or environmental effects laboratories.

The pharmaceutical market is huge, and growing. Worldwide sales of pharmaceutical products topped $400 billion in 2002, about a 9% increase over the previous year's sales. To support this level of activity, $63 billion was spent on research and development. Of this amount, $2.5 billion was spent by the largest 18 companies on gene-related drugs (amounting to 5% of their total R&D expenditure) while $1.5 billion was spent on high-throughput drug screening products, technologies and services [138]. As the rate of R&D expenditure rises and the rate of new drug approval falls, the pharmaceutical industry searches for ways to increase its efficiency in drug discovery and development (Figure 5.1).

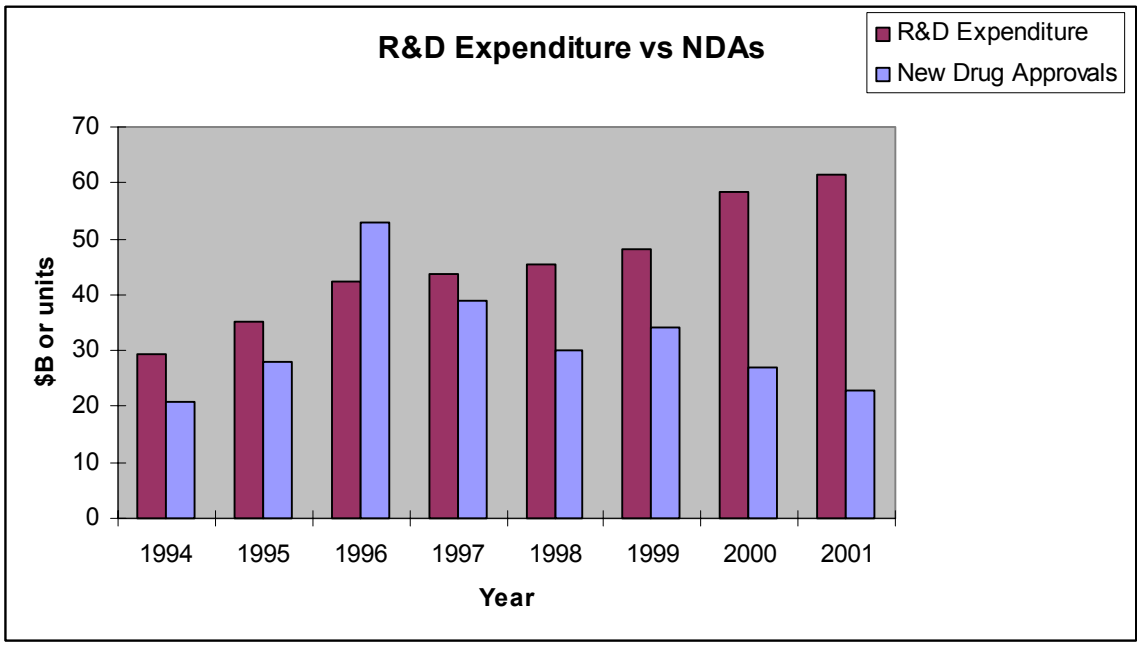

Source: Amersham Biosciences Annual Report 2002, PhRMA

Figure 5.1 Trends in worldwide R&D expenditure ($ billions) versus U.S. FDA new drug approvals

The rewards for the successful pharmaceutical manufacturer are huge, as well. A drug is considered a "blockbuster" when its sales reach $1 billion per year, a level that 44 drugs sold in the United States had reached by 2000. Such sales levels are needed with the average capitalized cost per marketed drug reaching an estimated $802 million over the 8 to 12-year discovery and development process. An estimated 7 of 10 drugs never sell enough to justify the investment in their development.

Tufts University's Center for the Study of Drug Design (CSDD) claims that 93.3% of 284 new drugs approved in the U.S. in the decade 1990 to 1999 originated in industry labs, with 3.2% in government labs and 3.5% in academic and other non-profit labs. CSDD estimates that 30% of R&D monies are spent in the preclinical phase. The preclinical cost of bringing a new drug to market is estimated at $121 million of expenditure, which is equivalent to $335 million when the time value of money is considered, and is growing at 7.6% per year. For every 5,000 compounds considered, only five proceed to a clinical test phase, and only one reaches the market.

R&D executives are seeking ways to improve the efficiency of the discovery and development process, and pharmaceutical industry executives are emphasizing the development of drugs for chronic diseases to maximize the likely return on their investment. These trends are good news for DrugDock™ which is expected to lead to quicker, better-informed decisions in the drug discovery and screening process.

The market may be segmented in many different ways. One obvious way would be to divide the revenues into those produced by patented drugs and those whose patents have expired, usually known as generics. As may be expected, the profit margins are much wider for patented drugs than for the generics, as the producing companies try to pay for the considerable effort that is expended in bringing a new drug to market. DrugDock™ is expected to be of value in bringing new drugs to market, and, therefore, is not likely to be applicable to the generic market. Another segmentation method is to divide the market into prescription and over-the-counter (OTC) drugs. Since DrugDock™ is expected to be of value in a relatively new area of treatment, it is expected that the OTC market is not applicable in this analysis. Another way to segment the market would be by the action that the drug takes to defeat the targeted malady. There are numerous mechanisms and given that the mechanism of targeting DNA with drugs to prevent disease is expected to be particularly suited to the treatment of some of the most intractable problems in the medical world such as cancer, the potential is great. Sales of cancer treatment drugs dominated the sales of drugs new on the market in 2002 at about two thirds of $156 million.

Competition

The competition is considered to be the current methods of target validation, although the possibility of parallel development of a similar technology must not be discounted in this new and expanding field. Current methods utilize general analytical laboratory instruments such as NMR and X-ray crystallography to visualize DNA. Both of these methods have major drawbacks in that they require significant sample preparation, they

average the results of a large number of molecules, and data interpretation is much more challenging.

X-ray crystallography requires a large sample of pure crystalline material that is difficult to obtain from larger molecules. This limitation prevents the evaluation of the compounds in their natural state which would likely effect activity. NMR can be conducted in liquid state, similar to physiological conditions. However, NMR requires a moderately large sample size (millimolar range) which is difficult with relatively insoluble compounds. Long data collection times are necessary to overcome this sensitivity limit using a pulse sequence design. In addition, NMR has limited resolution, especially for larger molecules (greater than 25 kDa).

Commercial Venture Options

There were several business venture formats that were considered for the commercialization of the technology. First, the inventors could start their own company to test, design, and research clients' drugs and/or compounds on a fee basis. Second, AFM manufacturers could license the method to make their product more salable to their current customer base and potentially widen the market for atomic force microscopes. Third, individual pharmaceutical firms could license the technology to characterize DNA-drug binding interactions while developing their product to provide a competitive advantage. Fourth, analytical service bureaus catering to the pharmaceutical industry could license the method to expand their portfolio of R&D services.

Operations

It was considered that operating a laboratory requires significant start-up costs: a substantial capital investment, expensive specialized labor, and possibly official certification to satisfy regulatory constraints. Laboratories already in the market offer a variety of services to the industry. A "one-trick pony" laboratory would not be likely to successfully compete in this environment, even with patent protection, unless the value added by the technology is exceptional. Therefore, the licensing business venture options are indicated.

The technology product is entirely in the area of intellectual property in the combination and proper use of instruments and components produced by other parties. The AFM instrument used is purchased on the market and used unmodified, and the drugs and DNA used are similarly sourced externally. A manual or other training materials would add value to the transfer of the technology. Possibly a limited amount of consulting or support services could also be arranged. Therefore, the operations that derive revenue from the DrugDock™ technology are associated almost entirely with the marketing of it.

Marketing

DrugDock™ is a quite specialized technology. A broadcast marketing campaign is not necessary, and several suitable vehicles exist for alerting the community of possible users. The pharmaceutical industry has a number of journals, magazines, and organizations to serve it. Publication of the research results in one or more peer-reviewed journals will alert the community to the existence of the technology. An advertisement in

an industry magazine timed to coincide with research publication would reach an audience of the more business-related side of the industry, and would generate a second channel of demand pull as well as instigate intra-company conversation about the technology. Another channel for raising awareness of the availability of the technology is the Internet. A polished-looking, informative website is a must in the information age

It is possible to contact a large portion of the target market of pharmaceutical R&D labs directly. A brochure extolling the benefits of DrugDock™ can be placed in the hands of decision-makers in this way. The key companies are readily identified through the website of the Pharmaceutical Research and Manufacturers Association of America at www.phrma.org. Collaboration with AFM manufacturers (Table 1.1) could be pursued as well. They may be in possession of customer lists outside of the pharmaceutical research industry who may nevertheless be interested in licensing DrugDock™ technology. An incentive to the AFM manufacturers for cooperation in this matter could be increased sales of their instruments to customers interested in the new application.

Roadblocks and Risks

Every new technology faces a variety of roadblocks or risks as it is developed toward marketability, and DrugDock™ is no exception. The risks considered are developmental risk, operational risk, market risk, and competitive risk.

Developmental Risk

Developmental risks are the risks encountered in proceeding from theory to practice. Every new technology faces unpredictable challenges in its development. The risks of failure or delay are higher when developing something completely new or when extending the limits of a technology than when developing procedures that are within the capability of a technology. The latter is the case for DrugDock™ for which the concept has been proven in the laboratory and the milestones for further development do not represent large technological leaps forward, but rather application of accepted laboratory practices to optimize the operation of the AFM. The valuable product that is the DrugDock™ technology is intellectual property, and the outlook for obtaining the necessary patent is good.

Operational Risk

Operational risks are the risks encountered in the production of the revenue-producing product. In general these might include risks from other segments of the value chain, risks from the acquisition and maintenance of plant and property, risks involved in and risks involved in manufacturing the product or providing the service, and risks in delivering the product or service to the customer. The operations risks for DrugDock™ are low. Such a concept of operations for commercialization leads to a high-fixed-cost business model, such as for software, music, or other products consisting primarily or solely of intellectual property. The marginal cost in producing more revenue by licensing to additional customers is expected to be low.

Market Risk

Market risks are those involved in producing a customer perception of value in the product. Such risks might include the risk of technological obsolescence or the risk that a competitive product might be preferred, perhaps due to a different performance profile or lower price. While the ability to investigate the binding mode of compounds with DNA is expected to result in a benefit of reduced money and time spent in the preclinical R&D phase, the amount of this benefit is as yet un-quantified. The risk of not being sufficiently valued by customers to produce profits must be considered moderate. The risk of low demand can also be derived from other factors. For instance, growth in the DNA-targeted drug market may be low.

Competitive Risk

There is a competitive risk of parallel development of a substantially similar technology. The AFM instrument itself is fairly new, and further uses for it and achievements with it are regularly reported in the literature. Another competitive risk is the possibility that the advantages afforded by AFM technology is not significantly valued above the current methods of NMR and X-ray crystallography, even with their drawbacks. Finally, there is some concern expressed in public forums regarding the enforcement of process patents. Even though the ability to draft a patent with broad protections might give a level of confidence that infringement is unlikely, the globally-distributed nature of the pharmaceutical industry, the proprietary nature of research laboratories and the uneven application of legislated intellectual property protections must be considered a risk.

Valuation

Many decisions made in the development of a technology are contingent on its potential value in the market, making valuation one of the earliest and most important tasks in the innovation process. Valuation drives or contributes information for decisions such as whether to devise a business strategy based on licensing or starting a venture business organization and the type of intellectual property (IP) protection to seek. Valuation entails understanding the "pain" in a market and how the technology might be of value in alleviating it.

The value of DrugDock™ is not a single number. Rather, it is a range of values produced by different methods. Many assumptions go into any valuation, since it is an attempt to discover something that is unknown. This valuation contains more assumptions than most, produced as it was made with limited connections to the industry, dealt with an industry that does not share information about specific costs, and concerns a new technology which may be disruptive in nature.

There were multiple challenges in attempting to value DrugDock™. Foremost among them was the dearth of solid information available about the pharmaceutical R&D decision process. The difficulty of making decisions regarding which potential drug compounds to pursue was the subject of many publications in both the industry press and in academic journals. Many competing theories were promoted as providing the best support for making decisions in the face of tremendous uncertainty. In addition, the real

costs involved in R&D were not often shared by firms in this very competitive industry. Appearing either too proficient or too inefficient could attract attention from potential acquiring companies. Aggregate data was available from some academic sources and industry associations, but its applicability to any particular firm was questionable given the wide range of sizes and capabilities of firms in the industry.

Net Present Value / Discounted Cash Flow

This standard valuation method involves projecting a series of cash flows into the future for a reasonable number of periods, assuming a terminal value based upon a fixed growth rate, and discounting all the cash flows back to the initial period. Strengths of this method include its transparency and simplicity, but it is notoriously inflexible. Still, other methods like Adjusted Present Value, Expected Net Present Value (NPV), and real options analysis only add value when there are events that are likely to occur, and outcomes that are known to a reasonable probability. Such a level of detail is overkill for such an early-stage technology, the future of which is so nebulous.

The keys to NPV analysis for DrugDock™ are in the choice of cash flow and growth rate, and to a lesser degree discount rate. The cost of capital will vary somewhat according to the firm, but a sensitivity analysis can show the range of possibilities. Continuing in reverse order, the growth rate may be assumed by assessing the industry's desire for the product. Since the pharmaceutical R&D industry is actively seeking ways to improve efficiency and DrugDock™ offers just that, a relatively higher rate of growth may be assumed. Indication of the possibility of cash flow would flow from unit price

times units sold, but that analysis has not been done for DrugDock™. A more general way would be to assess the time value savings that DrugDock™ might provide and estimate what proportion of that savings that might be charged for its use.

The CSDD estimates that $121 million is spent per approved new drug in the preclinical phase, where DrugDock™ is expected to be of use. That money is spent winnowing five thousand candidates down to the five that will enter the clinical phases for each new drug to reach the market. Of course, some compounds are eliminated early in the process (estimated to take 52 months) and others later, but assuming the average yields $24,200 per compound. Assuming the average compound makes it to the midway point, it is under consideration for 26 months, meaning that about $930 per compound per month is spent. Information from a pharmaceutical industry executive indicates that it takes from $100,000 to $300,000 per year to employ and equip a researcher (the so-called Full Time Equivalent, or FTE cost). Again taking the average, and assuming a 50-week year, an FTE is $4,000 per month, so a researcher can handle about 4.3 compounds per month on average. If DrugDock™ can provide a 10% reduction in the time it takes to evaluate a compound, then an FTE could handle 4.8 compounds per month. The 52 months become 46.8, and a savings of $12.19 million is realized without considering the time value of money back to the initial period. A 5% time savings similarly yields a $6.145 million savings by the time an investigational new drug reaches clinical testing. Assuming an average of 2 years to reach the savings and a 12% cost of capital those figures are $9.7 million and $4.9 million, respectively.

Not every compound will be suitable for screening with DrugDock™, so assuming it will only be used to screen 10% of compound candidates, and 10% of the potential cost savings can be wrought from the industry, one percent of $49 million (to use the lower time savings estimate, times 10 per year) is $490,000 per year.

Alternatively, the average of the two new cancer drugs Eloxatin and Faslodex, $75.6 million and $23.6 million respectively, can be used to make another estimate. Assuming the average level of sales of $49.6 million is reached in year 12 currently, the value of reaching the market 6 months earlier (reflecting a bit better than a 10% reduction in pre-clinical discovery time) would be $24.8 million (6 months' sales) divided by the factor of $1.12^{11.5}$, or 3.6814. This yields a value of $6.74 million.

For the range of potential values ($490k, $674k, and $970k) of full market penetration, assume first year sales of 5%, then a series three years doubling sales each year, then a series of more moderate growth (20% annually) for four more years, then growth thereafter only with the economy.

Comparable Analysis

Many new technologies follow similar trajectories in their growth and adoption by the marketplace. The key is to choose as models technologies that are comparable in appropriate ways. DrugDock™ will compete in an interesting environment. The techniques currently used to image DNA and to evaluate binding of compounds to DNA are general laboratory techniques performed with more-or-less general laboratory

instruments, some of which are much more expensive than a $120,000 AFM, some of which are much less. The capital expenditure will be acceptable to the largest labs, but as with other expensive and perhaps specialized technologies, DrugDock™ is expected to be attractive to service bureaus that can invest in the equipment and then take in a sufficient volume of work from many smaller labs, those that lack the requirement for full-time access to such technology, in order to make the investment pay off.

Identifying a comparable technology is difficult, and finding sales and use information is more so. The existence of an industry selling market reports for nearly $4,000 a copy is an indicator of the magnitude of the task. However, a quite comparable technology that is popular enough to appear in some detail in the industry press is Polymerase Chain Reaction (PCR). PCR does not accomplish the same task as DrugDock™, however, it is sold to a similar market and it has exhibited a strong intellectual property protection plan from the start which has created value for its developers.

PCR was invented in the 1980's in California by Nobel Prize winner Kary Mullis and developed by Cetus Corporation. The process involved repeated heating of a solution containing a particular enzyme that promoted the reproduction of copies of subject DNA. The process and the solution were patented, and Cetus licensed to Perkin Elmer the production of an instrument designed to perform the cyclic heating of the solution. From 1987 to 1990, the sales of the thermocycler increased at a CAGR of 123.5%. Cetus received approximately 15% of sales from Perkin Elmer as payment. Cetus then sold the rights to PCR in 1991 to Hoffmann-La Roche, which continued the license arrangement

with Perkin Elmer, which collected a $10,000 license fee with the sale of each thermocycler. In addition, Hoffmann-La Roche sold kits containing the solution with the enzyme and licensed production of the solution in return for a 15% royalty. By 1997 the total business in the PCR technology was reported at $300 million annually, which represents a CAGR of 41.63%.

Certainly the continued success of PCR is remarkable, and it is not reasonable to assume such success for DrugDock™. PCR is much more widely applicable, producing as it does the raw material for other DNA lab work, while DrugDock™ is a tool for analysis. PCR is widely used in research labs and in diagnostic work as well. We could use PCR as a model by assuming only a tiny fraction of its sales, one tenth of one percent, and assuming a conservative growth rate.

Venture Capital Analysis

Venture capitalists (VC) are in a risk-laden business. They follow a portfolio approach in attempting to reduce risk to the minimum by diversifying their investments in the nearly-sure knowledge that some of the companies in which they invest funds will provide no return. The hope is that through judicious choice of the teams and technologies one or more of the young businesses will succeed handsomely, with a many-fold payback of the investment at the end of the time horizon. To this end, VC's use a harsh discount rate.

Beginning with an estimate of the worth of the firm at the end of the investment horizon, they calculate NPV using discount rates in the neighborhood of 50%. This will normally

produce a valuation much lower than the other methods, which is a reflection of the risk being undertaken by the investors. A range of discount rates, from 45% to 60%, and a range of future values based upon different growth rate assumptions from a very low growth rate of 2% to a supernormal growth rate of 8% was used to produce a matrix of possible values. The projected required return rate was adjusted upward to account for the higher expectation of risk. A net cash flow assumption of 15% of the sales expected in 5 years was used. Assuming the middle value from the DCF cash flow analysis of $674,000 and using a recent average 5-year risk-free rate, about 5%, to project about $820,000 in sales. Net cash flow of 15% is roughly $123,000 per year.

Using various methods, DrugDock™ is estimated to have a value between $69,000 and $5.4 million at its current, early stage of development, depending the estimation of risk and on the forecasts for growth of sales, the market and the economy. These numbers indicate that Georgia Tech's Office of Technology Licensing should seriously pursue marketing opportunities for DrugDock™.

CHAPTER 6

FUTURE RESEARCH

Many new questions have arisen and paths to pursue discovered based on the novel findings of the research reported herein. A few of the key suggestions are outlined for the consideration of future researchers. They focus on gaining a better understanding of the DNA/drug interaction and DNA condensation process by exploring the impact of the DNA length and sequence, the role of the polyintercalator linker, and the influence of the preparation conditions. Experiments to test some of the hypotheses set forth in this dissertation are also proposed.

DNA Length and Sequence

The studies in this dissertation focused on the pRS316 linearized DNA plasmid with a length of 4,887 basepairs. This plasmid was selected based on its length being sufficiently long enough to allow significant lengthening with intercalation to increase the signal to noise ratio, yet short enough to allow some of the strands to lie on the surface with minimal crossovers. Because DNA with short lengths, less than 400 bp, are not able to form condensate structures [102], they would be useful for observing bending in a manner similar to that done by Berge *et al*. with luzopeptin [82]. Experiments with short linear DNA strands could help elucidate if intermolecular interactions are occurring as suggested in the model in Figure 3.20.

It was noted from the literature survey summary in Table 4.2 and Figure 4.12 that there appears to be a potential link between the DNA plasmid size and the thickness of the toroid as measured by AFM. However, there were numerous other complicating variables in these studies. For that reason, it would be worthwhile to conduct a controlled study observing toroids formed by various lengths of similar DNA sequences with a uniform drug to DNA basepair concentration.

Additionally, it would provide insight to observe the interactions of the poly-NDI with DNA molecules composed of different GC to AT ratios which may lead to condensation at lower concentrations or at different ratios of toroid to rod structures. DNA containing specific sequences such as A-tracts may also impact condensation. A-tracts were used by Hud's group to cause curvature to produce static loops in the DNA and theoretically serve as templates for toroid formation [108].

It would be interesting to explore the effect of poly-NDI on chromatin condensation compared to naked DNA. Chromatin is the nucleoprotein complex of DNA with histone proteins and related proteins found in higher order cells. Sen and Crothers studied the impact of magnesium ions and bis-intercalators with a 3+ charge on chromatin condensation [139]. It would be revealing to determine if the lesser charged poly-NDI which has been shown to be capable of condensing naked DNA has a similar effect on chromatin DNA.

DNA Binding Ligands

Other suggestions for future research are directed toward variations of the DNA binding compound, such as modifications of the polyintercalator compound or compounds with different binding modes. Investigation of the ability of other related poly-NDI compounds created from the combinatorial library [62] would allow analysis of the role of the linker sequence. It has been proposed that the lysine in the linker is responsible for charge neutralization of the DNA backbone resulting in its condensation. This concept would generally by supported by the ability to produce similar condensation reactions with other poly-NDI compounds containing a lysine or other positively charged amino acid in the linker. The impact of the location of the lysine or positively charged amino acid in the linker would help further in the understanding of the role of the linker sequence.

The poly-NDI molecules studied in this research were found not to be sequence specific, but other related poly-NDI molecules were sequence specific which allowed their structure to be resolved using NMR. Specifically, a poly-NDI with a linker sequence of Gly-Gly-Gly-Lys has been shown to have the linker bind in the major groove [67], versus the compound with a linker sequence of Ala-Ala-Ala-Lys that the linker binds in the minor groove [68]. A comparison of these two compounds may reveal the effect of the linker position relative to the DNA grooves.

The rigidity of the linker likely has an important impact on the mode of DNA interactions. It is anticipated that a very rigid linker that positions the intercalator

moieties in parallel would help differentiate between the sequential intercalation model (Figure 3.18) and the intrastrand intercalation model (Figure 4.20). The rigidity of the linker may also affect the ability of the DNA/ligand complex to bend and form condensate structures.

Exploration of other poly-intercalators and their linker structure would expand the understanding of the role of intercalation in condensation. Initial studies were conducted using the mono-intercalator, ethidium bromide (EtBr), and the bis-intercalator, ethidium homodimer (EtDi) (Figure 6.1). Lengthening was observed with the ethidum bromide which confirmed intercalation, but no significant secondary structures arose with increasing EtBr concentration (Figure 6.2). The preliminary data revealed greater looping structures and a few small condensate intermediate-like structures at higher ethidium homodimer concentrations (Figure 6.3). A molecule with a single ethidium ring and the linker is being synthesized in Bottomley's lab following the procedure outlined by Benson *et al*. [140]. A comparison of the effects of the single ethidium with the linker with the mono-intercalator and the bis-intercalator will be evidence for the role of the linker in forming secondary structures. A further comparison could be made with the commercially available heterodimer of ethidium and acridine intercalators with the same linker structure.

A similar study with the mono-intercalator of NDI and the mono-NDI with the Lys-Gly-Gly-Gly linker would help differentiate between the role of the intercalating ring moiety and the linker assembly. This could serve to support or oppose the model purporting the

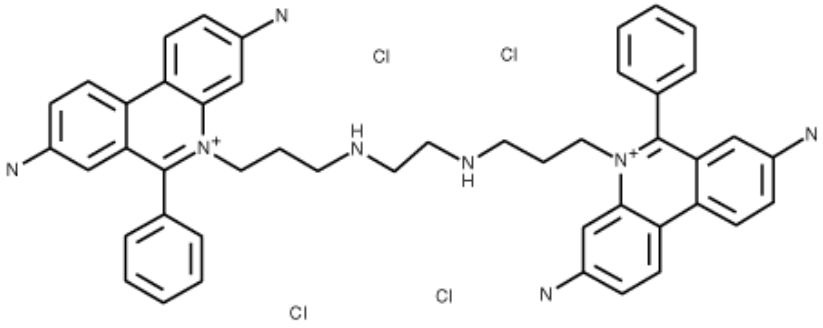

Figure 6.1 Chemical structure of ethidium homodimer-- a bis-intercalator composed of one of the most commonly used intercalators, ethidium, linked by a polyamine similar to spermine, a classical condensing agent

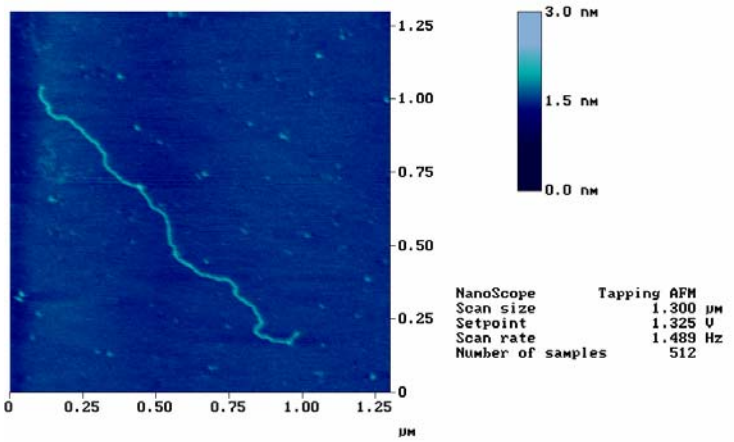

Figure 6.2 Representative AFM image of pRS316 with 1.0 µM ethidium bromide on mica illustrating strand lengthening due to intercalation, but no significant change in secondary structure

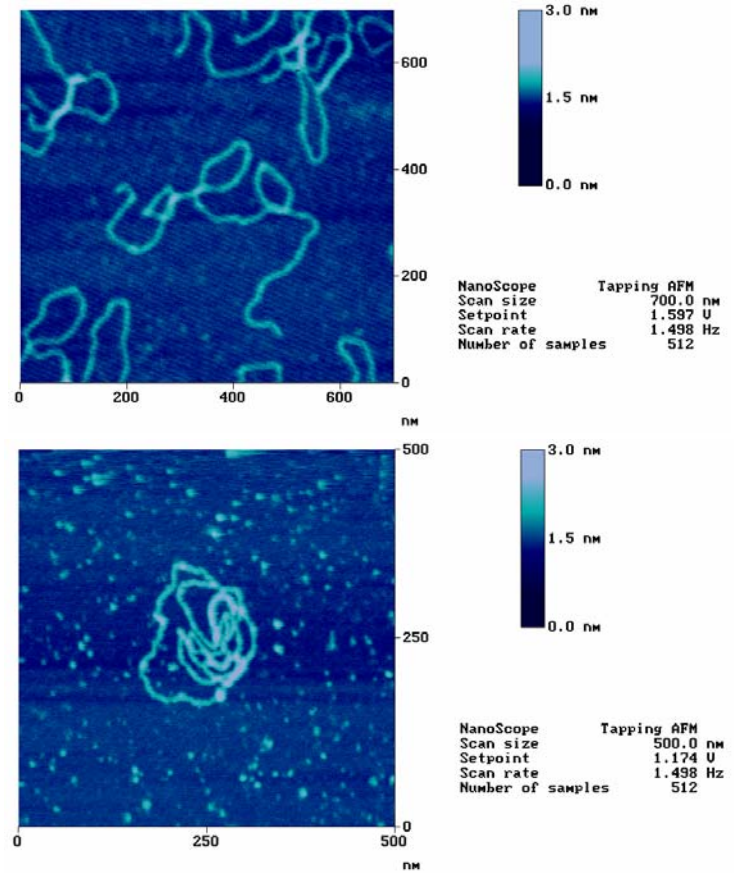

Figure 6.3 AFM images of pRS316 with 0.1 and 0.15 µM ethidium homodimer on mica showing secondary structure formation

involvement of multiple intercalation points on distant regions of the same or different DNA strands to form loop structures or stabilize multi-strand condensates (Figure 3.20). It is expected that the mono-NDI alone would not lead to DNA condensation based on its DNAse footprint (Figure 3.14).

Experiments using compounds known to utilize other DNA binding modes such as groove binding with high concentrations and similar charge intensities could indicate the function of intercalation versus charge neutralization in causing condensation.

Influence of Cations

Magnesium chloride (MgCl) was used in the buffer to generate electrostatic binding of the DNA to the mica surface during sample preparation in the studies reported in this dissertation. It is recognized that the magnesium ion may have an influence on the DNA conformation and the interactions between the poly-NDI and the DNA. Controls were run that confirmed that the buffer alone did not change the secondary structure of the DNA. Others' experiments have also determined that divalent cations, such as Mg^{+2}, are unable to induce DNA condensation [107].

However, these cations may facilitate condensation based on their ability to increase DNA flexibility, bending, and conformational changes [103-105]. Specifically, magnesium cations have been shown to have an effect on the size of toroids based on research with hexamine cobalt as the condensing agent [71]. Studies to probe the function

of the MgCl should include the use of other monovalent and divalent cations in the preparation buffer at various levels.

Intermediate Condensation Structures

Interesting secondary structures, described as loops and flowers were imaged in addition to the completely formed condensate structures of toroids, rods, and spheres. The progression of the formation of these structures was consistent for the bis-, tris-, and tetra-NDI molecules in relation to their increase in concentration. Recurrence of this pattern in the studies proposed above with various DNA sequences, different poly-intercalators or other DNA binding ligands would provide strong support that these are intermediate structures in the condensation pathway.

Ultimately, this work and expansion upon it may lead to a better understanding of DNA condensation which can be applied to gene delivery systems and anti-viral agents. It may also help direct the development of better drugs based on the insight of poly-intercalators interactions with DNA.

APPENDIX A: pRS316 DNA SEQUENCE

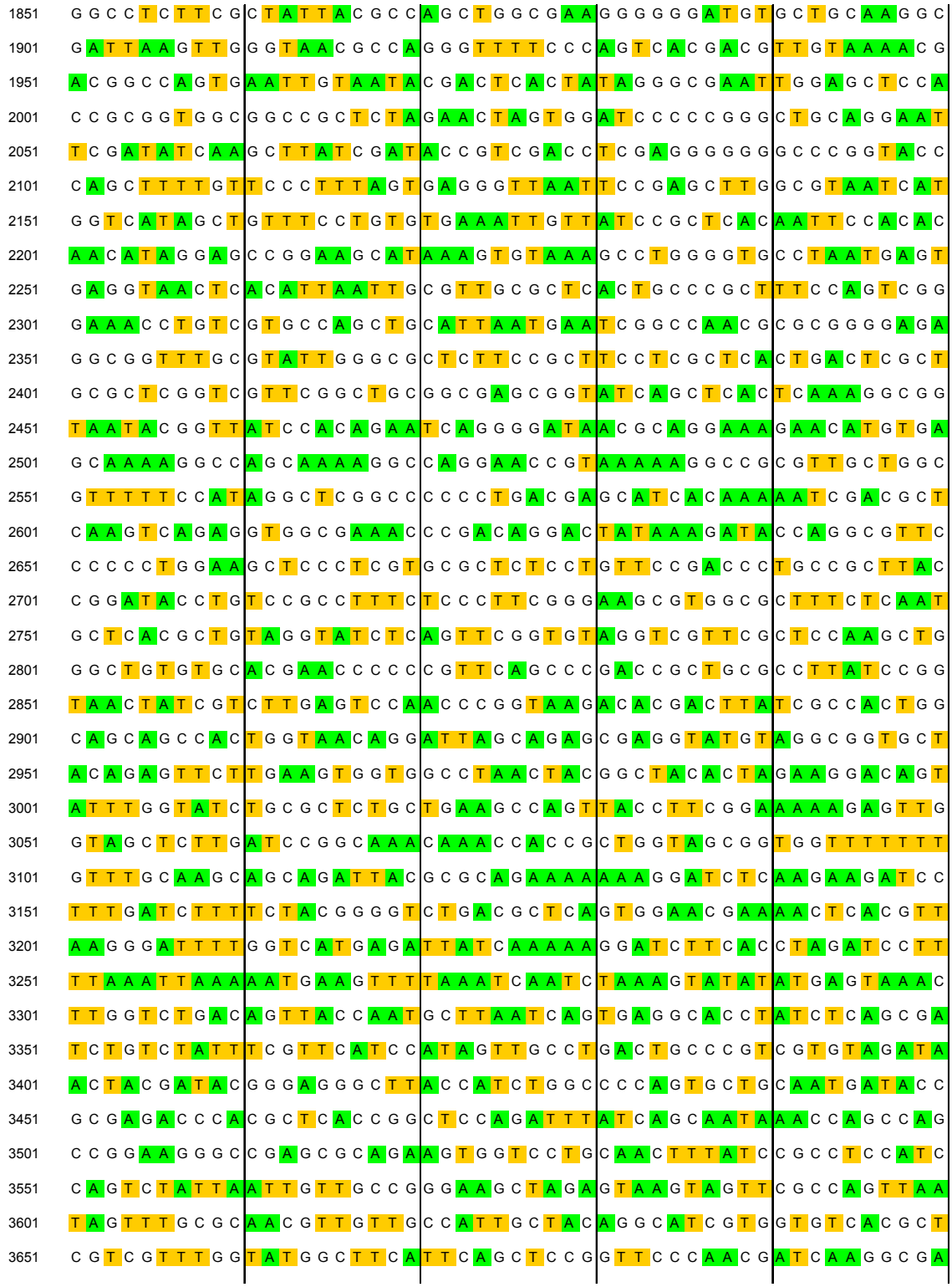

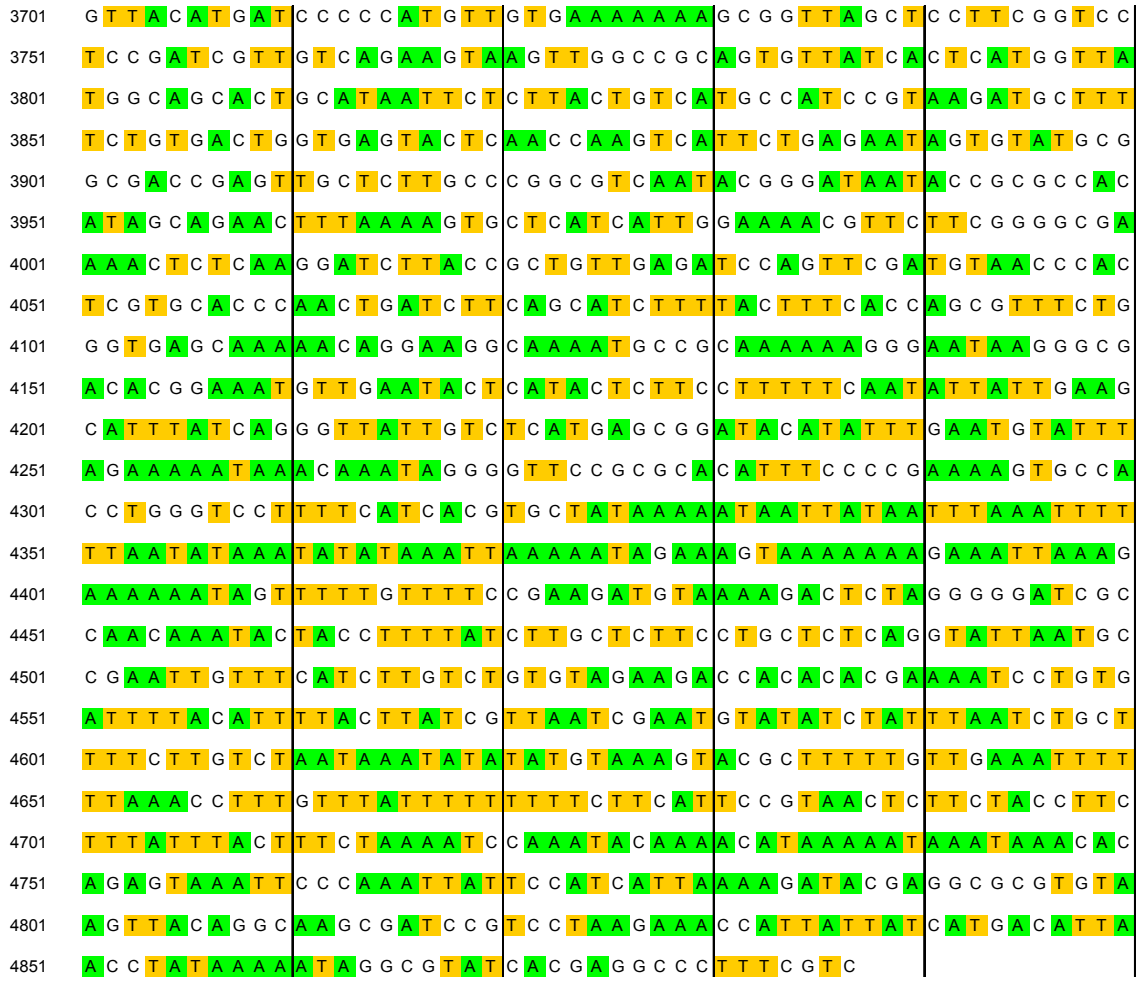
3701 GTTACATGATCCCCCATGTTGTGAAAAAAAGCGGTTAGCTCCTTCGGTCC
3751 TCCGATCGTTGTCAGAAGTAAGTTGGCCGCAGTGTTATCACTCATGGTTA
3801 TGGCAGCACTGCATAATTCTCTTACTGTCATGCCATCCGTAAGATGCTTT
3851 TCTGTGACTGGTGAGTACTCAACCAAGTCATTCTGAGAATAGTGTATGCG
3901 GCGACCGAGTTGCTCTTGCCCGGCGTCAATACGGGATAATACCGCGCCAC
3951 ATAGCAGAACTTTAAAAGTGCTCATCATTGGAAAACGTTCTTCGGGGCGA
4001 AAACTCTCAAGGATCTTACCGCTGTTGAGATCCAGTTCGATGTAACCCAC
4051 TCGTGCACCCAACTGATCTTCAGCATCTTTTACTTTCACCAGCGTTTCTG
4101 GGTGAGCAAAAACAGGAAGGCAAAATGCCGCAAAAAAGGGAATAAGGGCG
4151 ACACGGAAATGTTGAATACTCATACTCTTCCTTTTTCAATATTATTGAAG
4201 CATTTATCAGGGTTATTGTCTCATGAGCGGATACATATTTGAATGTATTT
4251 AGAAAAATAAACAAATAGGGGTTCCGCGCACATTTCCCCGAAAAGTGCCA
4301 CCTGGGTCCTTTTCATCACGTGCTATAAAAATAATTATAATTTAAATTTT
4351 TTAATATAAATATATAAATTAAAAAATAGAAAGTAAAAAAAAGAAATTAAAG
4401 AAAAAATAGTTTTTGTTTTCCGAAGATGTAAAAGACTCTAGGGGGATCGC
4451 CAACAAATACTACCTTTTTATCTTGCTCTTCCTGCTCTCAGGTATTAATGC
4501 CGAATTGTTTCATCTTGTCTGTGTAGAAGACCACACACGAAAATCCTGTG
4551 ATTTTACATTTTACTTATCGTTAATCGAATGTATATCTATTTAATCTGCT
4601 TTTCTTGTCTAAATAAATATATATGTAAAGTACGCTTTTTGTTGAAATTTT
4651 TTAAAACCTTTGTTTATTTTTTTTTTCTTCATTCCGTAACTCTTCTACCTTC
4701 TTTATTTACTTTCTAAAAATCCAAATACAAACATAAAAATAAATAAACAC
4751 AGAGTAAATTCCCAAATTATTCCATCATTAAAGATACGAGGCGCGTGTA
4801 AGTTACAGGCAAGCGATCCGTCCTAAGAAACCATTATTATCATGACATTA
4851 ACCTATAAAAATAGGCGTATCACGAGGCCCTTTCGTC

APPENDIX B: DERIVATION OF DNA INTERCALATION THEORETICAL LENGTHENING EQUATION

Definition of terms (units)
K = Binding affinity (M^{-1})
Lo = Length of un-intercalated DNA (nm)
L = Length of intercalated DNA (nm)
D = DNA concentration- total (M)
B = Basepairs per DNA (bp)
a = Lengthening per intercalation event (nm)
n = Exclusion number (bp)
I = Intercalator concentration- total (M)

$$K = \frac{[\text{occupied intercalation sites}]}{[\text{unoccupied intercalation sites}]\,[\text{free drug}]} \qquad \text{Equation B.1}$$

- Define concentrations with known variables

$$[\text{occupied intercalation sites}] = \left(\frac{L - Lo}{a}\right)D$$

$$[\text{unoccupied intercalation sites}] = \left(\frac{DB}{n}\right) - \left(\frac{L - Lo}{a}\right)D$$

$$[\text{free drug}] = I - \left(\frac{L - Lo}{a}\right)D$$

- Substitute back into Equation B.1

$$K = \frac{\left(\frac{L - Lo}{a}\right)D}{\left(\left(\frac{DB}{n}\right) - \left(\frac{L - Lo}{a}\right)D\right)\left(Io - \left(\frac{L - Lo}{a}\right)D\right)}$$

- Let $x = \left(\frac{L - Lo}{a}\right)$ for simplification

$$K = \frac{xD}{\left(\left(\frac{DB}{n}\right) - xD\right)(I - xD)}$$

- Divide D from numerator and denominator

$$K = \frac{x}{\left(\frac{B}{n} - x\right)(I - xD)}$$

- Multiply denominator

$$K = \frac{x}{\frac{BI}{n} - \frac{BD}{n}x - Ix + Dx^2}$$

- Multiply both sides of equation by denominator

$$x = \frac{KBI}{n} - \frac{KBD}{n}x - KIx + KDx^2$$

- Group x terms

$$x = KDx^2 - \left(\frac{KBD}{n} + KI\right)x + \frac{KBI}{n}$$

- Subtract x from both sides of equation

$$KDx^2 - \left(1 + \frac{KBD}{n} + KI\right)x + \frac{KBI}{n} = 0$$

- Substitute back in $x = \left(\frac{L - Lo}{a}\right)$

$$KD\left(\frac{L - Lo}{a}\right)^2 - \left(1 + \frac{KBD}{n} + KI\right)\left(\frac{L - Lo}{a}\right) + \frac{KBI}{n} = 0$$

- Multiply out parentheses

$$\frac{KD}{a^2}(L^2 - 2LLo + Lo^2) - \left(1 + \frac{KBD}{n} + KI\right)\left(\frac{L}{a}\right) + \left(1 + \frac{KBD}{n} + KI\right)\left(\frac{Lo}{a}\right) + \frac{KBI}{n} = 0$$

$$\frac{KD}{a^2}L^2 - \frac{2KD}{a^2}LLo + \frac{KD}{a^2}Lo^2 - \frac{L}{a} - \frac{KBD}{na}L - \frac{KI}{a}L + \frac{Lo}{a} + \frac{KBD}{na}Lo + \frac{KI}{a}Lo + \frac{KBI}{n} = 0$$

- Group L terms

$$\frac{KD}{a^2}L^2 - \left(\frac{2KDLo}{a^2} + \frac{1}{a} + \frac{KBD}{na} + \frac{KI}{a}\right)L + \left(\frac{KDLo^2}{a^2} + \frac{Lo}{a} + \frac{KDBLo}{na} + \frac{KILo}{a} + \frac{KBI}{n}\right) = 0$$

- Multiply by a

$$\frac{KD}{a}L^2 - \left(\frac{2KDLo}{a} + 1 + \frac{KBD}{n} + KI\right)L + \left(\frac{KDLo^2}{a} + Lo + \frac{KDBLo}{n} + KILo + \frac{KBIa}{n}\right) = 0$$

- Divide by KD

$$\frac{1}{a}L^2 - \left(\frac{2Lo}{a} + \frac{1}{KD} + \frac{B}{n} + \frac{I}{D}\right)L + \left(\frac{Lo^2}{a} + \frac{Lo}{KD} + \frac{BLo}{n} + \frac{ILo}{D} + \frac{BIa}{nD}\right) = 0$$

- Substitute $\mathbf{a}L^2 + \mathbf{b}L + \mathbf{c} = 0$ into quadratic equation $L = \dfrac{-b \pm \sqrt{b^2 - 4ac}}{2a}$

$$L = \frac{\left(\frac{2Lo}{a} + \frac{1}{KD} + \frac{B}{n} + \frac{I}{D}\right) \pm \sqrt{\left(\frac{2Lo}{a} + \frac{1}{KD} + \frac{B}{n} + \frac{I}{D}\right)^2 - 4\left(\frac{1}{a}\right)\left(\frac{Lo^2}{a} + \frac{Lo}{KD} + \frac{BLo}{n} + \frac{ILo}{D} + \frac{BIa}{nD}\right)}}{2\frac{1}{a}}$$

REFERENCES

1. Binning G, Rohrer H, Gerber C, Weibel E. Surface studies by scanning tunneling microscopy. Physical Review Letters 1982; 49: 57-61.
2. Binnig G, Gerber C, Stoll E, Albrecht TR, Quate CF. Atomic resolution with atomic force microscope. Surface Science 1987; 189-190: 1-6.
3. Hofer WA, Foster AS, Shluger AL. Theories of scanning probe microscopes at the atomic scale. Reviews of Modern Physics 2003; 75: 1287-1331.
4. Meyer E, Hug H-J, Bennewitz R. Scanning Probe Microscopy- The Lab on a Tip. Belin: Springer-Verlag; 2004.
5. Sarid D. Scanning Force Microscopy: With Applications to Electric, Magnetic and Atomic Forces, Revised Edition. [In: Oxford Ser. Opt. Imaging Sci., 1994; 5]. 1994.
6. Poggi MA, Gadsby ED, Bottomley LA, King WP, Oroudjev E, Hansma H. Scanning Probe Microscopy. Analytical Chemistry 2004; 76: 3429-3444.
7. Albrecht TR, Akamine S, Carver TE, Quate CF. Microfabrication of cantilever styli for the atomic force microscope. Journal of Vacuum Science & Technology, A: Vacuum, Surfaces, and Films 1990; 8: 3386-3396.
8. Morita S, Wiesendanger R, Meyer E, Editors. Noncontact Atomic Force Microscopy. 2002.
9. Li J, Cassell AM, Dai H. Carbon nanotubes as AFM tips: measuring DNA molecules at the liquid/solid interface. Surface and Interface Analysis 1999; 28: 8-11.

10. Noy A, Frisbie CD, Rozsnyai LF, Wrighton MS, Lieber CM. Chemical Force Microscopy: Exploiting Chemically-Modified Tips To Quantify Adhesion, Friction, and Functional Group Distributions in Molecular Assemblies. Journal of the American Chemical Society 1995; 117: 7943-7951.

11. Wiesendanger R. Scanning Probe Microscopy and Spectroscopy: Methods and Applications. New York: Cambridge University Press; 1994.

12. Manalis SR, Minne SC, Quate CF. Atomic force microscopy for high speed imaging using cantilevers with an integrated actuator and sensor. Applied Physics Letters 1996; 68: 871-873.

13. Schneir J, McWaid TH, Alexander J, Wilfley BP. Design of an atomic force microscope with interferometric position control. Journal of Vacuum Science & Technology, B: Microelectronics and Nanometer Structures 1994; 12: 3561-3566.

14. Tortonese M, Barrett RC, Quate CF. Atomic resolution with an atomic force microscope using piezoresistive detection. Applied Physics Letters 1993; 62: 834-836.

15. Parrat D, Sommer F, Solleti JM, Tran Minh D. Imaging modes in atomic force microscopy. Journal of Trace and Microprobe Techniques 1995; 13: 343-352.

16. Cappella B, Dietler G. Force-distance curves by atomic force microscopy. Surface Science Reports 1999; 34: 1-104.

17. Meyer E, Editor. Friction Force Microscopy. 1995.

18. Maivald P, Butt HJ, Gould SAC, Prater CB, Drake B, Gurley JA, Elings VB, Hansma PK. Using force modulation to image surface elasticities with the atomic force microscopy. Nanotechology 1991; 2: 103-112.

19. Hoelscher H. Analysis of microscopy and spectroscopy experiments. Noncontact Atomic Force Microscopy 2002: 349-369.

20. Zhong Q, Inniss D, Kjoller K, Elings VB. Fractured polymer/silica fiber surface studied by tapping mode atomic force microscopy. Surface Science 1993; 290: L688-L692.

21. Spatz JP, Sheiko S, Moeller M, Winkler RG, Reineker P, Marti O. Tapping Scanning Force Microscopy in Air - Theory and Experiment. Langmuir 1997; 13: 4699-4703.

22. Stark M, Stark RW, Heckl WM, Guckenberger R. Inverting dynamic force microscopy: from signals to time-resolved interaction forces. Proceedings of the National Academy of Sciences of the United States of America 2002; 99: 8473-8478.

23. Babcock KL, Prater CB. Phase Imaging: Beyond Topography. In: Digital Instruments Application Note; 1995.

24. Hansma HG. Surface biology of DNA by atomic force microscopy. Annual Review of Physical Chemistry 2001; 52: 71-92.

25. Hoerber JKH, Miles MJ. Scanning Probe Evolution in Biology. Science (Washington, DC, United States) 2003; 302: 1002-1005.

26. Alonso JL, Goldmann WH. Feeling the forces: atomic force microscopy in cell biology. Life Sciences 2003; 72: 2553-2560.

27. Jena B, Hoerber JKH, Editors. Atomic Force Microscopy in Cell Biology. [In: Methods Cell Biol., 2002; 68]. 2002.

28. Perfetti P, Cricenti A, Generosi R. Scanning probe microscopy applied to materials science and biology. Surface Review and Letters 2000; 7: 411-422.

29. Murray A, Leckenby J. Scanning probe microscopy applications in materials science. American Laboratory (Shelton, Connecticut) 1997; 29: 8, 10.

30. Bottomley LA, Coury JE, First PN. Scanning Probe Microscopy. Analytical Chemistry 1996; 68: 185-230.

31. Heymann B, Grubmuller H. Dynamic Force Spectroscopy of Molecular Adhesion Bonds. Physical Review Letters 2000; 84: 6126-6129.

32. Strunz T, Oroszlan K, Schafer R, Guntherodt H-J. Dynamic force spectroscopy of single DNA molecules. Proceedings of the National Academy of Sciences of the United States of America 1999; 96: 11277-11282.

33. Noy A, Vezenov DV, Lieber CM. Chemical force microscopy. Annual Review of Materials Science 1997; 27: 381-421.

34. Yu ET. Nanoscale characterization of semiconductor materials and devices using scanning probe techniques. Materials Science & Engineering, R: Reports 1996; R17: 147-206.

35. Balk LJ, Maywald M. Scanning force microscopy of semiconductor materials and devices. Materials Science & Engineering, B: Solid-State Materials for Advanced Technology 1994; B24: 203-208.

36. Higgins AM, Martin SJ, Jukes PC, Geoghegan M, Jones RAL, Langridge S, Cubitt R, Kirchmeyer S, Wehrum A, Grizzi I. Interfacial structure in semiconducting polymer devices. Journal of Materials Chemistry 2003; 13: 2814-2818.

37. Voet D, Voet JG. Biochemistry: Second Edition. 1995.

38. Pjura PE, Grzeskowiak K, Dickerson RE. Binding of Hoechst 33258 to the minor groove of B-DNA. Journal of Molecular Biology 1987; 197: 257.

39. Berman HM, Westbrook J, Feng Z, Gilliland G, Ghat TN, Weissig H, Shindyalov IN, Bourne PE. The Protein Data Bank. Nucleic Acids Research 2000; 28: 235-242.

40. Nielsen JE, Vriend G. Optimizing the hydrogen-bond network in Poisson-Boltzmann equation-based pK(a) calculations. Proteins 2001; 43: 403-412.

41. Metanomski WV. Compendium of Macromolecular Nomenclature. 1993.

42. Bustamante C, Marko JF, Siggia ED, Smith S. Entropic elasticity of lambda-phage DNA. Science 1994; 265: 1599-1600.

43. Access Excellence at the National Health Museum. Central dogma of molecular biology. www.accessexcellence.org; 1999.

44. Tessmer I, Baumann CG, Skinner GM, Molloy JE, Hoggett JG, Tendler SJB, Allen S. Mode of drug binding to DNA determined by optical tweezers force spectroscopy. Journal of Modern Optics 2003; 50: 1627-1636.

45. Leng F, Chaires JB, Waring MJ. Energetics of echinomycin binding to DNA. Nucleic Acids Research 2003; 31: 6191-6197.

46. Bordelon JA, Feierabend KJ, Siddiqui SA, Wright LL, Petty JT. Viscometry and atomic force microscopy studies of the interactions of a dimeric cyanine dye with DNA. Journal of Physical Chemistry B 2002; 106: 4838-4843.

47. Ban C, Ramakrishnan B, Sundaralingam M. Crystal structure of the highly distorted chimeric decamer r(C)d(CGGCGCCG)r(G).spermine complex--

spermine binding to phosphate only and minor groove tertiary base-pairing. Nucleic Acids Research 1994; 22: 5466.

48. Uytterhoeven K, Sponer J, Van Merrvelt L. Two 1:1 Binding Modes for Distamycin in the Minor Groove of D(Ggccaattgg). European Journal of Biochemistry 2002; 12: 2868.

49. Kopka ML, Yoon C, Goodsell D, Pjura P, Dickerson RE. Binding of an antitumor drug to DNA. Netropsin and C-G-C-G-A-A-T-T-BrC-G-C-G. Journal of Molecular Biology 1985; 183: 553-563.

50. Hud NV, Sklenar V, Feigon J. Localization of ammonium ions in the minor groove of DNA duplexes in solution and the origin of DNA A-tract bending. Journal of molecular biology 1999; 286: 651-660.

51. Wilson WD. DNA Intercalators. In; 1998: 427-476.

52. Brana MF, Cacho M, Gradillas A, de Pascual-Teresa B, Ramos A. Intercalators as anticancer drugs. Current pharmaceutical design 2001; 7: 1745-1780.

53. Thorpe JH, Hobbs JR, Todd AK, Denny WA, Charlton P, Cardin CJ. Guanine Specific Binding at a DNA Junction Formed by D[Cg(5-Bru)Acg]2 with a Topoisomerase Poison in the Presence of Co2+ Ions. Biochemistry 2000; 39: 15055.

54. Moore MH, Hunter WN, d'Estaintot BL, Kennard O. DNA-drug interactions. The crystal structure of d(CGATCG) complexed with daunomycin. Journal of Molecular Biology 1989; 206: 693.

55. Spielmann HP, Wemmer DE, Jacobsen JP. Solution structure of a DNA complex with a fluorescent bis-intercalator TOTO determined by NMR spectroscopy. Biochemistry 1995; 34: 8542.

56. Gaugain B, Barbet J, Oberlin R, Roques BP, Le Pecq JB. DNA bifunctional intercalators. 1. Synthesis and conformational properties of an ethidium homodimer and of an acridine ethidium heterodimer. Biochemistry 1978; 17: 5071-5078.

57. Shui X, Peek ME, Lipscomb LA, Gao Q, Ogata C, Roques BP, Garbay-Jaureguiberry C, Wilkinson AP, Williams LD. Effects of cationic charge on three-dimensional structures of intercalative complexes: structure of a bis-intercalated DNA complex solved by MAD phasing. Current Medicinal Chemistry 2000; 7: 59-71.

58. Peek ME, Lipscomb LA, Bertrand JA, Gao Q, Roques BP, Garbay-Jaureguiberry C, Williams LD. DNA Distortion in bis-Intercalated Complexes. Biochemistry 1994; 33: 3794-3800.

59. Coury JE, McFail-Isom L, Presnell S, Williams LD, Bottomley LA. Scanning probe visualization of electrostatically immobilized intercalating drug-nucleic acid complexes. Journal of Vacuum Science & Technology, A: Vacuum, Surfaces, and Films 1995; 13: 1746-1751.

60. Lokey RS, Kwok Y, Guelev V, Pursell CJ, Hurley LH, Iverson BL. A new class of polyintercalating molecules. Journal of the American Chemical Society 1997; 119: 7202-7210.

61. Murr MM, Harting MT, Guelev V, Ren J, Chaires JB, Iverson BL. An octakis-intercalating molecule. Bioorganic & Medicinal Chemistry 2001; 9: 1141-1148.

62. Guelev VM, Harting MT, Lokey RS, Iverson BL. Altered sequence specificity identified from a library of DNA-binding small molecules. Chemistry & Biology 2000; 7: 1-8.

63. Guelev VM, Cubberley MS, Murr MM, Lokey RS, Iverson BL. Design, synthesis, and characterization of polyintercalating ligands. Methods in Enzymology 2001; 340: 556-570.

64. Dixon DW. DNA threading intercalators: Rate constants for intercalation and electron transfer. Abstracts of Papers - American Chemical Society 2000; 220th: CHED-015.

65. Tanious FA, Yen SF, Wilson WD. Kinetic and equilibrium analysis of a threading intercalation mode: DNA sequence and ion effects. Biochemistry 1991; 30: 1813-1819.

66. Gallego J, Reid BR. Solution Structure and Dynamics of a Complex between DNA and the Antitumor Bisnaphthalimide LU-79553: Intercalated Ring Flipping on the Millisecond Time Scale. Biochemistry 1999; 38: 15104-15115.

67. Guelev V, Lee J, Ward J, Sorey S, Hoffman DW, Iverson BL. Peptide bis-intercalator binds DNA via threading mode with sequence specific contacts in the major groove. Chemistry & Biology 2001; 8: 415-425.

68. Guelev V, Sorey S, Hoffman DW, Iverson BL. Changing DNA Grooves - A 1,4,5,8-Naphthalene Tetracarboxylic Diimide Bis-Intercalator with the Linker (b-

Ala)3-Lys in the Minor Groove. Journal of the American Chemical Society 2002; 124: 2864-2865.

69. Bloomfield VA. DNA condensation by multivalent cations. Biopolymers 1998; 44: 269-282.

70. Wilson RW, Bloomfield VA. Counterion-induced condensation of deoxyribonucleic acid. A light-scattering study. Biochemistry 1979; 18: 2192-2196.

71. Conwell CC, Hud NV. Evidence That Both Kinetic and Thermodynamic Factors Govern DNA Toroid Dimensions: Effects of Magnesium(II) on DNA Condensation by Hexammine Cobalt(III). Biochemistry 2004; 43: 5380-5387.

72. Bright JN, Stevens MJ, Hoh J, Woolf TB. Characterizing the function of unstructured proteins: Simulations of charged polymers under confinement. Journal of Chemical Physics 2001; 115: 4909-4918.

73. Grosberg AY, Khokhlov AR. Statistical Physics of Macromolecules. 1994.

74. Fink TR, Crothers DM. Comparison of several calculations of helix-coil transitions in heterogeneous polymers. Biopolymers 1968; 6: 863-871.

75. Morita M, Tasaka M, Fujisawa H. DNA packaging ATPase of bacteriophage T3. Virology 1993; 193: 748-752.

76. Vijayanathan V, Thomas T, Thomas TJ. DNA Nanoparticles and Development of DNA Delivery Vehicles for Gene Therapy. Biochemistry 2002; 41: 14085-14094.

77. Mou J, Czajkowsky DM, Zhang Y, Shao Z. High-resolution atomic-force microscopy of DNA: the pitch of the double helix. FEBS Letters 1995; 371: 279-282.

78. Hansma HG, Laney DE, Bezanilla M, Sinsheimer RL, Hansma PK. Applications for atomic force microscopy of DNA. Biophysical Journal 1995; 68: 1672-1677.

79. Allen MJ, Hud NV, Balooch M, Tench RJ, Siekhaus WJ, Balhorn R. Tip-radius-induced artifacts in AFM images of protamine-complexed DNA fibers. Ultramicroscopy 1992; 42-44: 1095-1100.

80. Thundat T, Warmack RJ, Allison DP, Bottomley LA, Lourenco AJ, Ferrell TL. Atomic force microscopy of deoxyribonucleic acid strands adsorbed on mica: the effect of humidity on apparent width and image contrast. Journal of Vacuum Science & Technology, A: Vacuum, Surfaces, and Films 1992; 10: 630-635.

81. Coury JE, Anderson JR, McFail-Isom L, Williams LD, Bottomley LA. Scanning Force Microscopy of Small Ligand-Nucleic Acid Complexes: Tris(o-phenanthroline)ruthenium(II) as a Test for a New Assay. Journal of the American Chemical Society 1997; 119: 3792-3796.

82. Berge T, Jenkins NS, Hopkirk RB, Waring MJ, Edwardson JM, Henderson RM. Structural perturbations in DNA caused by bis-intercalation of ditercalinium visualized by atomic force microscopy. Nucleic Acids Research 2002; 30: 2980-2986.

83. Berge T, Lucy Haken E, Waring MJ, Henderson RM. The binding mode of the DNA bisintercalator luzopeptin investigated using atomic force microscopy. Journal of Structural Biology 2003; 142: 241-246.

84. Fang Y, Hoh JH. Early Intermediates in Spermidine-Induced DNA Condensation on the Surface of Mica. Journal of the American Chemical Society 1998; 120: 8903-8909.

85. Golan R, Pietrasanta LI, Hsieh W, Hansma HG. DNA Toroids: Stages in Condensation. Biochemistry 1999; 38: 14069-14076.

86. Dunlap DD, Maggi A, Soria MR, Monaco L. Nanoscopic structure of DNA condensed for gene delivery. Nucleic Acids Research 1997; 25: 3095-3101.

87. Moreno-Herrero F, Colchero J, Gomez-Herrero J, Baro AM. Atomic force microscopy contact, tapping, and jumping modes for imaging biological samples in liquids. Physical Review E: Statistical, Nonlinear, and Soft Matter Physics 2004; 69: 031915/031911-031915/031919.

88. Amemiya, Takahashi, Nakazawa, Yasuda N, Yamamoto M, Nakagawa Y, Kageji T, Nakaichi M, Ogura K. High-speed Scanning of Atomic Force Microscope. In: National Institute of Radiological Sciences; 1999.

89. Rogers B, Sulchek T, Murray K, York D, Jones M, Manning L, Malekos S, Beneschott B, Adams JD, Cavazos H, Minne SC. High speed tapping mode atomic force microscopy in liquid using an insulated piezoelectric cantilever. Review of Scientific Instruments 2003; 74: 4683-4686.

90. Rivetti C, Codeluppi S. Accurate length determination of DNA molecules visualized by atomic force microscopy: evidence for a partial B- to A-form transition on mica. Ultramicroscopy 2001; 87: 55-66.

91. Hansma HG, Laney DE. DNA binding to mica correlates with cationic radius: assay by atomic force microscopy. Biophysical Journal 1996; 70: 1933-1939.

92. Rivetti C, Guthold M, Bustamante C. Scanning force microscopy of DNA deposited onto mica: equilibration versus kinetic trapping studied by statistical polymer chain analysis. Journal of Molecular Biology 1996; 264: 919-932.

93. Lyubchenko YL, Gall AA, Shlyakhtenko LS, Harrington RE, Jacobs BL, Oden PI, Lindsay SM. Atomic force microscopy imaging of double stranded DNA and RNA. Journal of Biomolecular Structure & Dynamics 1992; 10: 589-606.

94. O'Brien JC, Stickney JT, Porter MD. Self-Assembled Double-Stranded DNA (dsDNA) Microarrays for Protein:dsDNA Screening Using Atomic Force Microscopy. Journal of the American Chemical Society 2000; 122: 5004-5005.

95. Coury JE. Scanning probe studies of small ligand-nucleic acid complexes (intercalation, SFM). 1997.

96. Yokota H, Sunwoo J, Sarikaya M, Van den Engh G, Aebersold R. Spin-Stretching of DNA and Protein Molecules for Detection by Fluorescence and Atomic Force Microscopy. Analytical Chemistry 1999; 71: 4418-4422.

97. McGhee JD, Von Hippel PH. Theoretical aspects of DNA-protein interactions. Cooperative and noncooperative binding of large ligands to a one-dimensional homogeneous lattice. Journal of Molecular Biology 1974; 86: 469-489.

98. Lillehei PT, Bottomley LA. Scanning force microscopy of nucleic acid complexes. Methods in Enzymology 2001; 340: 234-251.

99. Crothers DM. Calculation of melting curves for DNA. Biopolymers 1968; 6: 1391-1404.

100. Bubienko E, Cruz P, Thomason JF, Borer PN. Nearest-neighbor effects in the structure and function of nucleic acids. Progress in Nucleic Acid Research and Molecular Biology 1983; 30: 41-90.

101. Lerman LS. Structural considerations in the interaction of deoxyribonucleic acid and acridines. Journal of Molecular Biology 1961; 3: 18-30.

102. Windom J, Baldwin RL. Cation-induced toroidal condensation of DNA studies with Co3+(NH3)6. Journal of Molecular Biology 1980; 144: 431-453.

103. Bloomfield VA. DNA condensation. Current Opinion in Structural Biology 1996; 6: 334-341.

104. Adrian M, ten Heggeler-Bordier B, Wahli W, Stasiak AZ, Stasiak A, Dubochet J. Direct visualization of supercoiled DNA molecules in solution. EMBO journal 1990; 9: 4551-4554.

105. Sines CC, McFail-Isom L, Howerton SB, VanDerveer D, Williams LD. Cations Mediate B-DNA Conformational Heterogeneity. Journal of the American Chemical Society 2000; 122: 11048-11056.

106. Hud NV, Polak M. DNA-cation interactions: the major and minor grooves are flexible ionophores. Current Opinion in Structural Biology 2001; 11: 293-301.

107. Duguid JG, Bloomfield VA, Benevides JM, Thomas GJ, Jr. Raman spectroscopy of DNA-metal complexes. II. The thermal denaturation of DNA in the presence of Sr2+, Ba2+, Mg2+, Ca2+, Mn2+, Co2+, Ni2+, and Cd2+. Biophysical Journal 1995; 69: 2623-2641.

108. Conwell CC, Vilfan ID, Hud NV. Controlling the size of nanoscale toroidal DNA condensates with static curvature and ionic strength. Proceedings of the National Academy of Sciences of the United States of America 2003; 100: 9296-9301.

109. Teixeira SCM, Thorpe JH, Todd AK, Powell HR, Adams A, Wakelin LPG, Denny WA, Cardin CJ. Structural Characterization of Bisintercalation in Higher-order DNA at a Junction-like Quadruplex. Journal of Molecular Biology 2002; 323: 167-171.

110. Shen MR, Downing KH, Balhorn R, Hud NV. Nucleation of DNA Condensation by Static Loops: Formation of DNA Toroids with Reduced Dimensions. Journal of the American Chemical Society 2000; 122: 4833-4834.

111. Evdokimov YM, Platonov AL, Tikhonenko AS, Varshavskii YM. Compact form of double-stranded DNA in solution. FEBS Letters 1972; 23: 180-184.

112. Stevens MJ. Simple simulations of DNA condensation. Biophysical Journal 2001; 80: 130-139.

113. Manning GS. Quarterly Review in Biophysics 1978; 11: 179-246.

114. Sitko JC, Mateescu EM, Hansma HG. Sequence-dependent DNA condensation and the electrostatic zipper. Biophysical Journal 2003; 84: 419-431.

115. Manning GS. Thermodynamic stability theory for DNA doughnut shapes induced by charge neutralization. Biopolymers 1980; 19: 37-59.

116. Ariel G, Andelman D. Polyelectrolyte persistence length: Attractive effect of counterion correlations and fluctuations. Europhysics Letters 2003; 61: 67-73.

117. Marquet R, Houssier C. Thermodynamics of cation-induced DNA condensation. Journal of Biomolecular Structure & Dynamics 1991; 9: 159-167.

118. Zakharova SS, Egelhaaf SU, Bhuiyan LB, Outhwaite CW, Bratko D, van der Maarel JRC. Multivalent ion-DNA interaction: Neutron scattering estimates of polyamine distribution. Journal of Chemical Physics 1999; 111: 10706-10716.

119. Hansma HG, Golan R, Hsieh W, Lollo CP, Mullen-Ley P, Kwoh D. DNA condensation for gene therapy as monitored by atomic force microscopy. Nucleic Acids Research 1998; 26: 2481-2487.

120. Vijayanathan V, Thomas T, Antony T, Shirahata A, Thomas TJ. Formation of DNA nanoparticles in the presence of novel polyamine analogues: a laser light scattering and atomic force microscopic study. Nucleic Acids Research 2004; 32: 127-134.

121. Bloomfield VA. Condensation of DNA by multivalent cations: considerations on mechanism. Biopolymers 1991; 31: 1471-1481.

122. Martin AL, Davies MC, Rackstraw BJ, Roberts CJ, Stolnik S, Tendler SJB, Williams PM. Observation of DNA-polymer condensate formation in real time at a molecular level. FEBS Letters 2000; 480: 106-112.

123. Vijayanathan V, Thomas T, Shirahata A, Thomas TJ. DNA Condensation by Polyamines: A Laser Light Scattering Study of Structural Effects. Biochemistry 2001; 40: 13644-13651.

124. Allen MJ, Bradbury EM, Balhorn R. AFM analysis of DNA-protamine complexes bound to mica. Nucleic Acids Research 1997; 25: 2221-2226.

125. Lin Z, Wang C, Feng X, Liu M, Li J, Bai C. The observation of the local ordering characteristics of spermidine-condensed DNA: atomic force microscopy and polarizing microscopy studies. Nucleic Acids Research 1998; 26: 3228-3234.

126. Hud NV, Downing KH. Cryoelectron microscopy of l phage DNA condensates in vitreous ice: the fine structure of DNA toroids. Proceedings of the National Academy of Sciences of the United States of America 2001; 98: 14925-14930.

127. Yoshikawa Y, Yoshikawa K, Kanbe T. Formation of a Giant Toroid from Long Duplex DNA. Langmuir 1999; 15: 4085-4088.

128. Arscott PG, Li A, Bloomfield VA. Condensation of DNA by trivalent cations. 1. Effects of DNA length and topology on the size and shape of condensed particles. Biopolymers 1990; 30: 619-630.

129. Fang Y, Hoh JH. Cationic silanes stabilize intermediates in DNA condensation. FEBS letters 1999; 459: 173-176.

130. Moreno-Herrero F, Colchero J, Baro AM. DNA height in scanning force microscopy. Ultramicroscopy 2003; 96: 167-174.

131. Kindt J, Tzlil S, Ben-Shaul A, Gelbart WM. DNA packaging and ejection forces in bacteriophage. Proceedings of the National Academy of Sciences of the United States of America 2001; 98: 13671-13674.

132. Arscott PG, Ma C, Wenner JR, Bloomfield VA. DNA condensation by cobalt hexaammine (III) in alcohol-water mixtures: dielectric constant and other solvent effects. Biopolymers 1995; 36: 345-364.

133. Plum GE, Arscott PG, Bloomfield VA. Condensation of DNA by trivalent cations. 2. Effects of cation structure. Biopolymers 1990; 30: 631-643.

134. Vasilevskaya VV, Khokhlov AR, Kidoaki S, Yoshikawa K. Structure of collapsed persistent macromolecule: toroid vs. spherical globule. Biopolymers 1997; 41: 51-60.

135. Lang D, Taylor TN, Dobyan DC, Gray DM. Dehydrated circular DNA: electron microscopy of ethanol-condensed molecules. Journal of Molecular Biology 1976; 106: 97-107.

136. Marx KA. Structure and Dynamics of Biopolymers. In: Nicolini CA (ed.) NATO ASI Series; Series E, Applied Sciences, vol. 133. Dordrecht and Boston: Nijhoff; 1987: 137-168.

137. Report of Economic Survey 2001. In: Merrill SA, Levin R, C., Myers MB (eds.): American Intellectual Property Law Association; 2002.

138. Market Report. In; 2002.

139. Sen D, Crothers DM. Condensation of chromatin: role of multivalent cations. Biochemistry 1986; 25: 1495-1503.

140. Benson SC, Singh P, Glazer AN. Heterodimeric DNA-binding dyes designed for energy transfer: synthesis and spectroscopic properties. Nucleic Acids Research 1993; 21: 5727-5735.

VITA

Elizabeth Deibler Gadsby earned a Bachelor of Science with a major in Microbiology and a minor in Chemistry from the University of Florida. Her interest in business led her to elect numerous courses in the College of Business as well.

In part, this interest led Ms. Gadsby to begin her career in applied science at the Kimberly-Clark Corporation, in Roswell, Georgia, north of Atlanta. She has served as a research scientist and project leader for twelve years. Through her research efforts, she and her colleagues have been awarded more than twenty United States patents in fields including nonwoven treatments, sensors and water purification.

Ms. Gadsby's ties to the Georgia Institute of Technology include her grandmother, Dr. Helen H. Naugle, who became the first female professor at Georgia Tech in 1962. Her father, Dr. Lynn L. Deibler, received his Master's in Physics at Georgia Tech. During her Ph.D. career at Georgia Tech, Ms. Gadsby participated in the TI:GER innovation program's inaugural class, in which her team won the Otis Award. She was also an NSF and Georgia Tech Presidential Fellow during her student tenure.

Ms. Gadsby has been married to her husband James for ten years. They have enjoyed volunteering for a number of Atlanta organizations, including the Atlanta Symphony Orchestra, the Fox Theater, and the 1996 Centennial Olympic Games. Additionally, they are active members at River Community Church, where Ms. Gadsby has served on the Servant Leader Council Board. She and her husband also currently serve on the Board of North Georgia Walk to Emmaus, an international Christian retreat movement. In addition to their Georgia Tech allegiance, they remain avid Florida Gator football fans.